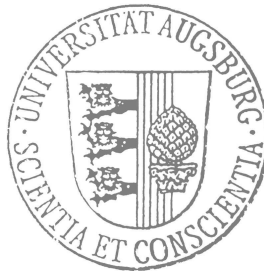# Phase Transitions in Low-Dimensional Transition Metal Compounds

Dissertation zur Erlangung des Doktorgrades
der Mathematisch-Naturwissenschaftlichen
Fakultät der Universität Augsburg

vorgelegt von
MARKUS HOINKIS

August 2006

Contents

Contents

List of Figures

List of Tables

1 Introduction

Transition metal compounds exhibit some of the most intriguing phenomena in condensed matter physics. Famous examples are the occurrence of high-temperature superconductivity in materials with copper-oxygen planes, the colossal magnetoresistance in manganese-based perovskite oxides, or the Mott metal-insulator transition, e.g., in certain vanadates. The richness of physics in these compounds is promoted by several factors. First of all, electronic correlations play an important role due to the spatial confinement in narrow d orbitals, so that the above mentioned effects cannot be described within the one-particle picture. They have to be understood as cooperative phenomena involving a large number of microscopic degrees of freedom. The complex interplay of the d electrons' internal degrees of freedom — i.e., charge, spin and orbital angular momentum — together with the lattice degrees of freedom, often makes this class of materials extremely sensitive to small changes in external parameters, such as temperature, pressure, magnetic field, or doping. Moreover certain structural aspects influence the emergence of exotic ordering phenomena at low temperatures. Geometric frustration of the magnetic interactions and a reduced dimensionality have to be named in this context.

In this thesis two studies of low-dimensional transition metal compounds are presented, in which virtually all of the above listed ingredients contribute and the competition of the involved degrees of freedom leads to interesting broken-symmetry ground states. The physics of the quasi-two-dimensional material $1T$-TaSe$_2$, on which the focus lies first, is characterized by the occurrence of two, usually separate phenomena: The charge density wave (CDW) and the Mott metal-insulator transition. This is already a clear sign that the charge, spin and lattice degrees of freedom are tightly entangled in this system. Unfortunately, a theoretical description of the Mott transition is not yet able to fully incorporate all these aspects. Up to date the Hubbard model, which is typically chosen to describe strongly correlated systems, can only be solved under rather restrictive assumptions, and a realistic modelling including the coupling to the lattice is not yet possible. Nevertheless, it will be shown that this system offers the opportunity to study a metal-insulator transition that can be described in close analogy to the highly idealized Hubbard model. It is possible to measure the energy- and momentum dependent electronic excitation spectrum while tuning the crucial ratio U/W of the onsite Coulomb energy U and the electronic bandwidth W in the same crystal, controlled by an external parameter, namely by varying the temperature. Remarkably, this is possible by exploiting the properties of the charge density wave, which modulates the transfer integrals and therewith modifies the bandwidth as a function of temperature.

Motivated by the discovery of this effect in 2003 [Perfetti03], a detailed investigation of the electronic properties of $1T$-TaSe$_2$ was conducted by means of photoelectron spectroscopy (PES), supplemented by density functional theory (DFT) calculations in collaboration with Dr. Eyert (Universität Augsburg).

In the second and more extensive study focussing on the titanium oxyhalides TiOCl and TiOBr, it will be shown that the physics of these low-dimensional compounds is again characterized by the interplay between electronic and lattice degrees of freedom. In conjuncture with the low spin of $S = 1/2$ and the geometric frustration of a simple antiferromagnetic order, these quantum magnets can be considered promising candidates for the long-sought realization of the resonating valence bond (RVB) state. However, it will become clear that these compounds — at least when undoped — adopt a different, but not less interesting ground state, viz., a spin-Peierls state with record-high energy scales concerning the magnetic exchange and the transition temperatures.

This was first shown by Seidel *et al.* in 2003 [Seidel03], and motivated by this discovery TiOCl single crystals were synthesized by means of the chemical vapor transport (CVT) technique in cooperation with Dr. Klemm at Prof. Horn's chair (Universität Augsburg). It is not exaggerated to state that the sample preparation delivered excellent results, as a comparison with other published results of, e.g., the magnetic susceptibility proves. Based on this success, several experimental collaborations were initiated with the aim to find a consistent and comprehensive picture of the physics in TiOCl. The nature of the two successive phase transitions was investigated by measurements of the specific heat by Dr. Hemberger at Prof. Loidl's chair (Universität Augsburg) [Hemberger05]. Further collaborations with Prof. Loidl's group include an electron spin resonance (ESR) study [Zakharov06], and an x-ray diffraction (XRD) experiment at Hasylab in Hamburg [Krimmel06] carried out by Dr. Krimmel, who is also in charge of neutron scattering experiments at the Institute Laue-Langevin in Grenoble, France. Another fruitful collaboration exists with Prof. van Smaalen's group (Universität Bayreuth), which lead to the determination of the low-temperature structure of TiOCl and its unambiguous identification as a spin-Peierls state [Shaz05]. Even though the following efforts did not result in publications (yet), it is added that muon spin rotation (μSR) experiments were conducted in a collaboration with Prof. Blundells group in Oxford, United Kingdom, and an extended x-ray absorption fine structure (EXAFS) experiment was carried out by Dr. Pfalzer of Prof. Horn's chair at the ANKA synchrotron in Karlsruhe.

A main focus of this thesis must certainly be seen in the investigation of the electronic structure of the oxyhalides TiOCl and TiOBr, both by experimental and theoretical means [Hoinkis05, Hoinkis06]. An extensive photoemission study includes homelab measurements at He I, He II and Al K$_\alpha$ photon energies, angle-resolved mappings of the electronic dispersions of both TiOCl and TiOBr (TiOBr crystals were supplied by Prof. van Smaalen's group), and polarization-dependent experiments with the aim to determine the symmetry of the TiOCl valence states. Furthermore, photoemission and x-ray absorption synchrotron experiments were performed at the Swiss Light Source in Villigen, Switzerland, at Elettra in Trieste, Italy, and at BESSY II in Berlin, which turned out

to be complicated by charging effects due to the insulating nature of TiOCl. On the theoretical side, the photoemission data were complemented within a framework of collaborations with several theory groups. The cooperation with Prof. Valenti (Universität Frankfurt) and her co-workers is pointed out as particularly productive, as it enabled a comparison of the experimental TiOCl and TiOBr spectra to various DFT calculations [Hoinkis05, Hoinkis06]. Moreover, a collaboration with Prof. Jeckelmann (Universität Hannover) and Dr. Benthien (Universität Marburg), who calculated the spectral function of the one-dimensional Hubbard model, must not be forgotten, as their results turned out to yield the best available match to the photoemission data [Hoinkis05].

Last but not least another experimental collaboration is cited to close the circle and return to the initially mentioned prospects regarding RVB physics in TiOCl: Very interesting results arose from the cooperation with Prof. Kuntscher's group (formerly Universität Stuttgart, now Universität Augsburg), which discovered a metal-insulator transition under pressure by means of optical spectroscopy [Kuntscher06]. The possibility to drive the compound TiOCl into a metallic state certainly fuels the speculations of the proximity to an RVB state, which is particularly interesting considering the prospects of a novel, RVB-type superconductivity.

Outline of the Thesis

This dissertation is structured as follows: In Chapter 2 the theoretical concepts necessary to describe the various phenomena occurring in the examined compounds are discussed. It was already mentioned that this includes the Mott metal-insulator transition, the charge density wave instability, the spin-Peierls transition, and the RVB model. It will be seen that these topics, although they might seem rather unrelated at first glance, share many common features and exhibit a multitude of parallels. This becomes obvious, for example, in the often very similar description of the systems with Hamilton operators that appear in almost identical form in various sections of this chapter. And also certain aspects of the mean-field descriptions, which often refer to the well known BCS results of ordinary superconductivity, show a strong resemblance in this chapter. After a brief introduction into the experimental technique of photoemission, which is given in Chapter 3 due to its importance for this thesis, the two central chapters follow. Chapter 4 focusses — as outlined above — on the experimental and theoretical investigation of the transition metal compound $1T$-TaSe$_2$. In Chapter 5, a comprehensive study of the titanium oxyhalides TiOCl and TiOBr by means of various experimental and theoretical methods is presented. The thesis concludes with a short summary in Chapter 6.

2 Theoretical Concepts

2.1 Mott Transition

It was a great success of quantum mechanics in the 1920s and 1930s that the metallic or insulating behavior of numerous materials could be explained applying the independent electron approximation. Band theory discovered that the distinctive feature between metals and non-metals is the presence or absence of a partly filled band. However, it was soon realized that systems with open d and f shells, where the corresponding orbitals are quite localized and hence the electrons occupy narrow orbitals, pose a problem to this scheme. In many transition metal compounds, especially in those involving cations of the $3d$ series, the independent electron approximation breaks down: The highly correlated electrons experience a strong, short-ranged Coulombic repulsion so that they cannot be treated independently. At a conference in Bristol in 1937 it was pointed out by de Boer and Verwey that Nickel oxide is an insulator despite the fact that its eight d electrons should only partly fill the $3d$ subshells [Mott90]. In the following discussion Peierls already attributed this phenomenon to electronic correlations, but it took more than ten years until Mott published his famous work that explains the insulating nature of NiO and describes the possibility of a metal-insulator transition, now termed the Mott transition [Mott49, Mott61]. It was mainly for this work that he was granted the 1977 Nobel prize in physics, together with van Vleck and Anderson. It is interesting to note that, beyond this achievement, the latter name is inseparably connected with the resonating valence bond theory presented in Chapter 2.4.

In a *Gedankenexperiment* Mott imagined a crystalline array of hydrogen-like atoms with a lattice constant a that can be varied, as illustrated in Fig. 2.1 (a) [Mott61]. In a tight-binding picture, the single s electron per site gives rise to a half-filled band, whose width depends on the orbitals' overlap. Starting with a value of a comparable to the extent of the $1s$ orbital, a rather wide band will be formed. According to band theory this crystal is expected to be metallic. This statement should continue to hold when the interatomic distances are increased. Of course, the s band will become narrower as sketched in Fig. 2.1 (b), nevertheless it will be always half-filled so that the hypothetic crystal remains in a metallic state. It goes without saying that this scenario eventually becomes absurd, when the lattice constant is large enough that clearly an array of neutral atoms is expected. This result can not be explained within the independent electron picture. How can it be then understood that the hypothetical stretching of this crystal will finally end in an insulating state? The crucial argument is that at
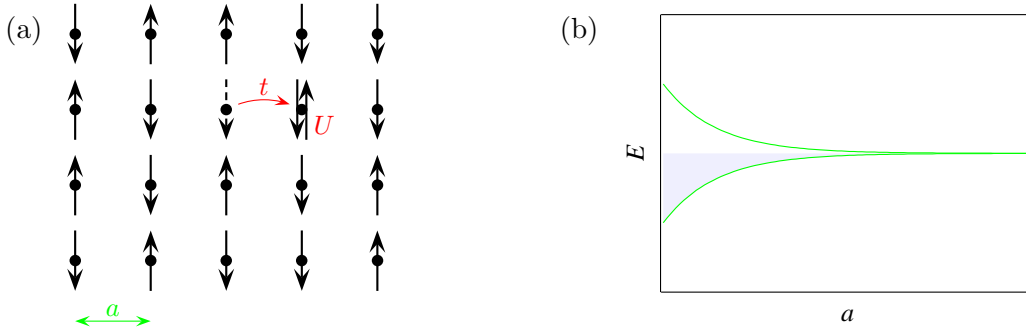
Figure 2.1: *Gedankenexperiment of a hypothetical crystal with variable lattice constant. (a) Square lattice with a lattice constant a and one electron per site. Hopping of an electron creates a doubly-occupied site and is therefore connected with the energy cost U. (b) Schematic representation of the lattice constant dependence of the tight-binding band structure. The s band becomes narrower with increasing lattice constant a, but stays half-filled (The shading indicates filled states).*

half-filling transport of charge is inevitably connected with double occupancy of sites. If two electrons share the same orbital, they have to pay an energy cost, the intra-atomic Coulomb energy, usually referred to as Hubbard U. This quantity is typically in the range from $1\,\mathrm{eV}$ to $10\,\mathrm{eV}$ for the valence orbitals of a solid material. The critical question is now, does the kinetic energy gain t connected with the hopping outweigh the energy cost U? Above some critical value of the lattice constant it will certainly not, so that an insulating state results. It is remarkable that there is no smooth cross-over from the metallic to the non-metallic state as one could naively expect — on the contrary, a first order phase transition was predicted by Mott using a screening argument [Mott61]. He pointed out that in the insulating state, electron-hole pairs can be formed as a consequence of their Coulomb attraction. For the metallic phase he assumed that the formation of excitons is inhibited by the Thomas-Fermi screening, where the bare Coulomb potential $-e^2/r$ is replaced by

$$- (e^2/r) \exp(-qr), \tag{2.1}$$

with the constant q depending on the density of free electrons n. He assumed that the transition into an insulating state would occur when the screening is just weak enough that an electron could be trapped. The resulting transition would therefore be discontinuous. From this condition Mott estimated the threshold

$$n^{1/3} a_{\mathrm{H}} \approx 0.2 \tag{2.2}$$

for the metal-insulator transition, where a_{H} is the Bohr radius.

While the Mott insulator can be easiest understood in the above real-space picture, the conduction electrons of metals are best described as Bloch waves in momentum space. The modelling of the Mott transition is complicated as one moves away from these extreme limits and tries to address the electrons of transition metal compounds that are neither fully itinerant nor fully localized at their atomic sites [Kotliar04].

Hubbard Model

The simplest model able to describe these two extreme cases is the Hubbard model. It became a standard framework for studying the Mott transition since it was introduced independently by Gutzwiller, Hubbard and Kanamori [Gutzwiller63, Hubbard63, Kanamori63]. The single-band Hubbard Hamiltonian reads

$$\mathcal{H}_{\text{Hubbard}} = \mathcal{T} + \mathcal{U} = t \sum_{\langle ij \rangle \sigma} \left(c_{i\sigma}^{\dagger} c_{j\sigma} + c_{j\sigma}^{\dagger} c_{i\sigma} \right) + U \sum_{i} n_{i\uparrow} n_{i\downarrow}, \tag{2.3}$$

where i and j are lattice site indices, $\sigma = \uparrow, \downarrow$ denotes the spin, angle brackets $\langle ij \rangle$ indicate a summation over nearest neighbors, and every pair shall be counted only once. The operator $c_{i\sigma}^{\dagger}$ creates an electron with spin σ in a Wannier state $\phi(\mathbf{r} - \mathbf{R}_i)$ at the lattice site i, whereas $c_{i\sigma}$ is the corresponding destruction operator. The number operator is defined as $n_{i\sigma} = c_{i\sigma}^{\dagger} c_{i\sigma}$.

The Hubbard Hamiltonian is characterized by the competition of its two parts, the kinetic energy or band term $\mathcal{T}$ and the interaction term $\mathcal{U}$. The relative strength of the two terms is parameterized by the transfer integral t and by the local Coulomb repulsion U, respectively. While the kinetic part promotes the mobility of electrons, the interaction energy is minimized by suppressing charge fluctuations involving a double occupancy of sites — a localization at the atomic sites is thus favored. The two parts will be separately examined in the following.

The kinetic energy term $\mathcal{T}$ describes the energy gain associated with hopping from site to site. Note that this term, strictly speaking, has contributions from both the kinetic energy, and the atomic potentials [Fazekas99a]. This band term can be Fourier transformed into its diagonal representation

$$\mathcal{T} = \sum_{\mathbf{k}\sigma} \epsilon_{\mathbf{k}} n_{\mathbf{k}\sigma}. \tag{2.4}$$

The dilemma of choosing between real space and momentum space to describe the Mott transition is now also formally evident: While the kinetic part $\mathcal{T}$ is diagonal when expressed in terms of Bloch waves, the interaction part $\mathcal{U}$ is diagonal in real space using the Wannier state description. The energy $\epsilon(\mathbf{k})$ of the Bloch wave is obtained by the Fourier transformation. For a D-dimensional cubic lattice with lattice constant a the result is simply

$$\epsilon(\mathbf{k}) = -2t \sum_{j=i}^{D} \cos k_j a. \tag{2.5}$$

The bandwidth W is thus proportional to the hopping probability:

$$W = 4Dt \tag{2.6}$$

Instead of this tight-binding approach, it is also possible to admit any form of $\epsilon(\mathbf{k})$ in the Hubbard model, so that the result of band structure calculations can be adopted.
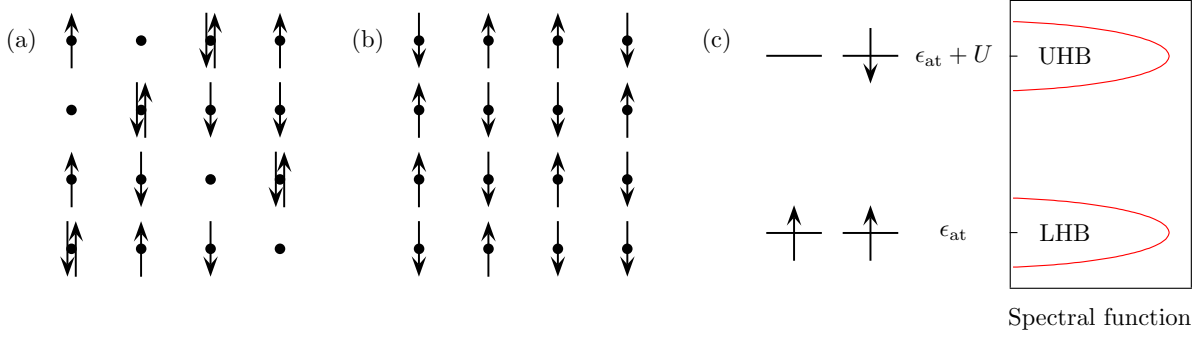
Figure 2.2: *(a) Snapshot of the Fermi sea ground state of $\mathcal{T}$. On average 25% of the sites are doubly occupied, and 25% are empty. (b) One possible configuration of the insulating ground state of $\mathcal{U}$. Every site is occupied with exactly one electron. For N sites, 2^N degenerate spin configurations exist. (c) Energy level diagram for two sites with single and double occupancy, respectively. The incoherent propagation of these states leads to the broadened lower Hubbard band (LHB) and upper Hubbard band (UHB) shown on the right hand side.*

At half-filling, the metallic ground state $|\Psi_{\mathrm{m}}\rangle$ of $\mathcal{T}$ is easily determined: It is given by the Fermi sea

$$|\Psi_{\mathrm{m}}\rangle = \prod_{\mathbf{k}}^{\epsilon_{\mathbf{k}}<\epsilon_{\mathrm{F}}} c_{\mathbf{k}\uparrow}^{\dagger} c_{\mathbf{k}\downarrow}^{\dagger} |0\rangle, \qquad (2.7)$$

filled up to the Fermi energy ϵ_{F}. In this state the occupancy of an orbital by an electron with spin "up" is independent of its occupation with spin "down". In other words, the probability of finding an electron with a certain spin direction at a given site is 50%. Consequently the probability for double occupancy is 25%, just as 25% of the sites will be empty. Figure 2.2 (a) shows a snapshot characteristic of the Fermi sea in real space.

Now the second part of the Hubbard Hamiltonian, $\mathcal{U}$, will be addressed. It takes account of the interaction of electrons sharing the same Wannier orbital due to the Coulomb repulsion. The Hubbard U is defined as

$$U = \int \mathrm{d}\mathbf{r}_1 \, \mathrm{d}\mathbf{r}_2 \, |\phi(\mathbf{r}_1 - \mathbf{R}_i)|^2 \, \frac{e^2}{|\mathbf{r}_1 - \mathbf{r}_2|} \, |\phi(\mathbf{r}_2 - \mathbf{R}_i)|^2. \qquad (2.8)$$

In this simple model only the onsite Coulomb interaction is regarded, while the long-range part of the Coulomb interaction is neglected (which indeed at least partially cancels out due to screening effects). The insulating ground state $|\Psi_{\mathrm{i}}\rangle$ of the interaction term $\mathcal{U}$ at half-filling is trivially given by the constellation with every site singly occupied. It is highly degenerate since every spin is free to point up or down,[1] as shown in Fig. 2.2 (b).

An interesting observation can be made when the two states $|\Psi_{\mathrm{m}}\rangle$ and $|\Psi_{\mathrm{i}}\rangle$ are used as trial wave functions for the Hubbard Hamiltonian [Müller-Hartmann88]. For a cubic two-dimensional lattice the energies of these states are obtained to be $\epsilon_{\mathrm{m}} = -16t/\pi^2 + U/4$

---

[1]In Chapter 2.3 it will be seen that a Mott insulator tends to magnetic ordering in the sense that the spins effectively interact. However, for this phenomenon it is essential that hopping of electrons is allowed for, whereas here only the term $\mathcal{U}$ is considered.

and $\epsilon_i = 0$. From this simple estimate it can be already concluded that a critical ratio U/t exists, where the system undergoes a transition from metallic to insulating behavior. For the one-dimensional Hubbard model it must be stated though, that a metal-insulator transition does *not* occur, proven by Lieb and Wu with a Bethe Ansatz [Lieb68]. Later in this chapter the extreme opposite, i.e., the limit of infinite dimensions, will be examined.

At this point some general remarks about the properties and limitations of the Hubbard model are appropriate. First the symmetry of the Hubbard model shall be illuminated. In addition to the purely geometrical symmetries of the underlying lattice, it is easy to see that the Hamiltonian 2.3 shows spin-rotational invariance. This means that any form of magnetic ordering that can arise (cf. the discussion in Sec. 2.3) must be regarded as a spontaneous breaking of this symmetry. Furthermore, the model exhibits time-reversal invariance in the absence of magnetic fields. Depending on the chosen lattice, also electron-hole symmetry is possible [Fazekas99a]. Note that for the system $1T$-TaSe$_2$ investigated in Chapter 4 this is not the case.

One of the most drastic simplifications of this *one-band* Hubbard model — besides the artificial truncation of the Coulomb repulsion — is that only the electrons of a single orbital are considered. It must be kept in mind that in the systems of interest the partially filled d shells are often characterized by orbital degeneracy, which is an important source of more complicated behavior.

Having presented the limits of either t or U being zero, the discussion of the intermediate regime is now commenced, coming from the atomic limit where the Hubbard U dominates the parameter t. If hopping from site to site is allowed for, the picture drawn in Fig. 2.2 (b) will change in the sense that a small fraction of sites will become occupied with two electrons. The diagram of Panel (c) shows what energetic configurations can arise as a consequence of the hopping processes. The sites with single occupation are characterized by their atomic energy, which is labelled ϵ_{at}. Electron pairs in the same orbital, on the other hand, have the energy $\epsilon_{at} + U$, since the local Coulomb energy has to be paid in this case. The level scheme is thus occupation-dependent: The existence of the upper energy level depends on the presence of electrons in the lower level. In the solid the excitations, viz., both the double occupation and the hole left behind, can propagate through the crystal. However, they will be scattered at the internal degrees of freedom like spin, or orbital angular momentum (not included in the simple Hubbard Hamiltonian 2.3). Consequently, a broadening into the incoherent, so-called lower and upper Hubbard bands will set in, as sketched in Panel (c) of Fig. 2.2. It is underlined that the emergence of the Hubbard bands is a many-particle effect. The Hubbard bands must therefore not be interpreted in the usual semiconductor band picture. The difference becomes obvious when the number of states in a Hubbard band is considered. While an ordinary band of a crystal with N sites can host $2N$ electrons, a full Hubbard band contains only N electrons. Consequently, the density of states (DOS) is strictly speaking not a useful quantity for the description of the many-body electronic structure. Instead, the spectral function $A(E)$ can be used to take over this role, as it measures the probability of removing (adding) an electron from the many-particle system at the

energy E below (above) the Fermi level. Therewith it can be regarded as the counterpart of the density of states of the one-particle picture.

Limit of Infinite Dimensions

Amazingly, it is possible to gain more insight into the nature of the Hubbard model by considering the limit of $D = \infty$. In 1989 Metzner and Vollhardt were able to show that in this limit the diagrammatic treatment of the Hubbard model simplifies substantially, while the many-body nature is still preserved [Metzner89]. The advantage that the infinite-dimensional model offers can be understood by the following argument. The complexity of a many-particle problem is greatly reduced by applying a mean field theory: Instead of being forced to treat each single electron explicitly, for it is coupled with its neighbors, the system is mapped onto an effective one-body problem. While in a three-dimensional simple cubic system every site is coordinated by six nearest neighbors, the infinite-dimensional hypercubic lattice is characterized by an infinite coordination number. In this limit an electron can be imagined as interacting with a bath of non-interacting excitations — in other words, the mean field theory becomes exact. This is the basis for the dynamical mean field theory (DMFT).

Before its results with direct impact for the understanding of the Mott metal-insulator transition will be presented, a couple of particularities at $D = \infty$ shall be briefly addressed. If each site is connected to an infinite number of nearest neighbors that can be reached by a hopping process, the parameter t associated with this hopping must be scaled suitably, so that the kinetic energy does not diverge. A further important aspect that must be kept in mind when dealing with infinite dimensions is that certain familiar and useful concepts fail to hold any longer. One such example is the Fermi surface, which separates occupied and unoccupied regions in **k**-space. This concept is based on the smoothness in the **k**-dependence of the electronic energies, which is absent at $D = \infty$: Electronic states with nearby momenta possess completely uncorrelated energies [Fazekas99a].

By means of the dynamical mean field theory it became possible to fill the gap between the two extremes of the ratio U/W. For W dominating over U, the spectral function is characterized by a quasiparticle peak — while the two Hubbard subbands arise in the opposite limit $U/W \gg 1$, i.e., in a Mott insulator. The DMFT is able to realistically describe materials in the intermediate regime ranging from weakly correlated metals to Mott insulators. DMFT results of two calculations with different ratios U/W taken from Ref. [Bulla99] are plotted in Fig. 2.3. The spectrum with $U/W = 2$ lies on the insulating side of the transition. At the Fermi energy the intensity vanishes, the spectral weight is found instead in the lower and upper Hubbard bands separated by the energy U, as it was expected from the simple picture drawn in Fig. 2.2. When the value of U/W is lowered below the critical value of ≈ 1.4, a quasiparticle peak emerges at zero energy. The resulting three-peak structure shown for $U/W = 1$ can be regarded as being typical for a correlated metal. These two spectra illustrate how the spectral features, which can
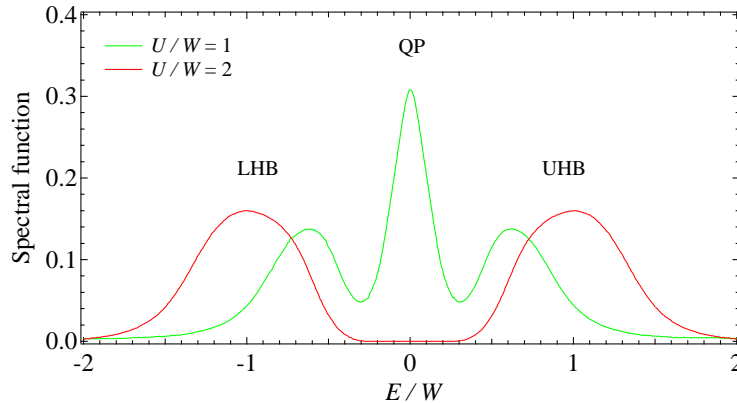
Figure 2.3: *Evolution of the spectral functions calculated in the dynamical mean field theory for the infinite-dimensional Hubbard model [Bulla99]. In the insulating regime, i.e., for $U/W = 2$, the spectrum consists of two features, the lower and upper Hubbard bands, located at the energetic positions $\pm\frac{1}{2}U$. Lowering U leads to a metal-insulator transition, so that for $U/W = 1$ a metallic spectrum results. As a third feature a quasiparticle (QP) peak appears at the Fermi energy.*

be measured by photoemission, evolve in the dynamical mean field theory solution of the Hubbard model at half-filling. A metal-insulator transition is observed that can be characterized by a transfer of spectral weight between the low-frequency quasiparticle peak and the high-frequency Hubbard subbands.

2.2 Charge Density Waves

A charge density wave is a broken-symmetry state that develops in low-dimensional metals as a consequence of electron-phonon interactions. In 1955 Peierls discovered that in one dimension (1D), a metallic state coupled to phonons is not stable at low temperatures. Interestingly, the relevance of this phenomenon for real physical systems was not clear at that time even to Peierls himself, as he describes in Ref. [Peierls91]:

> "This instability came to me as a complete surprise when I was tidying material for my book [Peierls55], and it took me a considerable time to convince myself that the argument was sound. It seemed of only academic significance, however, since there are no strictly one-dimensional systems in nature (and if there were, they would become disordered at any finite temperature [Peierls34]). I therefore did not think it worth publishing the argument, beyond a brief remark in the book (...)."

Today the *Science Citation Index Expanded* database [ISI06] counts approximately 2000 cited references for this brief remark, and several groups of organic and inorganic compounds are known that display this so-called Peierls instability.

Charge density waves can occur in materials with two- or even three-dimensional band structures, but they are basically a one-dimensional phenomenon [Grüner88]. However,

as was already touched upon in the above quote, a transition into a state with long-range ordering is not possible for a strictly one-dimensional system at finite temperatures. This is due to fluctuations of the order parameter [Peierls34, Landau79]. In real materials, weak interchain interactions and also three-dimensional phonons will always be present, so that the Peierls state with broken translational symmetry can survive at finite temperatures. Such systems are termed quasi-one-dimensional.

As it will be argued in the remainder of this section, the driving force of a charge density wave is the lowering of the *electronic* free energy. The related instability connected with a lowering of the *magnetic* free energy resulting in the so-called spin-Peierls transition originates from spin-phonon coupling and is treated in Section 2.3.

It is emphasized that the CDW instability is a cooperative phenomenon and can only be understood by inspecting the interplay between lattice and electronic system. This can be done from both viewpoints, i.e., starting from an unperturbed electronic system and considering the coupling to the phonons as perturbation, or vice versa. In this section both aspects will be illuminated. It commences with a brief presentation of the $2k_{\mathrm{F}}$-instability of the 1D free electron gas. The focus is then set on the phonon system, treating the electron-phonon coupling as a perturbation, which results in a renormalization of the phonon dispersion known as the Kohn anomaly. This is followed by a mean-field treatment where the roles are interchanged, thus showing how the electronic properties are altered in the presence of a perturbing potential induced by the interaction with phonons.

Response Function of the Free Electron Gas

In order to understand how the energy of the electronic system is lowered in a charge-Peierls system, it will be shown that a one-dimensional electron gas is unstable towards a perturbation with wave vector $2k_{\mathrm{F}}$. To this aim the response of the free electron gas to a time-independent potential with Fourier components $\phi(\mathbf{q})$ will be examined (boldface symbols denote three-dimensional vectors) [Grüner94]. If $\phi(\mathbf{q})$ is small it is a fair assumption that the Fourier components of the induced charge density $\rho^{\mathrm{ind}}(\mathbf{q})$ depend linearly on the perturbation, and one can write

$$\rho^{\mathrm{ind}}(\mathbf{q}) = \chi(\mathbf{q})\phi(\mathbf{q}). \tag{2.9}$$

The constant of proportionality $\chi(\mathbf{q})$ is the so-called Lindhard response function, which is given by

$$\chi(\mathbf{q}) = -e^2 \sum_{\mathbf{k}} \frac{f_{\mathbf{k}} - f_{\mathbf{k}+\mathbf{q}}}{\epsilon_{\mathbf{k}} - \epsilon_{\mathbf{k}+\mathbf{q}}}, \tag{2.10}$$

where $f_{\mathbf{k}} \equiv f(\epsilon_{\mathbf{k}})$ is the Fermi distribution. Evaluating this sum at zero temperature yields the results displayed in Fig. 2.4 (a). It can be seen that the response in one dimension is dramatically different from that obtained in higher dimensions: $\chi(\mathbf{q})$ diverges at $q = 2k_{\mathrm{F}}$ in the one-dimensional case, whereas this divergence is absent in two or three
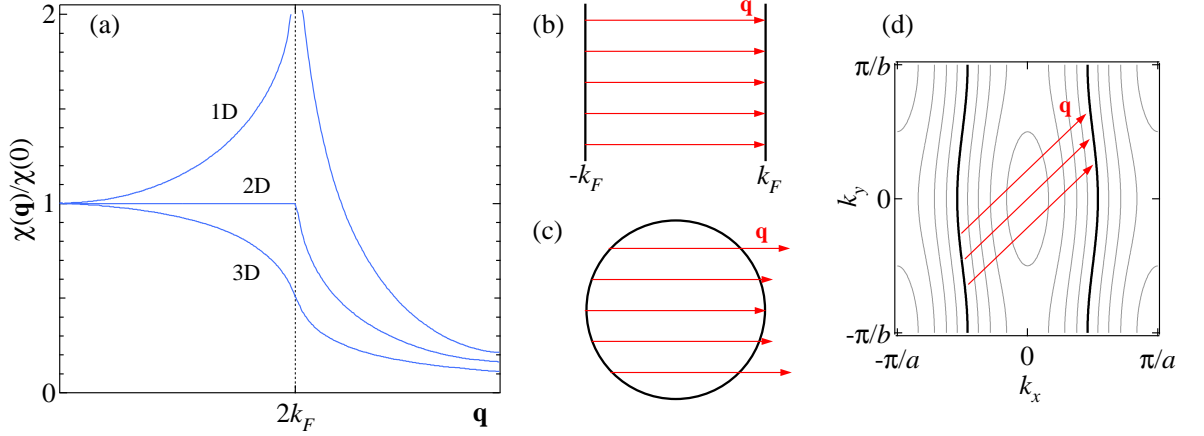
Figure 2.4: *(a) Lindhard response function χ for the one-, two-, and three-dimensional free electron gas at zero temperature as function of the wave vector $\mathbf{q}$ [Grüner94]. (b,c) Fermi surfaces of the one- and two-dimensional free electron gas. The arrows indicate electron-hole pairs differing by the wave vector $\mathbf{q}$ of length $2k_F$. (d) Contour plot of constant energy surfaces of a quasi-one-dimensional electron gas ($t_a/t_b = 8$). The Fermi surface is plotted as a thick black line and arrows indicate the partial nesting.*

dimensions. The logarithmic singularity of the one-dimensional electron gas is the origin of the Peierls instability, as it implies that an arbitrarily small external perturbation leads to a divergent charge density response. This suggests through self-consistency that the electron gas itself is unstable towards a periodic modulation of the charge density.

The underlying reason for this qualitative difference between one and higher dimensions can be understood from the Fermi surface topology. The largest contributions to the sum in Equation 2.10 come from pairs of states, one occupied and one empty, that are connected by the same wave vector $\mathbf{q}$ and differ only negligibly in energy. This condition can be fulfilled if large portions of the Fermi surface can be mapped onto other areas by translation with the same momentum vector $\mathbf{q}$. In one dimension, where the Fermi surface consists of two parallel planes $2k_F$ apart, this so-called nesting condition is perfectly fulfilled, as depicted in Fig. 2.4 (b). In Panel (c) it is shown that already in two dimensions only a vanishing fraction of the Fermi surface can be connected with the same wave vector. This causes the removal of the singularity in the response function. However, the possibility of a Peierls instability does also exist in two dimensions if a strong anisotropy of the electronic structure is given. In order to model such a system an electronic dispersion

$$\epsilon(\mathbf{k}) = \epsilon_0 - 2t_a \cos(k_x a) - 2t_b \cos(k_y b) \tag{2.11}$$

shall be assumed, with tight binding parameters $t_{a,b}$. The anisotropy is taken into account choosing $t_a \gg t_b$. Figure 2.4 (d) shows the Fermi surface that results from such a quasi-one-dimensional electronic dispersion. The resemblance to the 1D Fermi surface is apparent, and it can be seen that large parts of the Fermi surface fulfill the nesting

condition. With t_a/t_b approaching unity, this fraction will be diminished as the number of electron-hole pairs that contribute significantly to Equation 2.10 becomes smaller, leading to a gradual removal of the logarithmic singularity in the response function. In a real system, the Fermi surface will in general possess a much more complicated topology than that depicted in Fig. 2.4 (d). However, it is still possible — even in three dimensions — that parts of the Fermi surface nest with each other with the same effect discussed above.

The interaction of the electronic with the phonon system provides the perturbation that is responsible for the emergence of a broken-symmetry state in CDW systems. To illustrate this, an external potential ϕ^{ext} shall be considered, which leads to a density fluctuation ρ^{ind}, and — as a consequence of the electron-phonon coupling — to a potential ϕ^{ind} induced by ρ^{ind}. With the electron-phonon coupling constant $g < 0$ assumed to be momentum-independent, one can write

$$\phi^{\text{ind}}(\mathbf{q}) = -g\,\rho^{\text{ind}}(\mathbf{q}). \tag{2.12}$$

With Equation 2.9, the induced charge density can be expressed as

$$\rho^{\text{ind}}(\mathbf{q}) = \frac{\chi(\mathbf{q})\phi^{\text{ext}}(\mathbf{q})}{1 + g\,\chi(\mathbf{q})}. \tag{2.13}$$

This means that the system is unstable when $1 + g\,\chi(\mathbf{q})$ vanishes. At $T = 0$ the system will thus be subject to the Peierls instability if the electronic response function is sufficiently large. A CDW system is then characterized by a broken-symmetry state with a finite induced charge density ρ^{ind}.

Up to this point, only the case $T = 0$ was discussed. Finite temperatures have the effect of attenuating the singularity of the electronic response. It is thus clear that raising the temperature will eventually lead to a phase transition, usually referred to as Peierls transition, into a state with unbroken symmetry.

As pointed out, in CDW systems electron-phonon coupling is responsible for the formation of electron-hole pairs. A closely related phenomenon that can be caused by electron-phonon coupling is the formation of electron-electron pairs leading to superconductivity. If the circle is drawn wider and a generic interaction potential is assumed, even more possible instabilities come into view. The nature of the adopted ground state depends on the detailed interaction potential and its $\mathbf{q}$-dependence. In Table 2.1 the four possibilities of pair formation are summarized that occur considering a one-dimensional metal. In this case, the Fermi surface simply consists of two points at $\pm k_{\text{F}}$. The first two of these states involve electron-electron pairing: Cooper pairs with total momentum $q = 0$ are formed in the ground state of the singlet or triplet superconductors. In the last two states electron-hole pairing with a finite momentum $q = 2k_{\text{F}}$ leads to a periodic modulation of the charge and spin density. The latter phenomenon is the so-called spin density wave and is caused by the electron-electron interaction.

Table 2.1: *Possible broken symmetry ground states of one-dimensional metals. Electrons and holes are denoted by e and h, respectively, the subscripts 1 and 2 refer to the two points of the Fermi surface at $\pm k_F$, and arrows indicate the spin orientation.*

Ground state	Paring	Total Spin	Total Momentum
singlet superconductor	$e_{1\uparrow}$, $e_{2\downarrow}$	$S = 0$	$q = 0$
triplet superconductor	$e_{1\uparrow}$, $e_{2\uparrow}$	$S = 1$	$q = 0$
charge density wave	$e_{1\uparrow}$, $h_{2\uparrow}$	$S = 0$	$q = 2k_{\mathrm{F}}$
spin density wave	$e_{1\uparrow}$, $h_{2\downarrow}$	$S = 1$	$q = 2k_{\mathrm{F}}$

Fröhlich Hamiltonian

Turning back to the charge density wave, another effect of the electron-phonon coupling has to be mentioned: Not only the electronic system is affected but also the lattice. The modulation of the charge density is always accompanied by a modulation of the lattice with the same periodicity. Both the renormalization of the electron and the phonon spectrum that are responsible for the according modulations can be understood by describing an electron gas coupled to the phonon system with the Fröhlich Hamiltonian [Fröhlich54]. The following treatment is motivated not only by its relevance for the CDW system 1T-TaSe$_2$, but also because the results can partly be applied to the spin-Peierls transition treated in Section 2.3 and, last but not least, it is apt to show very nicely the analogies between the charge-Peierls and the spin-Peierls transition.

The Fröhlich Hamiltonian consists of two parts, viz., the unperturbed Hamiltonian $\mathcal{H}_0$, describing the free electron gas and the phonon system, and the perturbation $\mathcal{H}_{\text{el-ph}}$, describing the electron-phonon interaction. The first part is given in second quantized notation as

$$\mathcal{H}_0 = \sum_{\mathbf{k}} \epsilon_{\mathbf{k}} c_{\mathbf{k}}^{\dagger} c_{\mathbf{k}} + \sum_{\mathbf{q}} \hbar \omega_{\mathbf{q}} b_{\mathbf{q}}^{\dagger} b_{\mathbf{q}}, \tag{2.14}$$

where the free electron gas is represented by the sum over the creation and annihilation operators $c_{\mathbf{k}}^{\dagger}$ and $c_{\mathbf{k}}$ for an electron with energy $\epsilon_{\mathbf{k}} = \hbar^2 k^2 / 2m$ and wave vector $\mathbf{k}$. The phonon part is described in terms of the corresponding bosonic operators $b_{\mathbf{q}}^{\dagger}$ and $b_{\mathbf{q}}$ of a phonon with energy $\hbar \omega_{\mathbf{q}}$ and wave vector $\mathbf{q}$. For simplicity only a single acoustic phonon branch with longitudinal polarization is considered. The interaction Hamiltonian is expressed in this notation as

$$\mathcal{H}_{\text{el-ph}} = \sum_{\mathbf{k},\mathbf{q}} g_{\mathbf{k}\mathbf{q}} (b_{-\mathbf{q}}^{\dagger} + b_{\mathbf{q}}) c_{\mathbf{k}+\mathbf{q}}^{\dagger} c_{\mathbf{k}}, \tag{2.15}$$

where $g_{\mathbf{k}\mathbf{q}}$ is the electron-phonon coupling constant. Summing up both contributions, the Fröhlich Hamiltonian reads

$$\mathcal{H}_{\text{Fröhlich}} = \sum_{\mathbf{k}} \epsilon_{\mathbf{k}} c_{\mathbf{k}}^{\dagger} c_{\mathbf{k}} + \sum_{\mathbf{q}} \hbar \omega_{\mathbf{q}} b_{\mathbf{q}}^{\dagger} b_{\mathbf{q}} + \sum_{\mathbf{k},\mathbf{q}} g_{\mathbf{k}\mathbf{q}} (b_{-\mathbf{q}}^{\dagger} + b_{\mathbf{q}}) c_{\mathbf{k}+\mathbf{q}}^{\dagger} c_{\mathbf{k}}. \tag{2.16}$$

(a)

(b)

Figure 2.5: *Diagrammatic representation of an electron scattered under emission (a) or absorption (b) of a phonon. In both cases the total wave number is conserved.*

The interaction can be viewed as consisting of two parts: Terms involving $b^{\dagger}_{-\mathbf{q}} c^{\dagger}_{\mathbf{k}+\mathbf{q}} c_{\mathbf{k}}$ and terms involving $b_{\mathbf{q}} c^{\dagger}_{\mathbf{k}+\mathbf{q}} c_{\mathbf{k}}$. The underlying physical processes are visualized in Fig. 2.5. In the diagram (a), an electron with wave number $\mathbf{k}$ is scattered into a state with $\mathbf{k}+\mathbf{q}$ under emission of a phonon with wave number $-\mathbf{q}$. Panel (b) shows the corresponding diagram where a phonon with wave number $\mathbf{q}$ is absorbed in the scattering process.

Kohn Anomaly

The renormalization of the phonon dispersion can be derived using perturbation theory [Taylor02]. The total energy of the Fröhlich Hamiltonian to second order in $\mathcal{H}_{\text{el-ph}}$ can be written as

$$\epsilon = \epsilon_0 + \langle\Psi|\,\mathcal{H}_{\text{el-ph}}\,|\Psi\rangle + \langle\Psi|\,\mathcal{H}_{\text{el-ph}}(\epsilon_0 - \mathcal{H}_0)^{-1}\mathcal{H}_{\text{el-ph}}\,|\Psi\rangle, \tag{2.17}$$

where ϵ_0 is the unperturbed energy of the state Ψ with $n_{\mathbf{q}} = b^{\dagger}_{\mathbf{q}} b_{\mathbf{q}}$ phonons in the longitudinally polarized mode $\mathbf{q}$ and $n_{\mathbf{k}} = c^{\dagger}_{\mathbf{k}} c_{\mathbf{k}}$ electrons in state $\mathbf{k}$. It can be easily seen that the first order term vanishes. The interaction Hamiltonian $\mathcal{H}_{\text{el-ph}}$ contains only terms that either destroy or create one phonon, so that $\mathcal{H}_{\text{el-ph}}\,|\Psi\rangle$ is orthogonal to $|\Psi\rangle$. This argument does not apply to the second term, since a phonon destroyed by the first operator $\mathcal{H}_{\text{el-ph}}$ can be replaced by the second $\mathcal{H}_{\text{el-ph}}$, and vice versa. A typical scattering event contributing to the second-order term is depicted in Fig. 2.6 (a): An electron is scattered from state $\mathbf{k}$ into state $\mathbf{k}+\mathbf{q}$ under absorption of a phonon with wave vector $\mathbf{q}$. The electron is then scattered back into its original state associated with the re-emission of a phonon, again with wave vector $\mathbf{q}$, so that the total momentum is conserved.

The resulting total energy of second order perturbation theory can be used to determine the perturbed phonon frequency $\omega_{\mathbf{q}}^{(\text{p})}$, as it can be identified with the energy required to create one phonon:

$$\hbar\omega_{\mathbf{q}}^{(\text{p})} = \frac{\partial\epsilon}{\partial\langle n_{\mathbf{q}}\rangle} = \hbar\omega_{\mathbf{q}} - \sum_{\mathbf{k}} 2|g_{\mathbf{k}\mathbf{q}}|^2 \frac{\langle n_{\mathbf{k}+\mathbf{q}}(1-n_{\mathbf{k}})\rangle}{\epsilon_{\mathbf{k}} - \epsilon_{\mathbf{k}+\mathbf{q}}}, \tag{2.18}$$

where $n_{\mathbf{k}} = c^{\dagger}_{\mathbf{k}} c_{\mathbf{k}}$ and $n_{\mathbf{q}} = b^{\dagger}_{\mathbf{q}} b_{\mathbf{q}}$ are the number operators for electrons and phonons, respectively.

The origin of this renormalization can be understood redrawing the diagram shown in Fig. 2.6 (a) in the form of Fig. 2.6 (b), which focusses on the role of the phonon. Here
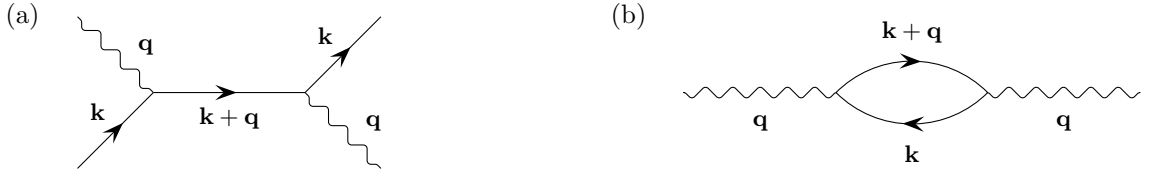
Figure 2.6: *Two equivalent diagrams describing the same scattering process that contributes to the energy of the electron-phonon system in second order perturbation theory. (a) An electron is scattered under absorption and re-emission of a phonon. (b) A phonon is annihilated and re-created involving a virtual electron-hole pair.*

the first scattering event is viewed as the creation of an electron hole pair. To formulate the key point of this diagram, one can say that the phonon spends part of its time as a virtual electron-hole pair, and through this process its energy is renormalized.

In this form the phonon renormalization is reminiscent of the expression for the electronic response function in Equation 2.10. Again, the most significant contributions to the sum come from pairs of states, one occupied and one empty, which differ by the same wave vector $\mathbf{q}$ and possess the same energy. Similarly to the discussion that followed Equation 2.10, where the topology of the Fermi surface in one dimension was found to be the origin of the singularity in the response function, one can now argue that the Fermi surface topology plays a crucial role in determining the phonon renormalization. Consequently, the dimensionality strongly influences the outcome, as it can be seen in Fig. 2.7 (a): In three dimensions it is only the derivative $\partial\omega_{\mathbf{q}}^{(p)}/\partial\mathbf{q}$ that diverges when the phonon wave vector is equal to the diameter of the Fermi surface. In other words, a kink appears in the phonon dispersion. This effect is known as the Kohn anomaly. In one dimension this effect is much more pronounced, the sum in Equation 2.18 actually diverges at zero temperature, which is of course unphysical. However, on its way to negative infinity the phonon frequency must pass through zero, and this simply means that the lattice becomes statically distorted. At finite temperatures, the sum shows no divergence. Upon cooling the phonon is said to "soften", i.e., its frequency is lowered, until it finally reaches zero, indicating a "frozen-in" lattice distortion. This static distortion, caused by a macroscopically occupied phonon mode, is then energetically favored by the system. As it will be shown, an electronic band gap opens at the Peierls transition, in this way prohibiting the sum in Equation 2.18 from the unphysical divergence.

Mean-Field Treatment

Having examined the effect of the electron-phonon coupling on the *phonon* dispersion, which finally led to the Kohn anomaly, in the following it will be shown how the *electron* dispersion is altered. To this aim a mean-field approach will be applied to the case of a CDW system, in close analogy to the BCS treatment of low-temperature superconductors. However, one has to keep in mind that serious deviations from the mean field treatment cannot be excluded because of the necessarily low-dimensional character of a
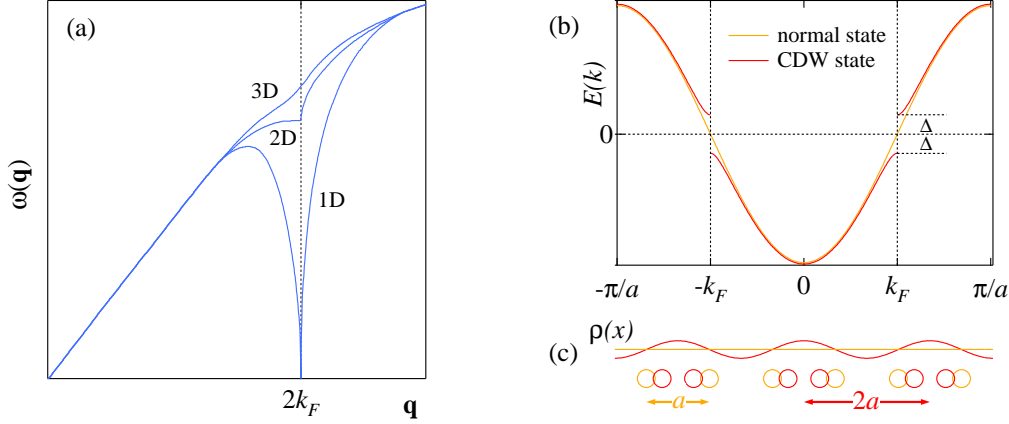
Figure 2.7: *(a) Acoustic phonon dispersion relation for one-, two-, and three-dimensional metals as function of the wave vector $\mathbf{q}$ [Grüner94]. The renormalization at $2k_F$ is known as the Kohn anomaly. (b) Tight binding electron band for a one-dimensional system. A band gap of $2|\Delta|$ opens at $\pm k_F$ in the Peierls state. (c) Electron density and atomic positions for a one-dimensional system. In the Peierls state a charge density wave develops, accompanied by a periodic lattice distortion.*

Peierls system.

The Fröhlich operator 2.16 can be simplified using a mean-field approximation, i.e., by replacing the boson operators $n_{\mathbf{q}}$, $b_{\mathbf{q}}$, and $b_{\mathbf{q}}^\dagger$ by their expectation values $\langle n_{\mathbf{q}} \rangle$, $\langle b_{\mathbf{q}} \rangle$, and $\langle b_{\mathbf{q}}^\dagger \rangle$. Note that, in contrast to the normal metallic state, the expectation values $\langle b_{\mathbf{q}} \rangle$ and $\langle b_{\mathbf{q}}^\dagger \rangle$ do not vanish below the Peierls transition due to the existence of macroscopically occupied phonon modes. They are thus well suited to define an order parameter. In the following the discussion is limited to the one-dimensional case, and the order parameter is defined as

$$\Delta e^{i\phi} = g_{2k_{\mathrm{F}}} \left(\langle b_{2k_{\mathrm{F}}} \rangle + \langle b_{-2k_{\mathrm{F}}}^\dagger \rangle \right), \tag{2.19}$$

where Δ shall be chosen to be real. Applying the mean field replacements, the Fröhlich Hamiltonian reads

$$\mathcal{H} = \sum_k \epsilon_k c_k^\dagger c_k + \sum_q \hbar \omega_q \langle b_q^\dagger b_q \rangle + \sum_{k,q} g_q \langle b_{-q}^\dagger + b_q \rangle c_{k+q}^\dagger c_k, \tag{2.20}$$

and the sum over q now contains only the values $\pm k_{\mathrm{F}}$. Using $\langle b_{2k_{\mathrm{F}}} \rangle = \langle b_{-2k_{\mathrm{F}}}^\dagger \rangle$ and $g_{2k_{\mathrm{F}}} = g_{-2k_{\mathrm{F}}}$, the electronic part of the Hamiltonian can be written as

$$\mathcal{H}_{\mathrm{el}} = \sum_k \epsilon_k c_k^\dagger c_k + 2g_{2k_{\mathrm{F}}} \sum_k \left[\langle b_{-2k_{\mathrm{F}}}^\dagger \rangle c_{k+2k_{\mathrm{F}}}^\dagger c_k + \langle b_{-2k_{\mathrm{F}}} \rangle c_{k-2k_{\mathrm{F}}}^\dagger c_k \right]. \tag{2.21}$$

With the order parameter introduced above, the electronic part of the Hamiltonian becomes

$$\mathcal{H}_{\mathrm{el}} = \sum_k \left[\epsilon_k c_k^\dagger c_k + \Delta e^{i\phi} c_{k+2k_{\mathrm{F}}}^\dagger c_k + \Delta e^{-i\phi} c_{k-2k_{\mathrm{F}}}^\dagger c_k \right]. \tag{2.22}$$

This is a typical mean-field Hamilton operator and strongly resembles the model Hamiltonian for a low-temperature superconductor, described for example in Ref. [Tinkham75]. The major difference to the case of superconductivity, however, lies in the fact that in Equation 2.22 the order parameter is connected with the occurrence of electron-hole pairs, whereas superconductivity is based on the formation of electron-electron pairs, viz., the Cooper pairs (cf. Table 2.1).

The mean-field Hamiltonian can be diagonalized utilizing a canonical transformation [Grüner94] — the counterpart of the Bogoliubov transformation in normal BCS theory. For the detailed solution the reader is referred to the extensive BCS treatment in the literature for the superconducting state. As a direct result of the canonical transformation the excitation spectrum is obtained. An energy gap 2Δ is introduced in the electron band structure so that the one-electron energies E_k become

$$E_k = \text{sgn}(\epsilon_k) \left(\epsilon_k^2 + \Delta^2 \right)^{1/2} , \tag{2.23}$$

where ϵ_k, the unperturbed single electron energy, is measured from the Fermi level. This result is plotted in Fig. 2.7 (b). The order parameter $\Delta e^{i\phi}$ can either be viewed as describing the lattice distortion, as it was introduced above, or, alternatively, be identified with the band gap.

Another straightforward output of the mentioned transformation is the charge density being periodically modulated in the Peierls state, depicted in Fig. 2.7 (c) together with the static distortion of the underlying lattice. In one dimension it is especially simple to understand the nature of the Peierls instability: Then k_F lies exactly halfway between Γ and the Brillouin zone boundary, and the lattice distortion is simply a dimerization. A new periodicity is thus introduced, and Bragg scattering of the electron states at the new Brillouin zone boundaries leads to the opening of the electronic band gap. Accordingly, in the one-dimensional case, the Peierls transition is a metal-insulator transition. In a quasi-one-dimensional system this is not necessarily the case. Only parts of the Fermi surface will be gapped, and the electronic energy gain of this partial gapping can be sufficient to trigger the Peierls transition. This CDW state is then still characterized by a metallic conductivity. Another qualitative difference can be inferred from Fig. 2.4 (d). In contrast to a purely one-dimensional system, the nesting vector and consequently the CDW periodicity will in general not be commensurate with the lattice. It shall be noted, however, that the coupling of the periodic lattice to the charge density wave favors commensurate modulations. If the two periods are close to being commensurate, the system lowers its energy via a lock-in transition from an incommensurate to a commensurate state as the CDW snaps in with the lattice periodicity.

With the obtained energy dispersion relation 2.23, it is an easy task to determine the energy gain of the 1D electronic system

$$E_\text{el} = \sum_k (\epsilon_k - E_k). \tag{2.24}$$

In the weak coupling limit, where $\epsilon_F \gg \Delta$, evaluating Equation 2.24 leads to an electronic energy gain proportional to $\Delta^2 \ln(W/\Delta)$, where W is the electronic bandwidth. This value has to be compared to the elastic energy of the lattice distortion, which is proportional to the square of the displacement amplitudes and thus to Δ^2. It becomes clear that at zero temperature the one-dimensional metal is unstable towards the development of a Peierls distortion if Δ is sufficiently small — the lowering of the electronic energy outweighs the energy cost to distort the lattice.

The condensation energy can be used to calculate the magnitude of the order parameter, and thus one obtains that the famous relation of the BCS theory in the weak coupling regime also applies to the case of a charge-Peierls transition:

$$2\Delta(0) = 3.52\, k_{\mathrm{B}} T_c \tag{2.25}$$

Another important BCS result directly translates to the CDW case, namely the temperature dependence of the order parameter. Close to the transition temperature, where the gap approaches zero, the behavior can be approximated as

$$\frac{\Delta(T)}{\Delta(0)} = 1.74 \left(1 - \frac{T}{T_c} \right)^{1/2}. \tag{2.26}$$

Also the temperature dependence of the specific heat $C(T)$ follows the behavior of a BCS superconductor. At low temperatures it is exponentially suppressed due to the electronic gap. Directly at T_c it shows a finite discontinuity proportional to its value C_n in the normal metallic state, which is linear in T for a free electron gas. The jump is thus given by

$$\Delta C = 1.43\, \gamma T_c = 1.43\, C_n(T_c), \tag{2.27}$$

where γ is the Sommerfeld constant.

At this point, a critical statement concerning the above BCS results is appropriate: The mean-field treatment of a one-dimensional system leads to a finite transition temperature below which long-range order develops. This is an artefact of the mean-field approximation that averages out fluctuations of the order parameter. However, in highly anisotropic systems these fluctuations become important, culminating in the absence of long-range order at finite temperatures in strictly one-dimensional systems [Landau79]. As pointed out before, in real systems there exists always a finite interchain coupling, and a transition into a charge density wave state becomes possible at finite temperatures. However, for a strongly anisotropic system the transition temperature T_c^{3D} will be significantly reduced from its mean-field value T_c^{MF}. The temperature regime between T_c^{3D} and T_c^{MF} will be dominated by fluctuations and a development of short-range order can be observed.

2.3 Spin-Peierls Instability

The spin-Peierls transition closely resembles the charge-Peierls transition described in the previous section. Both instabilities are basically one-dimensional phenomena and therefore occur in quasi-one-dimensional chains. In both cases, the instability involves a periodic lattice distortion, which in the simplest case corresponds to a dimerization of lattice sites. Another parallel is the thermodynamic description, which is almost identical for the two transitions. However, the origins of these two phase transitions are of completely different nature. Whereas a charge density wave system draws the energy gain from the electronic system, the spin-Peierls instability is a magneto-elastic effect in antiferromagnetic (AFM) insulating spin chains, where a lowering of the magnetic free energy is achieved by the formation of spin singlet pairs.

The first materials to display the spin-Peierls transition were discovered in the 1970s. Several *organic* compounds were found to be subject to this instability, which benefits from the soft lattice vibrations in organic materials — the Peierls distortion is thus less costly. Another favorable property in these compounds is the typically large distance between neighboring chains. One famous example is the organic charge transfer salt TTF-CuBDT with a transition temperature $T_c = 12K$ [Moncton77]. TTF stands for tetrathiafulvalene and is the organic donor for the copper bisdithiolene complex CuBDT. In 1993 the *inorganic* $CuGeO_3$ was discovered as a spin-Peierls system [Hase93]. For almost ten years, it remained the only known inorganic compound, for which the spin-Peierls state was unambiguously established, until in 2002 the oxychloride TiOCl, subject of this thesis, was interpreted as another realization of a spin-Peierls system [Seidel03].

To get a qualitative picture of the spin-Peierls instability, an assembly of quantum spin chains is considered, where the spins interact only via nearest neighbor exchange of antiferromagnetic type. The coupling of spins on different chains be not included. Spin-phonon coupling is a necessary ingredient, as the separation between successive spins will influence the exchange constant. The ground state of this system is comprised of a dimerized lattice, where the ions are displaced from their uniform locations, so that they move alternately closer and further apart. The magnetic energy of the system is then minimized by forming magnetic singlets of spin pairs. Exciting the system from the singlet ground state into a triplet state is connected with an energetic cost, termed the spin gap. The presence of this gap is a quantum effect — the classical Heisenberg model for an alternating spin chain does not yield a spin gap.

Heisenberg Hamiltonian

In order to get a deeper understanding of this phenomenon, one has to take a look at the Hamiltonian that is typically chosen to represent this physical situation, viz., the Heisenberg Hamiltonian, and spend a few thoughts about its possible ground states.

The Heisenberg Hamiltonian describing the low energy fluctuations of a set of interacting spins can be derived from the Hubbard Hamiltonian 2.3 for half-filling in the

strong coupling limit. In this limit the onsite Coulomb repulsion U is much larger than the hopping energy t, and thus enforces single occupancy of each site. The kinetic energy term $\mathcal{T}$ can be treated as a small perturbation compared to the Coulomb term $\mathcal{U}$. In zeroth order the resulting ground state is highly degenerate, as the spin of each electron can point both up or down. For N sites, all 2^N eigenstates $|\Psi\rangle$ of $\mathcal{U}$ with eigenvalue $\epsilon_0 = \langle\Psi|\mathcal{U}|\Psi\rangle = 0$, having the general form $c_{1\sigma_1}^\dagger c_{2\sigma_2}^\dagger \ldots c_{N\sigma_N}^\dagger |0\rangle$, contribute to the unperturbed ground state. This enormous degeneracy remains unchanged by the hopping term in first order: $\epsilon_1 = \langle\Psi|\mathcal{T}|\Psi\rangle = 0$, since each term of $\mathcal{T}$ acting on a purely singly-occupied state must produce an orthogonal state with one double occupation. Therefore, the second order term in $\mathcal{T}$ is required to lift the degeneracy, which reads

$$\epsilon_2 = \langle\Psi|\,\mathcal{T}(\epsilon_0 - \mathcal{U})^{-1}\mathcal{T}\,|\Psi\rangle . \tag{2.28}$$

The factor $(\epsilon_0 - \mathcal{U})^{-1}$ measures the lifetime of the intermediate states $\mathcal{T}|\Psi\rangle$. For any $|\Psi\rangle$ the same eigenvalue $(-U)^{-1}$ is obtained. This means that the energy shift ϵ_2 of any state with only singly-occupied sites is the same as that resulting from an effective Hamiltonian

$$\mathcal{H}_{\text{eff}} = -\mathcal{T}^2/U = -\frac{t^2}{U}\sum_{\langle ij\rangle\sigma}\sum_{\langle kl\rangle\sigma'} \left(c_{i\sigma}^\dagger c_{j\sigma} + c_{j\sigma}^\dagger c_{i\sigma}\right)\left(c_{k\sigma'}^\dagger c_{l\sigma'} + c_{l\sigma'}^\dagger c_{k\sigma'}\right), \tag{2.29}$$

where $\langle ij\rangle$ denotes a summation over nearest-neighbors, and every pair shall be counted only once. The site indices i, j, k, and l have to be chosen such that one arrives again at a state with one electron on each site, which yields

$$\mathcal{H}_{\text{eff}} = -\frac{t^2}{U}\sum_{\langle ij\rangle\sigma\sigma'}\left(c_{i\sigma}^\dagger c_{j\sigma}c_{j\sigma'}^\dagger c_{i\sigma'} + \text{h.c.}\right). \tag{2.30}$$

The corresponding hopping processes of this Hamiltonian can be viewed as one electron hopping to a neighboring site, briefly doubly occupying it, and then one of the two electrons hopping back as depicted in Fig. 2.8. Due to the Pauli exclusion principle, two electrons cannot occupy the same site if their spins point in the same direction. Consequently, only two neighboring electrons with antiparallel spins are able to profit from the hopping process. This arrangement is thus preferred to the parallel one — the system can be described by an antiferromagnetic exchange constant.

Introducing the spin operators[2] $S_i^z = \frac{1}{2}(n_{i\uparrow} - n_{i\downarrow})$, $S_i^+ = c_{i\uparrow}^\dagger c_{i\downarrow}$, and $S_i^- = c_{i\downarrow}^\dagger c_{i\uparrow}$, one can rewrite Equation 2.30 to obtain the usual form of the Heisenberg Hamiltonian

$$\mathcal{H}_{\text{Heisenberg}} = J\sum_{\langle ij\rangle}\left(\mathbf{S}_i \cdot \mathbf{S}_j - \tfrac{1}{4}\right), \tag{2.31}$$

with the Heisenberg interaction $J = 4t^2/U$ per bond. The constant offset of $\frac{1}{4}$ can be omitted, as it merely shifts the zero of energy.

---

[2]Note that $\hbar = 1$ is chosen in this section to permit the simple form 2.31 of the Heisenberg Hamiltonian.
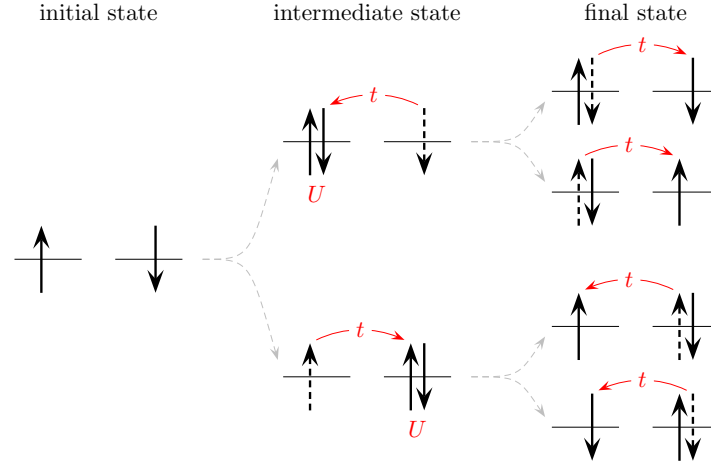
Figure 2.8: *Hopping processes of second order perturbation theory for a lattice with only two sites. Starting from a state with spin up on the left site and and spin down on the right site, the four possibilities are sketched that lead again to a state without double occupancy. Only these four terms can contribute to the sum in Equation 2.29. Each process is composed of two hops of energy t and involves an intermediate state of energy U, so that its energy contribution is $-t^2/U$. In total, the four processes lower the energy of the system by $-4t^2/U$.*

The Heisenberg Hamiltonian is not limited to AFM systems — it is able to describe ferromagnetic (FM) exchange as well by choosing a negative exchange constant. For a Heisenberg ferromagnet it is a simple task to find the ground state. Inspired by classical spins, one would expect the configuration with all spins aligned parallel to each other as the state with the lowest energy. Indeed, the state where each spin is maximally polarized in the same direction is an eigenstate of the Hamiltonian 2.31, and it can be shown that this is actually the ground state.

The situation is quite different for a Heisenberg antiferromagnet. Assuming a bipartite lattice, the obvious guess for the ground state is the Néel state depicted in Fig. 2.9 (a), with the spins on each sublattice ferromagnetically aligned, however with opposite sublattice magnetizations. For classical spins, this would yield the lowest possible energy, as each spin is surrounded by spins oppositely directed. This is still true for the Ising model, where the scalar product of the quantum-mechanical spins $\mathbf{S}_i \cdot \mathbf{S}_j$ of the Heisenberg Hamiltonian is replaced by the product of the z-components $S_i^z S_j^z$. In the AFM Heisenberg model, however, this state is not even an eigenstate. The spin-flip terms $S_i^+ S_j^-$ and $S_i^- S_j^+$ do not vanish, as in the ferromagnetic case, but produce a state, where a spin's z-component in one sublattice is reduced by unity, and that of another is raised. Consequently, this state is not an eigenstate.

To illustrate this in form of a simple example, the case of two interacting spins with $S = 1/2$ is considered. The corresponding Hamiltonian reads

$$\mathcal{H} = J\mathbf{S}_1 \cdot \mathbf{S}_2 = JS_1^z S_2^z + \frac{J}{2}\left(S_1^+ S_2^- + S_1^- S_2^+\right). \tag{2.32}$$
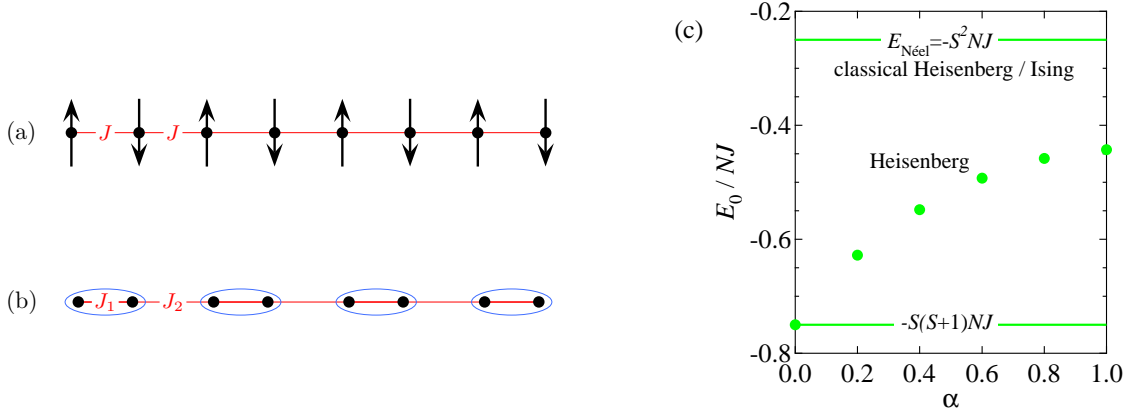
Figure 2.9: *Ground states of an antiferromagnetic spin chain. (a) Néel state of a spin chain with a uniform exchange interaction J. (b) Dimerized state of an alternating spin chain with intradimer exchange J_1 and interdimer exchange J_2. (c) Ground state energies of an alternating spin-1/2 chain as a function of the amount of dimerization $\alpha = J_2/J_1$. The average exchange $J = \frac{1}{2}(J_1 + J_2)$ is kept constant. The Heisenberg results for $\alpha = 0.2, 0.4, 0.6, 0.8$ are taken from Ref. [Duffy68]. $E_0(\alpha = 1)$ is the exact Bethe result, and $E_0(\alpha = 0)$ is the exact result for spin singlets according to Equation 2.33.*

Applying this Hamiltonian to the Néel state gives $\mathcal{H} \left| \uparrow\downarrow \right\rangle = -\frac{J}{4} \left| \uparrow\downarrow \right\rangle + \frac{J}{2} \left| \downarrow\uparrow \right\rangle$, a linear independent state. The energy of this state is $E_{\text{Néel}} = -0.25J$, equal to the result for classical spins.

The ground state of this system is the spin singlet $\left| \Psi_{\text{singlet}} \right\rangle = -\frac{1}{\sqrt{2}}(\left| \uparrow\downarrow \right\rangle - \left| \downarrow\uparrow \right\rangle)$. Its energy is

$$E_{\text{singlet}} = \left\langle \Psi_{\text{singlet}} \right| \mathcal{H} \left| \Psi_{\text{singlet}} \right\rangle = \frac{1}{2}\left(-\frac{J}{4} - \frac{J}{4} - \frac{J}{2} - \frac{J}{2}\right) = -0.75J, \qquad (2.33)$$

where the first two terms stem from the z-z, or Ising, part of the Heisenberg interaction, and the latter two from the spin-flip part. From this example it becomes clear that strict antiparallel alignment only gains energy from the Ising part of the Hamiltonian. However, a lower energy can be obtained by letting the spins fluctuate, so that also the spin-flip part of the Hamiltonian is utilized. This also applies to the general case of a spin-S bipartite lattice. Again the Néel state is higher in energy than the true ground state, and also a lower bound for the ground state energy E_0 can be found [Ashcroft76]:

$$- S(S + 1)NJ \leq E_0 \leq -NS^2J, \qquad (2.34)$$

where N counts the number of nearest-neighbor bonds. From this inequation one can see why a system with low spin behaves differently as a classical spin system. In the limit of large spin, when the spins resemble classical spins, the bounds become equal, and the neel state is a good approximation to the ground state. In the other limit, i.e., for $S = 1/2$, these bounds leave much more freedom for the system, as Equation 2.34 becomes $-0.75NJ \leq E_0 \leq -0.25NJ$. Except for the special case of a one-dimensional spin-1/2 chain, which Bethe showed to have a ground state energy $E_0 = -0.443NJ$

[Bethe31], finding a solution to the ground state problem is not yet solved in the general case. From the above two-site example, however, one can learn that it is advantageous for the system to form dimers, and this tendency increases for small spins. The effect is further enforced if the spins are given the possibility to distort the lattice, so that the interaction strength of a spin pair is raised. Depending on the detailed geometry of the lattice and of the exchange paths, this can lead to different ground states. Every pair of interacting spins would like to form a singlet, but a magnetic moment can only pair up with one other moment at a time. It was suggested by Anderson in 1973 that for a two dimensional spin-1/2 lattice, where a simple AFM order is frustrated, the ground state is defined by a linear combination of all possible singlets of the whole system. This state is termed the resonating valence bond state and will be presented in detail in Section 2.4.

Physical Picture of the Spin-Peierls Transition

A one-dimensional spin-1/2 chain is able to lower its energy in a much simpler way, opposed to the 2D RVB case. The energy can be minimized by distorting the lattice in such a way, that spin dimers with an enhanced exchange interaction are generated adjacent to each other. Magnetic singlets are then formed within these dimers, as depicted in Fig. 2.9 (b). This is the essence of a spin-Peierls transition. In a classical model, this effect cannot be understood, and also the Ising model does not support this possibility. It can be seen from Fig 2.9 (c), where the ground state energies of an alternating magnetic chain according to the different models is plotted, that only in the quantum Heisenberg model the free energy is lowered when the ratio of exchange constants $\alpha = J_2/J_1$ begins to deviate from unity, where J_1 and J_2 denote the intradimer and interdimer exchange, respectively. Moreover, one would not expect a spin-Peierls transition in a material with $S > 1/2$, since the importance of quantum fluctuations decreases rapidly with increasing magnetic moment and the upper and lower bound in Fig 2.9 (c) move closer together.

The initially mentioned analogy to the charge-Peierls transition has now become clear: While a CDW system minimizes its *electronic* free energy, a spin-Peierls system minimizes its *magnetic* free energy. In both cases, this is connected with a distortion of the lattice, but the energy cost of the distortion is outweighed by the energy gain of the electronic or magnetic system, respectively. The role of the electron-phonon coupling is taken over by the spin-phonon coupling.

The same considerations that were conducted in the context of the charge-Peierls transition can be applied to the spin-Peierls case: Also the spin-Peierls distortion is a one-dimensional phenomenon, and strictly speaking no broken-symmetry ground state is possible in one dimension. However, in nature the systems are only quasi-one-dimensional, as a finite interchain coupling will always be present. This may be due to non-vanishing exchange paths between the chains, or to the coupling of the magnetic moments to three-dimensional phonons.

Pseudofermion Representation

Formally, the similarity to a charge density wave can be seen by converting the spin operators into pseudofermion operators via the Jordan-Wigner transformation [Buzdin80, Pytte74, Bulaevskii63]. As a starting point, the model Hamiltonian

$$\mathcal{H} = \sum_j J_{j,j+1} \mathbf{S}_j \cdot \mathbf{S}_{j+1} + \sum_q \omega_q b_q^\dagger b_q \qquad (2.35)$$

for a one-dimensional spin-1/2 system is chosen including a term describing one-dimensional phonons. To minimize the number of indices, only a single phonon branch is considered. Note that an exact treatment would include three-dimensional phonons. To simplify matters, this will not be taken account of. The three-dimensional nature of the phonons will merely be seen as an implicit means of suppressing the one-dimensional fluctuations, thus enabling the possibility of a finite transition temperature [Bray83].

The destruction operator of the Jordan-Wigner transformation is defined as

$$\Psi_j = (-2)^{l-1} S_1^z S_2^z \ldots S_{j-1}^z S_j^-, \qquad (2.36)$$

and it is easily verified that these quasiparticles obey the anti-commutation rules of fermions $\{\Psi_j, \Psi_l\} = \delta_{jl}$. The spin operators in the Hamiltonian 2.35 can be substituted using the identities

$$S_j^+ S_{j+1}^- = \psi_j^\dagger \psi_{j+1} \qquad (2.37)$$

and

$$S_j^z = \tfrac{1}{2} - \psi_j^\dagger \psi_j. \qquad (2.38)$$

From the last equation the nature of these quasiparticles can be inferred. Instead of describing the spin state of a site as up or down, one can alternatively view the same situation as a site occupied or unoccupied with one pseudofermion. With these operators, the Hamiltonian now translates into

$$\mathcal{H} = \sum_j J_{j,j+1} \left[\tfrac{1}{2} \Psi_j^\dagger \Psi_{j+1} + \tfrac{1}{2} \Psi_{j+1}^\dagger \Psi_j - \Psi_j^\dagger \Psi_j + \Psi_j^\dagger \Psi_j \Psi_{j+1}^\dagger \Psi_{j+1} + \tfrac{1}{4} \right] + \sum_q \omega_q b_q^\dagger b_q. \quad (2.39)$$

At this point, two approximations will be applied, to further simplify the Hamiltonian. The first one concerns the spin-phonon coupling — the exchange interaction is expanded in first order in intersite spacing $(u_j - u_{j+1})$:

$$J_{j,j+1} = J + (u_j - u_{j+1}) \frac{\partial J_{j,j+1}}{\partial (u_j - u_{j+1})} \qquad (2.40)$$

After Fourier transforming the Hamiltonian 2.39 into k-space and rewriting the lattice displacements in second quantized notation in terms of phonon creation and destruction operators, the second approximation is applied: The Hartree approximation converts

the fermion-fermion interaction terms into single particle terms via the mean field assumption

$$\left\langle \Psi_k^\dagger \Psi_{k'} \right\rangle = f_k \delta_{kk'}, \tag{2.41}$$

where f_k is the Fermi distribution. Again, one has to keep in mind that a mean-field treatment is in general a poor approximation for a one-dimensional system. Neglecting the fluctuation effects leads to exaggerated transition temperatures, and in reality one expects a fluctuation regime between T_c^{3D} and T_c^{MF}.

With these approximations, the Hamiltonian

$$\mathcal{H} = \sum_k \epsilon_k \Psi_k^\dagger \Psi_k + \sum_q \omega_q b_q^\dagger b_q + \sum_{k,q} g_{kq}(b_{-q}^\dagger + b_q)\Psi_{k+q}^\dagger \Psi_k \tag{2.42}$$

is obtained. The pseudofermion energy is defined as

$$\epsilon_k = pJ \cos ka, \tag{2.43}$$

where a is the lattice constant and p is a dimensionless renormalization factor that is determined by the self-consistency condition

$$p = 1 - 2 \sum_k f_k \cos ka. \tag{2.44}$$

In the limit $T \ll J$, p is approximately constant with $p = 1.64$. The coupling constant g_{kq} is a function of the fermion and boson wave vectors k and q and furthermore depends on the gradient of the exchange constant $\partial J_{j,j+1}/\partial (u_j - u_{j+1})$.

The above Hamiltonian is nothing but the one-dimensional form of the Fröhlich Hamiltonian 2.16, which was used in the previous chapter as the basis for describing a charge density wave. As both systems can be described with the same Hamilton operator, it is obvious that a charge density wave is the corresponding spinless fermion system to a spin-Peierls system. The following discussion of the effect of finite temperatures is consequently analog to the one in the previous section.

Finite Temperatures

In the absence of a magnetic field, the band of pseudofermions is half-filled, the Fermi vector k_F thus lies in the exact center between Γ and the Brillouin zone boundary.[3] In one dimension the Fermi surface consists of only two points, whereas in higher dimensions it will adopt a more complicated topology. As derived for the CDW case, it follows from the form of a quasi-one-dimensional Fermi surface that the lattice is unstable towards a distortion with wave vector $2k_\mathrm{F}$. The Kohn anomaly, illustrated in Fig. 2.7, also develops

---

[3]To avoid confusion it shall be emphasized that a Fermi vector is only defined for the quasiparticles introduced by the Jordan-Wigner transformation. The electronic system certainly remains in an insulating state and does not possess a Fermi surface.
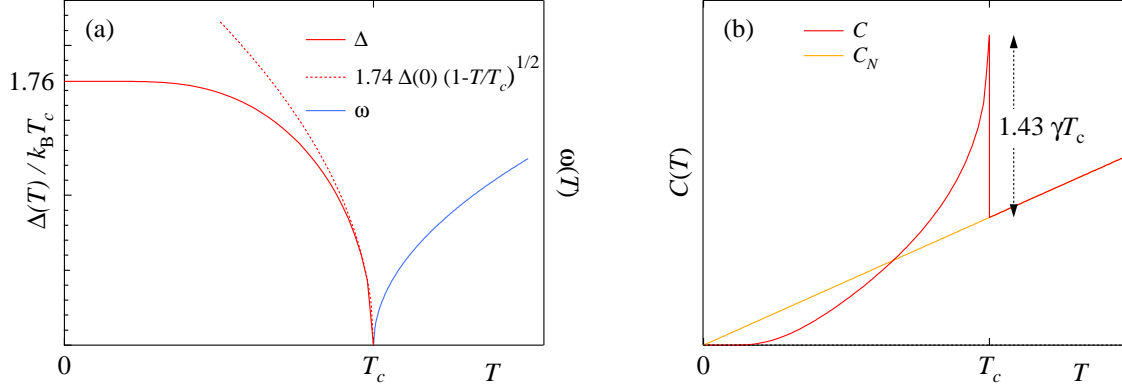
Figure 2.10: *Mean-field results for the thermodynamic properties of a spin-Peierls system in the weak-coupling regime. (a) Temperature dependence of the spin gap $\Delta(T)$ [Mühlschlegel59], of its approximation in the vicinity of the transition, and of the renormalized phonon frequency $\omega_{2k_F}^{(p)}(T)$. In the spin-Peierls phase the phonon state with wave vector $2k_F$ is macroscopically occupied as its energy vanishes below T_c. (b) Temperature dependence of the specific heat. A jump of magnitude $\Delta C = 1.43\, C_n(T_c)$ occurs at the transition temperature.*

in a spin-Peierls system. Upon cooling, the phonon with wave vector $2k_{\mathrm{F}}$ softens, until its energy completely vanishes at the spin-Peierls transition temperature, as depicted in Fig. 2.10 (a). Close to T_c the temperature dependence of the phonon frequency can be approximated by

$$\omega_{2k_{\mathrm{F}}}^{(\mathrm{p})}(T) \propto \left(\frac{T}{T_c} - 1\right)^{1/2}. \tag{2.45}$$

The spin gap Δ, i.e., the energy required to break up one magnetic singlet and to excite a triplet state, can be derived replacing the phonon operators by their expectation values in a mean-field approximation. The gap is then defined analog to Equation 2.19. In the weak coupling regime, where $T_c \ll J$, BCS theory can be applied yielding the zero temperature result

$$2\Delta(0) = 3.52\, k_{\mathrm{B}} T_c. \tag{2.46}$$

The temperature dependence of the gap is given implicitly by the BCS gap equation. The self-consistent solutions are tabulated in Ref. [Mühlschlegel59]. In the vicinity of T_c the gap obeys the square-root-like temperature dependence

$$\frac{\Delta(T)}{\Delta(0)} = 1.74 \left(1 - \frac{T}{T_c}\right)^{1/2}. \tag{2.47}$$

Both the spin gap and its approximation close to T_c are plotted in Fig. 2.10 (a). The increase of the gap width below T_c is responsible for a rapid suppression of the magnetic susceptibility with decreasing temperature.

The last BCS result to be mentioned here is the temperature dependence of the specific heat $C(T)$, displayed in Fig. 2.10 (b). It is exponentially damped by the spin gap $\Delta(T)$

below T_c. Not too far above T_c and disregarding lattice contributions, the specific heat is given by γT characteristic for a AFM Heisenberg chain with $\gamma = 2k_B^2/3J$ [Buzdin80]. Directly at T_c, BCS predicts a jump of 1.43 times the corresponding value in the normal state:

$$\Delta C = 1.43\,\gamma T_c = 1.43\,C_n(T_c) \tag{2.48}$$

Effect of an External Magnetic Field

In the absence of a magnetic field H, the band of pseudofermions is half-filled, as outlined above, and the system can benefit from the commensurability. To take account of an applied magnetic field, the term $g\mu_B H \sum_j \Psi_j^\dagger \Psi_j = g\mu_B H \sum_k \Psi_k^\dagger \Psi_k$ has to be added to the Hamiltonian 2.42, and the pseudofermion energy has to be replaced by

$$\epsilon_k = pJ\cos ka + g\mu_B H, \tag{2.49}$$

where g is the Landé factor. This effectively changes the chemical potential of the pseudofermions. The magnetic field thus maps onto the band filling of the corresponding spinless fermion system. This is in contrast to a CDW system, where the chemical potential is determined by the material parameters and cannot be varied at will. The spin-Peierls transition thus offers a possibility to study the role of commensurability effects very directly. Switching on an external magnetic field shifts the Fermi vector away from its commensurate value halfway between Γ and the Brillouin zone boundary. For small deviations, i.e., for weak magnetic fields, the system prefers to remain in the state with twice the period of its normal state in order to gain from the commensurability energy. A sufficiently low magnetic field will therefore not change the structure of the Peierls distortion, but it will reduce T_c [Cross79]. Increasing the field strength above a certain threshold can then take the system into an incommensurate state. For fields larger than a critical field H_c the spin-Peierls distortion will finally vanish. This is the case when the pseudofermion band is completely depleted and all spins are ferromagnetically aligned. The mean field result for the critical field [Bray83] is

$$\mu_B H_c \simeq 0.75\,k_B T_c. \tag{2.50}$$

2.4 Resonating Valence Bond Model

Having examined the properties of a one-dimensional spin-1/2 system in the previous section, the two-dimensional case of a quantum Heisenberg system with antiferromagnetic exchange will now be considered. Motivated by the rareness of experimental $S = 1/2$ systems with antiferromagnetic order, Anderson published his pioneering work [Anderson73] introducing the RVB state in 1973. This state is clearly distinct from the two other stable possibilities, the Néel state and the spin-Peierls state, which both break the symmetry of the high-temperature paramagnetic state in a phase transition at a temperature T_c. The RVB state is a precise singlet, has no obvious long-range order, and is

a fluid in the sense that it supports the quantum transport of spin excitations [Anderson87b].

In his original publication Anderson used the triangular lattice to illustrate the RVB state as an alternative possibility for the ground state of low-dimensional quantum spin systems. The term "resonating valence bonds" was inspired by the work of Pauling [Pauling33], who used linear combinations of bonding schemes to describe the valence states of aromatic molecular systems. While only limited activity followed Anderson's original ideas, the discovery of high-temperature superconductivity by Bednorz and Müller in 1986 [Bednorz86] revived the interest in the RVB model. Anderson suggested that the RVB state of a Mott insulator, rather than the conventional metallic Fermi-liquid state, is the appropriate reference state for the description of the new high-T_c cuprate superconductors, particularly addressing those based on La_2CuO_4 [Anderson87a]. He departed from the traditional BCS approach that was not able to explain the high transition temperatures by identifying a predominantly electronic and magnetic mechanism as the origin of superconductivity, instead of an exchange of virtual phonons. In his view, the preexisting magnetic singlet pairs take over the role of the conventional Cooper pairs when they become charged upon sufficiently strong doping of the initial insulator. Today it is widely believed that RVB ideas are not applicable to the cuprate superconductors. Nevertheless it is an interesting route to superconductivity, as the physics takes place on the energy scale of the magnetic exchange constant J, which is of the order of $700\,\mathrm{K}$ for the compound in the focus of this thesis, TiOCl.

Basic Properties of the RVB State

In the previous section it was shown that for a single pair of interacting spins the ground state is a singlet or, in Anderson's nomenclature, a valence bond, which may be written as

$$b_{ij}^\dagger = \tfrac{1}{\sqrt{2}}\left(c_{i\uparrow}^\dagger c_{j\downarrow}^\dagger - c_{i\downarrow}^\dagger c_{i\uparrow}^\dagger\right).\tag{2.51}$$

It is clear that in a two-dimensional $S = 1/2$ lattice every pair of interacting magnetic moments would like to form a spin singlet. However, this cannot be achieved for all possible pairs simultaneously, because a given magnetic moment can only form a singlet with one partner at a time. Note also that any complete covering of the lattice with singlets is not an eigenstate of the Heisenberg Hamiltonian, as will be illustrated later in a simple example. As a solution to this problem, Anderson suggested to delocalize the singlets among all pairs of electrons. In this way, every spin can be satisfied in a singlet state, and moreover, the system can gain a resonance energy because the Heisenberg Hamiltonian transforms related singlet configurations into one another, as will become clear in the example below. Such a state of singlets is created by the operator $\sum_{\langle ij\rangle} a_{ij} b_{ij}^\dagger$. Here only nearest neighbor interactions are considered, which will lead to a so-called short-range RVB state. Of course, it is possible to include also the interaction between more distant spins.
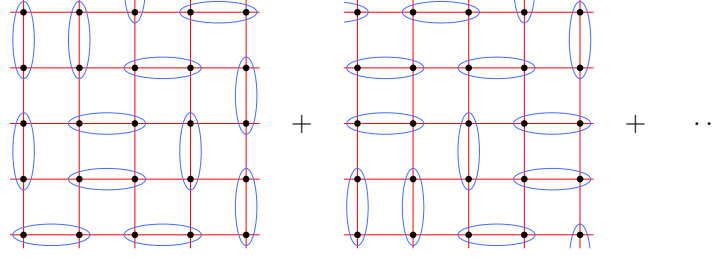
Figure 2.11: *Schematic illustration of the short-range RVB ground state. Valence bonds, i.e., singlet pairs, between neighboring magnetic moments are formed, and the RVB ground state is expressed as the superposition of all configurations of the kind depicted in the figure.*

The N electrons can Bose condense into a state Ψ with $N/2$ valence bonds

$$\Psi = \Big(\sum_{\langle ij \rangle} a_{ij} b_{ij}^{\dagger} \Big)^{N/2} |0\rangle , \qquad (2.52)$$

where $|0\rangle$ is the vacuum state. Unfortunately, Ψ contains large numbers of empty and doubly occupied sites, the latter costing the energy U, and is therefore not a good description for Mott insulators. In order to remedy this situation a projection technique can be applied. The Gutzwiller operator

$$P_{\mathrm{G}} = \prod_{i}(1 - n_{i\uparrow} n_{i\downarrow}) \qquad (2.53)$$

projects out every state with double occupancy. The RVB state can now be expressed as

$$\Psi_{\mathrm{RVB}} = P_{\mathrm{G}} \Big(\sum_{\langle ij \rangle} a_{ij} b_{ij}^{\dagger} \Big)^{N/2} |0\rangle . \qquad (2.54)$$

This form is a mathematical exact description of the short-range RVB state. However, it is not very convenient to handle for two reasons: Firstly due to the Gutzwiller projection, and secondly, because two different valence bond configurations are not necessarily orthogonal. The valence bond basis is thus overcomplete and non-orthogonal.

An illustration of the RVB state, which is nothing but the superposition of all possible singlet configurations that do not lead to doubly occupied sites, is given in Fig. 2.11. It is a precise magnetic singlet, the analogue of the Bethe solution for a linear AFM chain. An enormous degeneracy characterizes the RVB state, as the number of possible valence bond coverings increases exponentially with the number of lattice sites. The ground state can be viewed as a quantum *liquid* of valence bonds, whereas in this context the spin-Peierls state could be termed a *crystal* of valence bonds, which cannot resonate with other configurations without breaking bonds. It shall be stressed at this point that the suggestive phrase "valence bond" does not have a meaning in the chemical sense in this context. It is rather a pictorial representation of the magnetic singlets that can in principle form even between distant lattice sites.

It is remarkable that if the limitation to nearest-neighbor exchange in Equation 2.54 is lifted, the RVB state is capable of describing the Luttinger liquid or even long-range Néel order, depending on the choice of the coefficients a_{ij} [Baskaran93].

The above mentioned properties of the RVB state, e.g., the non-orthogonality of the valence bond configurations or the lowering of the free energy via resonance between those configurations, can be best understood by considering a simple example. Often the six interacting spins of a benzene ring are utilized, as it was this molecule that inspired Anderson to his pioneering work. In this thesis, however, the even simpler example of four spins arranged in a square are chosen. The sites are labelled with arabic numbers, as shown in Fig. 2.12 (a). For this situation one can write

$$
\begin{aligned}
\Psi_{\mathrm{RVB}} &= P_{\mathrm{G}} \Big(\sum\nolimits_{\langle ij \rangle} a_{ij} b_{ij}^{\dagger} \Big)^2 |0\rangle \\
&= P_{\mathrm{G}} \Big(a_{12} b_{12}^{\dagger} + a_{23} b_{23}^{\dagger} + a_{34} b_{34}^{\dagger} + a_{41} b_{41}^{\dagger} \Big)^2 |0\rangle \, .
\end{aligned}
\tag{2.55}
$$

Equal amplitudes a_{ij} for each singlet, i.e., the same interaction strengths, shall be assumed. The Gutzwiller operator now eliminates all configurations that involve double occupancy, and the RVB state becomes

$$
\begin{aligned}
\Psi_{\mathrm{RVB}} &= \tfrac{1}{\sqrt{3}} \Big(b_{12}^{\dagger} b_{34}^{\dagger} + b_{23}^{\dagger} b_{41}^{\dagger} \Big) |0\rangle \\
&= \tfrac{1}{2\sqrt{3}} \Big(2 \, |\uparrow\downarrow\uparrow\downarrow\rangle + 2 \, |\downarrow\uparrow\downarrow\uparrow\rangle - |\uparrow\downarrow\downarrow\uparrow\rangle - |\downarrow\uparrow\uparrow\downarrow\rangle - |\uparrow\uparrow\downarrow\downarrow\rangle - |\downarrow\downarrow\uparrow\uparrow\rangle \Big) \, .
\end{aligned}
\tag{2.56}
$$

The prefactor $\tfrac{1}{\sqrt{3}}$ ensures the normalization to unity. From this form, it can be seen that Equation 2.54 indeed leads to a state comprised of all possible bond configurations allowed by the Gutzwiller projection. In this simple case there exist only two — the one with horizontally and the one with vertically aligned bonds depicted in Fig. 2.12 (b) and (c), respectively. They are not orthogonal, as their scalar product does not vanish:

$$
\langle 0| \, b_{12} b_{34} \, b_{23}^{\dagger} b_{41}^{\dagger} \, |0\rangle = \tfrac{1}{4} \Big(\langle\uparrow\downarrow\uparrow\downarrow| - \langle\uparrow\downarrow\downarrow\uparrow| - \langle\downarrow\uparrow\uparrow\downarrow| + \langle\downarrow\uparrow\downarrow\uparrow| \Big)
$$
$$
\Big(|\downarrow\uparrow\downarrow\uparrow\rangle - |\uparrow\uparrow\downarrow\downarrow\rangle - |\downarrow\downarrow\uparrow\uparrow\rangle + |\uparrow\downarrow\uparrow\downarrow\rangle \Big) = \tfrac{1}{2} \quad (2.57)
$$

This is the reason for the unusual value $\tfrac{1}{\sqrt{3}}$ of the normalization factor.

Now a second observation follows that is more easily seen in this example than in the general case of a 2D lattice: A single valence bond configuration is not an eigenstate of the Heisenberg Hamiltonian, which reads in this case

$$
\mathcal{H}_4 = J \left(\mathbf{S}_1 \cdot \mathbf{S}_2 + \mathbf{S}_2 \cdot \mathbf{S}_3 + \mathbf{S}_3 \cdot \mathbf{S}_4 + \mathbf{S}_4 \cdot \mathbf{S}_1 \right) .
\tag{2.58}
$$

A single configuration is an eigenstate only of the scalar product of two spin operators

$$b_{12}^\dagger b_{34}^\dagger \ket{0} \qquad b_{13}^\dagger b_{24}^\dagger \ket{0} \qquad \Psi_{\mathrm{RVB}} = \tfrac{1}{\sqrt{3}}(b_{12}^\dagger b_{34}^\dagger + b_{13}^\dagger b_{24}^\dagger)\ket{0}$$
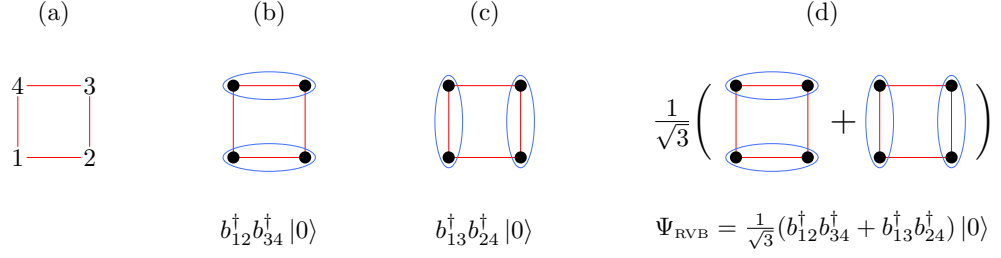
Figure 2.12: *Valence bond configurations of the four-site problem. (a) Labelling of the sites. (b) Configuration with horizontal bonds. (c) Configuration with vertical bonds. (d) RVB state as the superposition of all possible configurations.*

of electrons *within* the same singlet, as for example

$$
\begin{aligned}
\mathbf{S}_1 \cdot \mathbf{S}_2 \, b_{12}^\dagger b_{34}^\dagger \ket{0} &= \left(S_1^z S_2^z + \tfrac{1}{2} S_1^+ S_2^- + \tfrac{1}{2} S_1^- S_2^+ \right) \tfrac{1}{2} \Big(\ket{\uparrow\downarrow\uparrow\downarrow} - \ket{\uparrow\downarrow\downarrow\uparrow} - \ket{\downarrow\uparrow\uparrow\downarrow} + \ket{\downarrow\uparrow\downarrow\uparrow} \Big) \\
&= -\tfrac{1}{8} \Big(\ket{\uparrow\downarrow\uparrow\downarrow} - \ket{\uparrow\downarrow\downarrow\uparrow} - \ket{\downarrow\uparrow\uparrow\downarrow} + \ket{\downarrow\uparrow\downarrow\uparrow} \Big) \\
&\quad + \tfrac{1}{4} \Big(- \ket{\uparrow\downarrow\uparrow\downarrow} + \ket{\uparrow\downarrow\downarrow\uparrow} \Big) + \tfrac{1}{4} \Big(\ket{\downarrow\uparrow\uparrow\downarrow} - \ket{\downarrow\uparrow\downarrow\uparrow} \Big) \\
&= -\tfrac{3}{4} \, b_{12}^\dagger b_{34}^\dagger \ket{0} \, .
\end{aligned}
\tag{2.59}
$$

The situation is different if a scalar product is chosen that does not fulfill the above condition. Letting act $\mathbf{S}_2 \cdot \mathbf{S}_3$ on the same state yields

$$
\mathbf{S}_2 \cdot \mathbf{S}_3 \, b_{12}^\dagger b_{34}^\dagger \ket{0} = -\tfrac{1}{4} \, b_{23}^\dagger b_{41}^\dagger \ket{0} - \tfrac{1}{4} \, b_{13}^\dagger b_{24}^\dagger \ket{0} \, .
\tag{2.60}
$$

Hence, the considered state is not an eigenstate of $\mathbf{S}_2 \cdot \mathbf{S}_3$, and neither is it an eigenstate of the complete Heisenberg Hamiltonian. The second term of the result 2.60 is not of further relevance, as the singlet bond connects sites that are not nearest neighbors and do not interact. The first term, however, is the origin of the resonance energy in the RVB ground state as it couples the state depicted in Panel (b) with the state of Panel (c). From this result it can be learnt that parts of the Heisenberg Hamiltonian make the system "resonate" between different singlet configurations, i.e., a certain singlet bond configuration is transformed into another. As the RVB state consists not only of one configuration, but is a linear combination of all combinations allowed by the Gutzwiller projection, it is able to take advantage of this resonance. Summing up all contributions of the above type leads to the ground state energy

$$
\begin{aligned}
E_0 &= \bra{\Psi_{\mathrm{RVB}}} \mathcal{H}_4 \ket{\Psi_{\mathrm{RVB}}} \\
&= \frac{J}{3} \bra{0} (b_{12} b_{34} + b_{23} b_{41}) (\mathbf{S}_1 \cdot \mathbf{S}_2 + \mathbf{S}_2 \cdot \mathbf{S}_3 + \mathbf{S}_3 \cdot \mathbf{S}_4 + \mathbf{S}_4 \cdot \mathbf{S}_1) (b_{12}^\dagger b_{34}^\dagger + b_{23}^\dagger b_{41}^\dagger) \ket{0} \\
&= \left(-\tfrac{3}{4} - \tfrac{3}{4} - \tfrac{1}{4} - \tfrac{1}{4} \right) J = -2J \, .
\end{aligned}
\tag{2.61}
$$

On the other hand, the energy of a single configuration is

$$\langle 0| \, b_{12} b_{34} \, \mathcal{H}_4 \, b_{12}^\dagger b_{34}^\dagger \, |0\rangle = (-\tfrac{3}{4} - \tfrac{3}{4})J = -1.5J, \tag{2.62}$$

i.e., simply twice the energy E_{singlet} of one singlet derived in Equation 2.33. The RVB ground state is thus lower in energy than the crystalline arrangement of valence bonds. This is the essence of the RVB state.

Another property of this state is the absence of antiferromagnetic order in the Néel sense, which expresses itself in the fact that $\langle \Psi_{\text{RVB}}| \, S_i^z \, |\Psi_{\text{RVB}}\rangle = 0$ for every site i. However, it is easy to see that the magnetic correlations between interacting sites do not vanish, so $\langle \Psi_{\text{RVB}}| \, S_i^z S_{i+1}^z \, |\Psi_{\text{RVB}}\rangle = -\tfrac{1}{6}$.

The RVB State — A Fragile State of Matter

After this simple example, that nicely illustrated the basic properties of the RVB state, the question will be answered if this state is likely to occur at all. Up to date no experiment was able to show that the RVB state is realized in nature. From the theoretical side, it was proven that the ground state of the antiferromagnetic $S = 1/2$ Heisenberg model for a three-dimensional cubic lattice shows AFM order. Even for the two-dimensional square lattice the AFM order is universally accepted [Fazekas99b]. Moreover, if a finite coupling to the phonons is allowed for, the most straightforward possibility to break the symmetry of an antiferromagnet would rather be the spin-Peierls state. It is therefore likely that a Heisenberg system will undergo a phase transition with broken spin rotational or translational symmetry (or both) before the RVB state can develop. Presumably, it can only then prevail when all more obvious types of ordered states are frustrated. So, what are then the conditions for the establishment of the RVB state?

One loophole poses the *geometric frustration* of a system. The emergence of magnetic order relies heavily on the fact that the ground state of the Ising term is essentially unambiguous. This is ensured when dealing with a bipartite lattice, e.g., the square lattice with nearest-neighbor coupling only. In this situation, an up-down alternation of the spins is possible without complications. However, if such a configuration is geometrically frustrated as illustrated in Fig. 2.13, the RVB state gets a chance to develop. Exactly for this reason Anderson considered the triangular lattice in his original publication [Anderson73]. Another candidate is the square lattice, if either or both of the two possibilities occur: A next-nearest-neighbor interaction strong enough to frustrate the Néel state, or a coupling to the phonon system short of being strong enough to induce the spin-Peierls instability [Anderson87a].

Other necessary conditions for the applicability of the RVB theory are *low spin* and *low dimensionality*, because in this regime the effects of quantum fluctuations are more dramatic. This can be demonstrated comparing the energy of a singlet-pair state and of a Néel state as a function of dimensionality and spin. For a D-dimensional cubic lattice with N sites of spin S, the DN nearest neighbor pairs contribute to the Néel state's
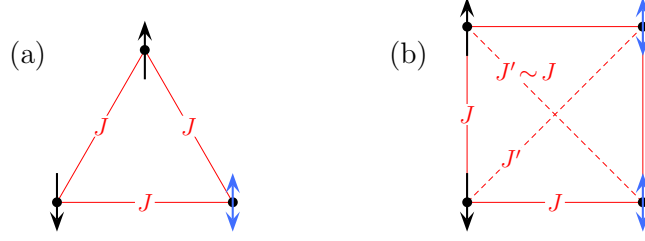
Figure 2.13: *Illustration of geometric frustration. (a) In this triangular system, the two spins drawn in black are able to minimize their magnetic energy, whereas this is not possible for the remaining spin drawn in blue. It is exposed to the conflicting interactions of both its neighbors. (b) The situation is similar for the over-determined system of four spins arranged in a square with nearest-neighbor and next-nearest-neighbor coupling. Without the diagonal interaction the system would be unfrustrated, for every spin could reside in a state unambiguously determined by the condition of minimizing the total energy. Switching on the diagonal coupling leads again to competing interactions and the system becomes frustrated.*

energy

$$E_{\text{Néel}} = -DNS^2 J. \qquad (2.63)$$

The singlet state profits independently of the dimensionality from $N/2$ pairs, and its energy thus is given by

$$E_{\text{singlet}} = -\tfrac{1}{2}NS(S+1)J. \qquad (2.64)$$

Obviously, in high dimensions and for high spin the Néel state is preferred, while the singlet state takes advantage of the opposite limit. Note, however, that this argument not only applies to the RVB but also to the spin-Peierls state, which benefits from the formation of singlet bonds as well.

Even though the high-temperature superconductors are strongly anisotropic $S = 1/2$ systems, it seems unlikely that the superconductivity in the cuprates can be explained by the RVB model for the following reasons: The superconductivity in these systems is an amazingly robust phenomenon, in contrast to the fragile RVB state, and furthermore, types of magnetic order seem to persist in the doped cuprates even into the superconducting state, which is not compatible with the RVB model [Carlson04].

t-J Model and Spin-Charge Separation

Up to this point the discussion was limited to the special case of a half-filled band. The question naturally arises what happens when this restriction is lifted, i.e., carriers such as holes are introduced into the Mott insulator. This situation can be described by the so-called t-J model, which can be derived from the Hubbard Hamiltonian 2.3 in the large U limit by an appropriate canonical transformation [Fulde91]. The t-J Hamiltonian can be written as

$$\mathcal{H}_{tJ} = t \sum_{\langle ij \rangle \sigma} \left((1-n_{i,-\sigma})c_{i\sigma}^\dagger c_{j\sigma}(1-n_{j,-\sigma}) + \text{h.c.} \right) + J \sum_{\langle ij \rangle} \mathbf{S}_i \cdot \mathbf{S}_j, \qquad (2.65)$$
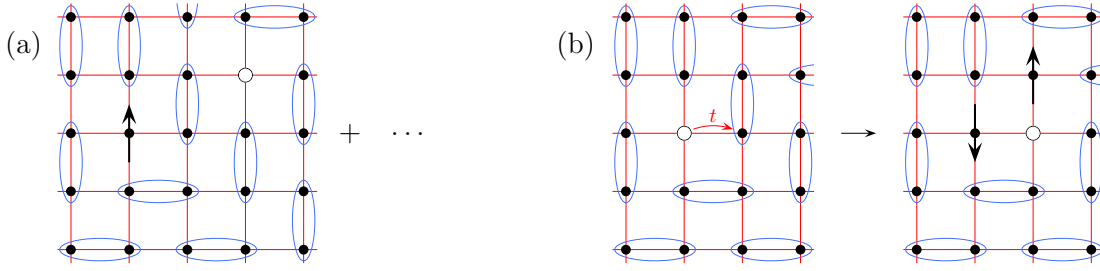
**Figure 2.14:** *(a) Schematic picture of a spinon and a holon excitation in the RVB model. Spinons carry a $S = 1/2$ magnetic moment and no charge, holons are charged excitations that carry no spin. (b) Diagram illustrating the frustration effect of a propagating hole. If a holon hops to the neighboring site, it inevitably destroys a singlet bond, and as a result two unpaired spins appear.*

with the projection operators $(1-n_{i,-\sigma})$ to exclude double occupancy. This projection is necessary since the hopping term could otherwise lead to a state outside the singly occupied subspace. From this Hamiltonian, the Heisenberg Hamiltonian follows trivially for half-filling. For a finite doping concentration x, the basic physics of this model can be viewed as the competition between the energy gain $\sim xt$ due to mobile holes, and the cost of the exchange energy $\sim J$ resulting from the disruption of the antiferromagnetic correlations [Manske04].

An important concept associated with the RVB model is the spin-charge separation. This phenomenon can be understood by examining the excitations that arise in the RVB picture. If a hole is inserted into the half-filled RVB state, one unpaired magnetic moment and one vacant site with charge $+e$ will appear, as shown in Fig. 2.14 (a). Anderson introduced the term "spinon" for the neutral spin-1/2 excitation, the charged spin-0 excitation is called "holon". The spinon and the holon are not bound to each other, and due to the liquid-like character of the RVB state they can propagate independently with the aid of the transfer energy t. In this way, spin and charge separate, and the liquid of valence bonds will fill the space between the two excitations as they drift apart.

The spin excitation with its magnetic moment of $S = 1/2$ is clearly a fermion. This is in contrast to the Néel state, where the excitations are bosonic magnons with spin-1 or spin-0 singlets. Concerning the holons, it is tempting to assign a bosonic character to these spinless excitations. Although this is correct for a number of regards, the matter is more complicated than this simple view. There is no universal answer to the question if the holon is a boson or a fermion. The statistics of this quasiparticle is dynamically determined, there are even transitions between states in which the holon has different statistics [Carlson04].

As can be seen from Fig. 2.14 (b), the motion of a holon is inevitably connected with the destruction of local singlet bonds. The mobile holes thus frustrate the tendency of the spins to order. The valence bond liquid is much better able to compensate this effect than the crystalline arrangement of the spin-Peierls state. Doping therefore stabilizes the RVB state.
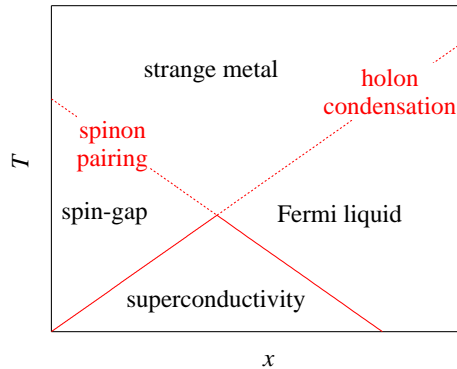
Figure 2.15: *Mean-field phase diagram of the RVB model obtained by a Ginzburg Landau theory [Nagaosa92]. Only the boundary to the superconducting region is found to correspond to a genuine phase transition, the remaining phase space can be regarded as a crossover from the spin-charge separated phase to the Fermi liquid.*

This fact is reflected in the phase diagram of the RVB model that was calculated by a phenomenological Ginzburg-Landau theory with two order parameters, viz., for the spinon pairing and for the Bose condensation of the holons [Nagaosa92]. From this mean-field calculation the holon condensation temperature is found to increase with the hole concentration x. On the other hand, the spinon pairing temperature is a decreasing function of x and reaches zero when $x \sim J/t$. The two scales associated with carrier coherence and singlet pairing give rise to the lines drawn in Fig. 2.15, where the resulting phase diagram with four different regions is displayed. In the region where both the spinons are paired and the holon system has condensed, a superconducting phase is predicted. Note the obvious resemblance to the phase diagram of the high-T_c superconductors with the superconducting "dome" and the pseudogapped phase (cf. Ref. [Carlson04] for a review).

Superconductivity

At first sight it seems to be very surprising that the RVB state of a Mott insulator is able to produce a superconducting phase, since conventional superconductivity emerges from a Fermi liquid reference state. At closer inspection, however, one sees that the RVB state is full of singlet electron pairs, just as the familiar Cooper pairs of a BCS superconductor. Even if these singlet pairs are not able to carry a current at half-filling, where any form of charge transport is connected with a great energy cost, one cannot disapprove the idea that the valence bonds are preexisting, yet uncharged Cooper pairs [Müller-Hartmann88].

The mean-field theory developed by Baskaran, Zou, and Anderson (BZA) is able to show how superconductivity can arise from the RVB model [Baskaran87]. In the BZA theory the exchange term $J \sum_{\langle ij \rangle} \mathbf{S}_i \cdot \mathbf{S}_j$ in Equation 2.65 plays the role of the interaction term of the conventional BCS theory. The formal similarity is appreciated when going

back to the form 2.30, where the exchange term was written in terms of four fermion operators. BZA treated the interaction with a Hartree-Fock approximation. The four fermion operators are reduced to two by introducing the order parameter

$$\Delta = \sqrt{2}\langle b_{ij}^\dagger \rangle = \langle c_{i\uparrow}^\dagger c_{j\downarrow}^\dagger - c_{i\downarrow}^\dagger c_{i\uparrow}^\dagger \rangle. \tag{2.66}$$

This Hamiltonian can be diagonalized à la BCS by a Bogoliubov transformation. Before discussing the general solution of the resulting gap equation, the trivial solution will be examined, which corresponds to the half-filled case without doping. It leads to the RVB state 2.54 constructed originally by Anderson. Furthermore, one obtains that the low energy excitations are the above introduced spinons. In contrast to the charged excitations, the spinon excitation spectrum is gapless — spinons possess a pseudo Fermi surface where the excitation energy vanishes. As a consequence, a linear temperature dependence of the specific heat $C(T) \propto \gamma T$ is expected, analog to the heat capacity of a normal metal. In the presence of a magnetic field, the degeneracy of spinon states will be lifted giving rise to a Pauli susceptibility.

The RVB state, obtained in this way from first principles, has a strong analogy to the BCS ground state, which is usually written as

$$\Psi_{\mathrm{BCS}} = \prod_{\mathbf{k}} \left(u_{\mathbf{k}} + v_{\mathbf{k}} c_{\mathbf{k}\uparrow}^\dagger c_{-\mathbf{k}\downarrow}^\dagger \right) |0\rangle. \tag{2.67}$$

It is an easy task to show (cf. Ref. [Anderson87a]) that the projection of Ψ_{BCS} to the state with $N/2$ cooper pairs reads

$$\Psi_{\mathrm{BCS}} = \left(\sum_{ij} g_{i,j} c_{i\uparrow}^\dagger c_{j\downarrow}^\dagger \right)^{N/2} |0\rangle, \tag{2.68}$$

where $g_{i,j}$ is the Cooper pair wave function. Comparing this to the RVB state given by Equation 2.54 yields that the main difference is the removal of double occupancy imposed by the Gutzwiller projection.

Turning now back to the general solution of the gap equation, a superconducting state with a true energy gap is produced when the system is doped. While the motion of singlet pairs is not accompanied by any charge flow at half-filling, a valence bond can carry charge if it is next to a hole. In other words, the motion of holes can be thought of as a motion of charge carrying singlet bonds. The previously uncharged Cooper pairs become thus charged.

From this mean-field point of view, the system will become a superconductor as soon as it is metallized, since the pairing exists already in the insulating state. Breaking a singlet costs an energy of the order of J, which determines the spin gap. The pairing is a property of the spin degree of freedom, and involves little or no pairing of actual charge. In the superconducting state, the system can be viewed as being in a quantum protectorate, which means that the many-body correlations are so strong that the dynamics

Table 2.2: *Comparison between conventional BCS theory and RVB theory.*

Theory	Reference State	Mechanism	Excitations
BCS	Fermi liquid	Exchange of Bose quanta	Bogoliubov quasiparticles
RVB	Mott insulator, quantum spin liquid	Exchange interaction	spinons

can no longer be described in terms of individual particles. Perturbations which scatter individual particles are consequently not effective, and the system is superconducting.

In Table 2.2 the features of the BCS theory are compared to the RVB theory, which is able to generate superconductivity as well. The most novel aspect is probably the parting of ways from the traditional approach of building pair condensation in a Fermi liquid reference state [Baskaran01].

When the system is doped too much, electron pairs will break up by gaining kinetic energy, and superconductivity will disappear. The optimum doping concentration is expected to be of order of t/U, as then the kinetic energy and pair binding energies match. The corresponding transition temperature will be of the order or less than J [Anderson87a], which can be much higher than the typical transition temperature of a conventional BCS superconductor.

3 Photoemission Spectroscopy

The experimental examination of low-dimensional transition metal compounds systems is the main subject of this thesis, but, of course, only the joint efforts of experiment *and* theory can lead to a deeper understanding of the involved phenomena. In this regard photoemission spectroscopy must be appreciated as an extremely useful tool, since the momentum-dependent spectral function $A(E, \mathbf{k})$ — a key property of many-body electron systems — can be accessed very directly by this technique. Hence, a comparison to the results of theoretical methods is straightforwardly possible. It is a fortunate circumstance that the necessary condition for the emergence of RVB, Mott, or Peierls physics, viz., *low dimensionality*, constitutes a perfect ground for the photoemission experiment. It will become clear in the course of this chapter that both the experimental procedure and the interpretation of the results strongly benefit from the low-dimensional character. In the following an introduction to the experimental technique of photoelectron spectroscopy will be given, focussed on those aspects with direct relevance for the discussion of the experimental results.

In an angle-resolved photoemission (ARPES) experiment, a single crystal is exposed to a beam of monochromatized radiation, produced for instance by a gas-discharge lamp or by a synchrotron radiation source with typical photon energies in the range from 10 to 100 eV. Electrons will then be emitted by the photoelectric effect and escape into the vacuum in all directions. By collecting photoelectrons with an electron energy analyzer characterized by a finite acceptance angle, both their kinetic energy and their emission angle are recorded, as sketched in Fig. 3.1 (a). The wave vector of the photoelectron *in vacuo* is thus completely determined. Both its components parallel and perpendicular to the surface are easily expressed in terms of the polar emission angle ϑ:

$$\hbar k_\parallel^{\text{vac}} = \sqrt{2mE_{\text{kin}}} \sin \vartheta \tag{3.1}$$

$$\hbar k_\perp^{\text{vac}} = \sqrt{2mE_{\text{kin}}} \cos \vartheta \tag{3.2}$$

It is then the aim to deduce from this information the energy and momentum distribution *in the solid* by exploiting the corresponding conservation laws. In order to account for the many-body effects discussed in the previous chapter, one has to choose also a suitable many-body description of the photoemission process. But before this approach will be presented, the general properties of the photoemission experiment shall be addressed within the independent electron picture, as it offers an intuitive understanding of the photoemission process.
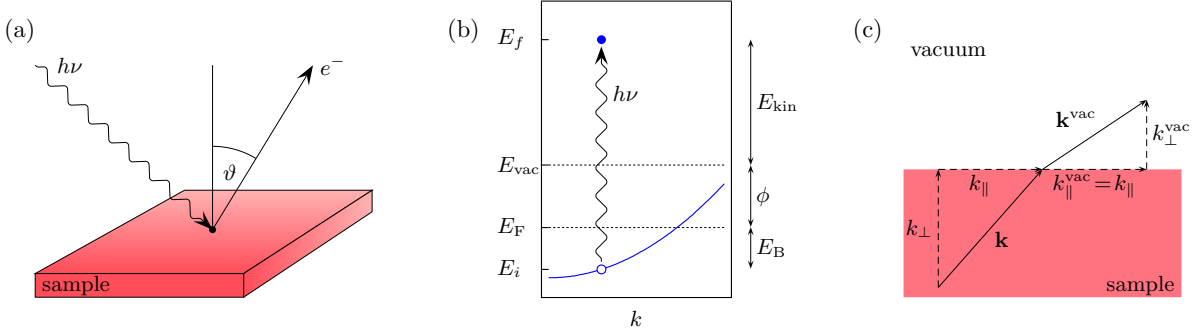
Figure 3.1: *(a) Schematic illustration of a photoemission experiment. (b) Energetics of the photo-emission process. (c) Refraction of the photoelectron at the escape into vacuum.*

One-Particle Picture

In the one-particle picture, the binding energy of the electron before the excitation is derived by a simple argument of energy conservation according to the energy scheme displayed in Fig. 3.1 (b) as

$$E_\text{B} = h\nu - \phi - E_\text{kin}, \tag{3.3}$$

where E_B is the binding energy, $h\nu$ the photon energy, and ϕ the work function. In order to obtain the electronic momentum in the solid, it is essential to recall that according to band theory, the electrons in a crystal can be described by Bloch waves of the form $\Psi(\mathbf{k}, \mathbf{r}) = u_n(\mathbf{r}) \exp(i\mathbf{k} \cdot \mathbf{r})$, where u_n is a function obeying the lattice periodicity. The Bloch theorem still holds outside the solid if restricted to the dimensions parallel to the sample surface. In this case the condition of translational invariance with the lattice periodicity is trivially satisfied. Therefore, the wave vector components parallel to the surface are conserved:

$$\hbar k_\| = \hbar k_\|^\text{vac} = \sqrt{2mE_\text{kin}} \sin \vartheta \tag{3.4}$$

Note, however, that in this equation the photon wave vector was neglected, as is common practice in the analysis of ARPES experiments. This is well justified for ultraviolet radiation — for example, the momentum of a He I photon is only $\sim 1\%$ of an electron momentum at the Brillouin zone edge in TiOCl or TaSe$_2$.

The case of the perpendicular momentum $k_\perp$ is more complicated, since the translational invariance fails to hold in this dimension, and therefore the photoelectron is refracted when leaving the crystal, as illustrated in Fig. 3.1 (c). In general it is a complex task to determine $k_\perp$, which requires additional information about the final states, but for a crude estimate it is possible to make the *a priori* assumption of nearly-free electrons. Adopting this description for the final bulk Bloch states, one obtains

$$\hbar k_\perp = \sqrt{2m \left(E_\text{kin} \cos^2 \vartheta + V_0 \right)}, \tag{3.5}$$

where V_0 is the inner potential corresponding to the energy of the bottom of the valence band referenced to the vacuum level E_vac. Note that this method is expected to work well

for high-energy final states in which case the crystal potential is a small perturbation. Eventually the bands become so closely spaced in energy to form a continuum, and the details of the final-state band structure become unimportant [Damascelli04].

Not only is it difficult to determine the perpendicular momentum due to the refraction at the potential step from the solid into the vacuum, also the damping of the final state perpendicular to the surface poses a problem. At the typical kinetic energies of an ARPES experiment the threshold of plasmon excitation is exceeded, leading to a high cross section for electron-plasmon scattering. Also interband transitions are likely to scatter the photoelectrons inelastically, so that an extremely low mean free path of the order of 5–15 Å results. This is the reason for the strong surface sensitivity of the photoemission technique. Furthermore, the damping of the perpendicular momentum relaxes the selection rule for $k_\perp$, so that the information on the electronic structure becomes smeared out in this direction [Strocov03].

Fortunately, the drawbacks caused by the lack of control of $k_\perp$ become irrelevant for strongly anisotropic systems, where the dispersion of the electronic structure is only weakly pronounced in the direction perpendicular to the surface. The layered materials investigated in this thesis are thus ideally suited for photoemission experiments. In fact, TaSe$_2$ was the first material for which it was demonstrated that the electronic structure can be mapped by angle resolved photoemission [Smith74]. It is added that not only does the interpretation of the experimental spectra benefit from the strongly anisotropic electronic structure. In addition, layered compounds offer the possibility to prepare *in situ* clean surfaces due to the presence of natural cleavage planes.

For non-interacting electrons, the probability to detect a photoelectron with momentum $\mathbf{k}_f$ and energy E_f can be expressed according to Fermi's Golden Rule as

$$I(\mathbf{k}_f, E_f) \propto \sum_{\mathbf{k}_i} |M_{fi}|^2 \delta(E_f - E_i - h\nu) \,, \tag{3.6}$$

where $M_{if} = \langle \mathbf{k}_i | \mathcal{H}_{\text{int}} | \mathbf{k}_f \rangle$ is the one-particle matrix element of the optical transition. Note that the summation involves only the initial states, as the final state is already determined by the experiment itself (E_f and the measured E_{kin} are easily translated with help of the energy diagram of Fig. 3.1). The operator $\mathcal{H}_{\text{int}}$ describes the interaction of the electrons with an oscillating electromagnetic wave field $\mathbf{A}(\mathbf{r}, t)$. Replacing the momentum operator $\mathbf{p}$ by $\mathbf{p} + \mathbf{A}$ and neglecting terms of quadratic order in $\mathbf{A}$ leads to the form

$$\mathcal{H}_{\text{int}} = \frac{e}{2mc}(\mathbf{A} \cdot \mathbf{p} + \mathbf{p} \cdot \mathbf{A}). \tag{3.7}$$

To give an illustrative meaning to the result 3.6, it is pointed out that under the assumption of a constant matrix element, it is possibly to deduce the band structure $E(\mathbf{k})$ in the solid directly from the measured energy and momentum distribution of the photoemission signal. An integration in $\mathbf{k}$-space consequently yields the density of states in this one-particle description.

Many-Body Picture

In order to incorporate electronic correlations, which are an essential ingredient in the physics of the investigated materials, it is necessary to work with N-electron wave functions and energies, instead of the corresponding one-particle quantities. Only then it is possible to take account of the reaction of the $N-1$ particle system that is induced by the removal of the photoelectron. Analogous to the one-particle description, it is possible to apply time-dependent perturbation theory, but now Fermi's Golden Rule has to be formulated in the N-particle Hilbert space (for a review, see Refs. [Kevan92,Hüfner95,Claessen97,Hüfner99,Schattke03,Damascelli04]). For simplicity, it shall be assumed that $T = 0$, i.e., before the excitation the system is in its ground state $|N\rangle$ with energy $E(N, 0)$. The final state relevant for photoemission must obviously contain one free electron with wave vector $\mathbf{k}_f$ and energy E_f. The remaining $N-1$ electrons will be left behind in an excited state labelled by the quantum number s with energy $E(N-1, s)$. The final state is thus written as $|\mathbf{k}_f; N-1, s\rangle$. With this nomenclature, the photoemission intensity reads

$$I(\mathbf{k}_f, E_f) \propto \sum_s |\langle \mathbf{k}_f; N-1, s| \, \mathcal{H}_{\text{int}} \, |N\rangle|^2 \; \delta(E_f - E_s - h\nu), \qquad (3.8)$$

where $E_s = E(N, 0) - E(N-1, s)$ is the energy of the excited photohole state and the subscript f refers to the wave vector and energy of the photoelectron, both of which are measured in the experiment.

Starting from this expression, it will be derived in the following that the photoemission signal is closely related to the spectral function — a quantity which is directly accessible by many-body theory.

The matrix element can be simplified considerably with help of the *sudden approximation*. One then assumes that relaxation processes of the $N-1$ electron system do not have time to occur before the photoelectron leaves the solid. In other words, an electron is instantaneously removed, and the effective potential of the system changes discontinuously at that instance without any interaction between the photoelectron and the system left behind. At sufficiently high energies, this approximation is certainly justified, but for He I radiation or even lower photon energies it is advisable to apply this approximation with caution.

The essential step in simplifying the matrix element is the factorization of the final state. The state can then be written as a product of the photoelectron and the $N-1$ electron state:

$$|\mathbf{k}_f; N-1, s\rangle = c_f^\dagger \, |N-1, s\rangle \qquad (3.9)$$

Writing the interaction operator in second quantization

$$\mathcal{H}_{\text{int}} = \sum_{lm} \langle \mathbf{k}_l| \, \mathcal{H}_{\text{int}} \, |\mathbf{k}_m\rangle \, c_l^\dagger c_m = \sum_{lm} M_{lm} c_l^\dagger c_m, \qquad (3.10)$$

where M_{lm} is the one-particle matrix element, leads to the following form of Fermi's Golden Rule:

$$I(\mathbf{k}_f, E_f) \propto \sum_s \left| \langle N-1, s | c_f \sum_{lm} M_{lm} c_l^\dagger c_m | N \rangle \right|^2 \delta(E_f - E_s - h\nu) \qquad (3.11)$$

If the photoelectron is fast enough, there are no virtual states f in the ground state $|N\rangle$ to annihilate. Consequently, c_f must match $c_l^\dagger$ and one can write

$$\begin{aligned}
I(\mathbf{k}_f, E_f) &\propto \sum_s \left| \sum_m M_{fm} \langle N-1, s | c_m | N \rangle \right|^2 \delta(E_f - E_s - h\nu) \\
&= \sum_{mn} M_{fm} M_{fn}^* \sum_s \langle N-1, s | c_m | N \rangle \langle N | c_n^\dagger | N-1, s \rangle \, \delta(E_f - E_s - h\nu) \quad (3.12) \\
&= \sum_{mn} M_{fm} M_{fn}^* \, A_{mn}(E_f - h\nu) \,,
\end{aligned}$$

where $A_{mn}(E)$ is a matrix generalization of the spectral function. In its simplest form, the sudden approximation assumes that this matrix is diagonal, i.e., $A_{mn}(E) = A^<(\mathbf{k}_n, E) \, \delta_{mn}$, with the spectral function defined as

$$A^<(\mathbf{k}_n, E) = \sum_s |\langle N-1, s | c_n | N \rangle|^2 \, \delta(E - E_s) \,. \qquad (3.13)$$

The photoemission signal can now be written as

$$I(\mathbf{k}_f, E_f) = \sum_n |M_{fn}|^2 \, A^< (\mathbf{k}_n, E_f - h\nu) \,. \qquad (3.14)$$

Assuming that the one-electron matrix element M_{fn} conserves momentum, this result can be interpreted in the sense that the spectral function is the theoretical counterpart of the photocurrent. This is a very natural result considering the definition of $A^<(\mathbf{k}_n, E)$ as describing the spectrum of excitation energies when a particle is removed from the system. This physical meaning is best understood when interpreting Equation 3.13 as instruction for a quantum-mechanical measurement [Claessen97]: The operator c_n first destroys an electron with Bloch wave vector $\mathbf{k}_n$ in the ground state $|N\rangle$. The resulting hole state will in general *not* be an eigenstate of the $N-1$ particle system. In the measurement it is projected onto the excited states $|N-1, s\rangle$, and only if the energy of interest E matches the excitation energy $E_s = E(N, 0) - E(N-1, s)$, the matrix element can contribute to the result. The spectral function is thus the many-body generalization of the $\mathbf{k}$-resolved density of states. For non-interacting electrons, the hole state $c_n |N\rangle$ will be identical to exactly one of the excited states $|N-1, s\rangle$, so that $A^<(\mathbf{k}_n, E)$ boils down to the δ-function. Along with that, Equation 3.13 transforms into its one-particle counterpart 3.6.

A great advantage of photoemission can definitely be seen in the close connection to the spectral function, which is in turn intimately related to its one-particle Green's function $G(\mathbf{k}, E)$. Extending the Green's function formalism to include the effect of finite temperatures, the spectral function is given as

$$A^<(\mathbf{k}, E) = \frac{1}{\pi} \operatorname{Im} G(\mathbf{k}, E - i0^+) \, f(E, T), \qquad (3.15)$$

where $f(E, T)$ is the Fermi function.

Even though it is very helpful to have the above described intuitive interpretation of the photoemission signal, it must not be forgotten that the applied approximations omit that the interaction with light is associated with a cross section — an aspect to which the remainder of this chapter is devoted.

The Matrix Element

It was shown that in an ARPES experiment information about the spectral function can be gained. However, several effects perturb a direct extraction of this quantity: The finite experimental resolution in determining energy and momentum of the photoelectron, and also the background of secondary electrons, which escape from the solid after having lost parts of their kinetic energy in inelastic scattering events. Last but not least, the matrix element stands in the way of identifying the photoemission signal directly with the desired spectral function. While it is often assumed that the matrix element is a slowly varying function of energy and momentum, so that its effect can be neglected, a special case will be presented in the following, where this assumption fails utterly: For certain geometric measurement conditions, the matrix element for the emission from particular initial states can vanish identically.

The matrix element is usually simplified by means of the so-called *dipole approximation*, which assumes that the commutator $[\mathbf{p}, \mathbf{A}] = i\hbar \nabla \mathbf{A}$ vanishes. This is justified when the spatial variation of the light field is small on the atomic scale. The interaction operator introduced in Equation 3.7 then reduces to

$$\mathcal{H}_{\text{int}} = \frac{e}{mc} \mathbf{A} \cdot \mathbf{p}. \qquad (3.16)$$

The momentum operator can be rewritten as commutator of the unperturbed Hamiltonian $\mathcal{H}_0$ and the position operator $\mathbf{r}$, so that the matrix element can be expressed as

$$M_{if} = \frac{e}{mc} \langle \mathbf{k}_f | \mathbf{A} \cdot \mathbf{p} | \mathbf{k}_i \rangle = -\frac{ie}{\hbar c} A_0 \, (E_f - E_i) \, \langle \mathbf{k}_f | \varepsilon \cdot \mathbf{r} | \mathbf{k}_i \rangle, \qquad (3.17)$$

where ε is a unit vector along the polarization direction of the vector potential $\mathbf{A}$, whose amplitude is A_0.

In the following the experiment sketched in Fig. 3.2 shall be considered. The geometry is such that the wave vector of both the incoming photon and the escaping photoelectron
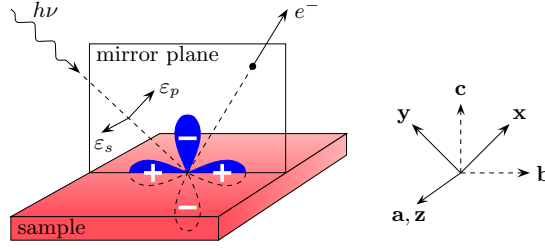
Figure 3.2: *Geometry of an experiment with mirror plane emission from an even-symmetry orbital. The light polarization ε_p is parallel to the mirror plane, whereas ε_s is perpendicular. With the coordinate system on the right, chosen in accordance with the compound TiOCl (cf. Chapter 5), the depicted orbital corresponds to d_{xy} symmetry.*

are located within the same mirror plane of the sample. If a real-space basis is chosen for the states $|\mathbf{k}_f\rangle$ and $|\mathbf{k}_i\rangle$, it becomes obvious that the integrand of the matrix element $\phi_f^{\mathbf{k}}(\mathbf{r})\varepsilon\cdot\mathbf{r}\phi_i^{\mathbf{k}}(\mathbf{r})$ must be an even function under reflection with respect to the mirror plane, otherwise it would vanish. The parity of the three factors comprising the integrand will now be examined separately. The final state $\phi_f^{\mathbf{k}}(\mathbf{r})$ must be even, as a wavefunction with odd symmetry would require that the mirror plane is a nodal plane. It could therefore not be detected in this experiment, where the detector is located in exactly this plane. The parity of the second factor $\varepsilon\cdot\mathbf{r}$ depends on the polarization of the incident radiation: If the polarization vector is parallel to the mirror plane, ε_p selects only the in-plane components of $\mathbf{r}$, and the scalar product is even. The opposite is true for the perpendicular polarization; then $\varepsilon_s\cdot\mathbf{r}$ is an odd function with respect to the mirror plane. The initial state can be of either parity, of course. Assume, for instance, a Bloch wave with wave vector $\mathbf{k}_i$ within the mirror plane, which is comprised exclusively of even orbitals. As an example a d_{xy} orbital of the compound TiOCl can be considered, which is oriented in space as shown in Fig. 3.2. This orbital possesses an even parity, and so does the Bloch wave, consequently. The separately discussed parities for emission from this initial state can be summarized as

$$\langle\mathbf{k}_f|\,\mathbf{A}\cdot\mathbf{p}\,|\mathbf{k}_i\rangle = \begin{cases} \langle+|+|+\rangle \neq 0 & \text{if } \varepsilon = \varepsilon_p, \\ \langle+|-|+\rangle = 0 & \text{if } \varepsilon = \varepsilon_s. \end{cases} \tag{3.18}$$

Hence, in this example photoemission is symmetry forbidden when the light polarization is perpendicular to the mirror plane. Exactly this effect will be utilized in a polarization-dependent photoemission study on TiOCl subject of Section 5.5.3, which shows that it is possible to determine the symmetry of the low-lying electronic states in this way.

4 Surface Metal-Insulator Transition in $1T$-TaSe$_2$

4.1 Motivation

In 1979 Fazekas and Tosatti revealed that the interplay of lattice, charge and spin degrees of freedom in $1T$-TaS$_2$ couples two phenomena which usually occur independently from each other: The charge density wave, which is based on electron-phonon interactions, and the Mott metal-insulator transition, which emerges from electronic correlations [Fazekas79]. Until today $1T$-TaS$_2$ and related transition metal dichalcogenides receive ongoing interest, not only because of the wealth of physics that evolves from this interplay, but also because they are perfectly suited to examine the electronic structure and its changes responsible for these phenomena. The quasi-two-dimensional structure makes them an ideal sample for angle-resolved photoelectron spectroscopy, both from the experimental point of view, and because the complications in interpreting the data are minimized due to the strongly anisotropic electronic structure.

The basic units of the CDW superstructure in $1T$-TaS$_2$ are so-called star-of-David clusters consisting of 13 Ta atoms. However, several distinct CDW phases are found, and only below 180 K these clusters are ordered in a triangular lattice. Above this temperature a nearly-commensurate, a domain-like incommensurate, and an incommensurate phase were found to exist [Bayliss84, Wu89]. At the 180 K phase transition the system not only changes between two different CDW states, this transition is additionally accompanied by a Mott metal-insulator transition. Due to the complex phase diagram, this system cannot be considered as an example for a canonical Mott-Hubbard transition.

It was discovered first by Perfetti *et al.* that the isostructural and isoelectronic $1T$-TaSe$_2$ offers the possibility to analyze the Mott transition without an interfering CDW transition, as it is controlled by a *continuous* tuning of the U/W ratio, where U is the onsite Hubbard repulsion and W the conduction bandwidth [Perfetti03]. From the phase diagram it can be concluded that the CDW is stronger in the selenide, in the sense that the commensurate state prevails up to 475 K. On the other hand, it will be seen that the tendency towards Mott localization is less pronounced, and an insulating state is not reached in the bulk even down to LHe temperatures. Nevertheless, it is possible to induce a metal-insulator transition at the surface. This bandwidth-controlled transition has the advantage over a filling-controlled transition that there is no disorder involved,

as it is inevitably the case in doping studies.

This chapter is organized as follows. First the system 1T-TaSe$_2$ and its structural properties will be introduced, presenting both the ideal crystal structure and the lattice distortions induced by the charge density wave. Then a brief section provides the experimental details concerning the sample preparation and characterization. The next section discusses the electronic structure of 1T-TaSe$_2$ that was investigated both by theoretical and experimental means. At this point it is remarked that a great number of studies already exist examining the electronic structure of TaSe$_2$ [Smith75, Myron75, Woolley77, Aebi01, Horiba02, Aiura03a, Bovet04, Clerc04]. Hence this investigation focusses on certain aspects of the electronic structure and the CDW-induced changes, paving the way for the surface metal-insulator transition, which will finally be addressed.

## 4.2 Crystal Structure and Charge Density Wave

1T-TaSe$_2$ belongs to the family of transition metal dichalcogenides, which possess a layered crystal structure with the basic building blocks consisting of one hexagonal sheet of transition metal atoms sandwiched between two sheets of hexagonally packed chalcogen atoms. These layers repeat along the crystallographic c direction, as depicted in Fig. 4.1 (a). While strong ionic and covalent bonding predominates within the layers, weak van der Waals forces act between them.

Two different possibilities of ligand coordination exist for the Ta ions: They can either be in an octahedral or in a trigonal prismatic environment of Se ions, displayed in Panels (b) and (c). Different stacking orders of the ligand sheets give rise to pure octahedral, pure trigonal prismatic or mixed coordination polytypes. The point symmetry is denoted by T (trigonal), H (hexagonal), or R (rhombohedral) [Lieth77]. Whereas a unit cell in 1T-TaSe$_2$ extends over only one layer in the c dimension, the periodicity is doubled in the 2H polytype in order to reach a stable configuration.

The basic structure of 1T-TaSe$_2$ is of CdI$_2$ type, with space group $P\bar{3}m1$ and lattice parameters $a = 3.4733$ Å and $c = 6.2715$ Å at room temperature [Wiegers01]. This crystal structure can be viewed as an almost perfect hexagonal close packing of the anions, with the cations in the octahedral interstitials. Note that the rotation axis contained in this space group is only threefold and not sixfold, as one could naively conclude from the hexagonal sheets of metal and ligand atoms. With a ratio $c/a = 1.806$ deviating from the ideal value of 1.633, the coordinating octahedra are trigonally distorted, viz., elongated in the c dimension.

The corresponding Brillouin zone with the conventional high-symmetry points is displayed in Fig. 4.1 (d). While all six corners of a hexagon in one plane of the Brillouin zone are equivalent, as for instance the K-points, one has to distinguish between M- and M'-points on the edges of the hexagon.

For the further investigation of 1T-TaSe$_2$ it is important to note that the crystal structure of the 1T polytype is distorted by a commensurate charge density wave at
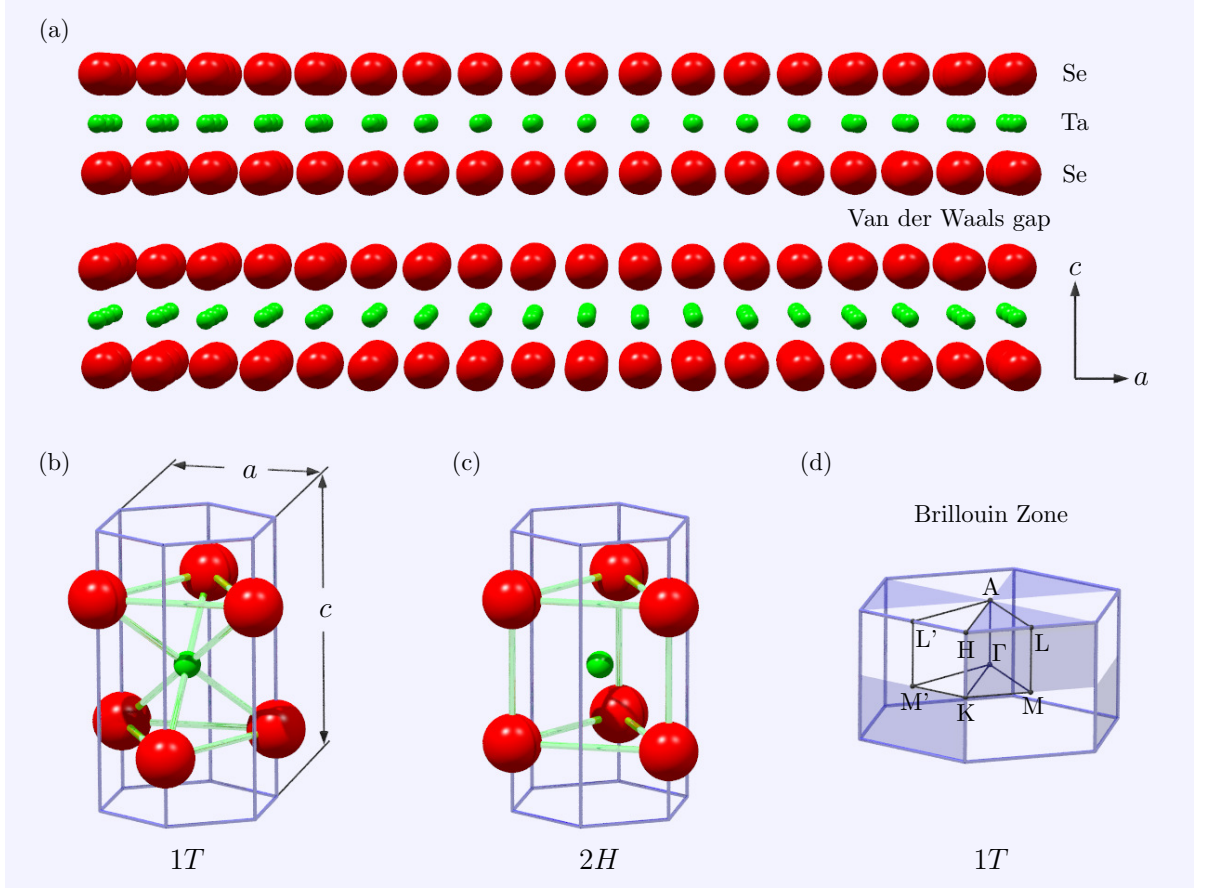
Figure 4.1: *Basic structure of 1T-TaSe$_2$. (a) Layered crystal structure consisting of Se–Ta–Se sandwiches separated by van der Waals gaps. (b,c) Octahedral and trigonal prismatic coordination of the cations in the 1T and 2H polytype. (d) 1T Brillouin zone with the conventional high-symmetry points.*

room temperature. The above described basic structure serves as a fundament for the description of the $\sqrt{13} \times \sqrt{13}$ superstructure adopted by the compound below 475 K [Wilson75]. Heating above this temperature takes the system from the commensurate into an incommensurate state via a first order phase transition. The normal state cannot be reached by heating to higher temperatures, as 1T-TaSe$_2$ is only metastable below 870 K and is thus irreversibly transformed into the 2H polytype at approximately 600 K. The CDW distorted state is characterized by a $\sqrt{13} \times \sqrt{13}$ superlattice, which is rotated by 13.9° with respect to the original lattice [Brouwer80]. The basal plane unit cell contains 13 Ta atoms, which are arranged in star-of-David-shaped clusters, as depicted in Fig. 4.2 (a). The atoms on the inner ring of a cluster move closer to the center atom — an effect of approximately 7% at room temperature [Wiegers01]. The six outer atoms are situated asymmetrically with respect to the inner hexagon, again with a shorter distance to these atoms than the average Ta–Ta distance. As a consequence of this clustering of Ta atoms, the Se atoms residing approximately above the centers of the clusters are

(a)

(b)

M

K

Γ

+ — undistorted structure

• — CDW distorted structure
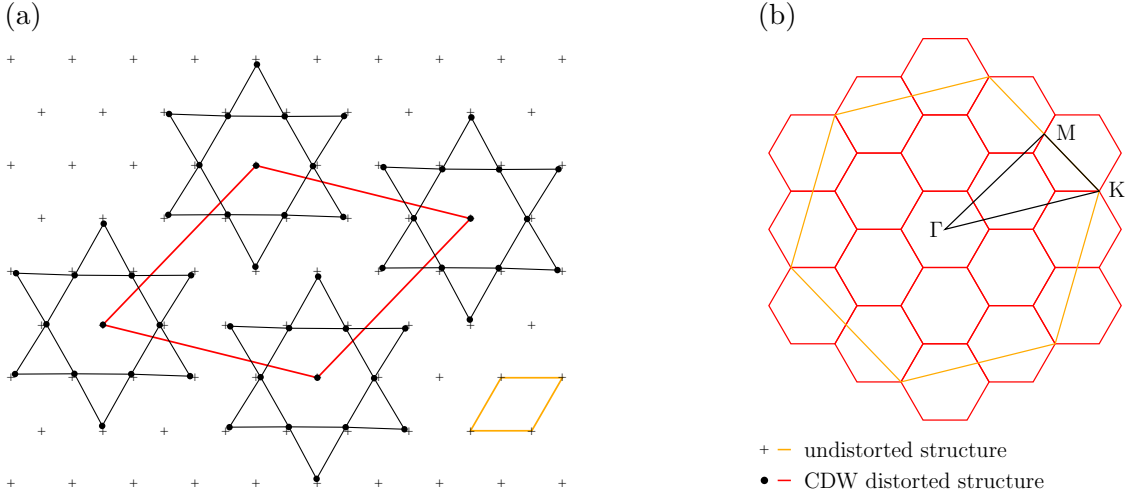
Figure 4.2: *(a) Ta sites forming star-of-David clusters in the commensurate CDW phase. Atomic positions are taken from Ref. [Wiegers01]. The unit cells of the undistorted 1T phase and of the CDW distorted phase are indicated in amber and red colors, respectively. (b) Brillouin zone projections of the undistorted lattice (amber) and of the $\sqrt{13} \times \sqrt{13}$ superlattice (red).*

shifted away from the central Ta plane. The Se atoms in between the clusters are shifted towards the central Ta plane. The resulting buckled sheets of Se atoms lead to a new periodicity along the c axis, viz., 13 times the value of the basic structure, as the relative phases of the CDW on neighboring layers is governed by the Se–Se contacts between those layers. The new, smaller Brillouin zone of the CDW superstructure is displayed together with the one of the basic structure in Panel (b).

4.3 Sample Preparation and Characterization

1T-TaSe$_2$ was synthesized from the elements with the chemical vapor transport technique. For a more detailed description of this method, confer Section 5.3. Here, only a brief account of the parameters is given [Huisman69, DiSalvo74, Slough86, Buslaps91]. Approximately 5 g of Ta and the amount of Se corresponding to a Se excess of 2 mg/cm^3 was brought into quartz ampoules of 20 cm length. Iodine was used as transport agent with a concentration of 5 mg/cm^3. The crystals were grown at a temperature of ≈ 960°C in a temperature gradient of 40°C along the ampoule length. Before the stable growth phase of 18 days, the direction of the temperature gradient was repeatedly switched for one to three days in order to dissolve the smallest of the developing crystals. In this way the formation of polycrystalline clusters is impeded in favor of larger undisturbed single crystals. As a result of this approach, a quartz tube typically contained several single crystal platelets with an in-plane dimension of the order of 5 mm and a thickness of approximately 0.5 mm.
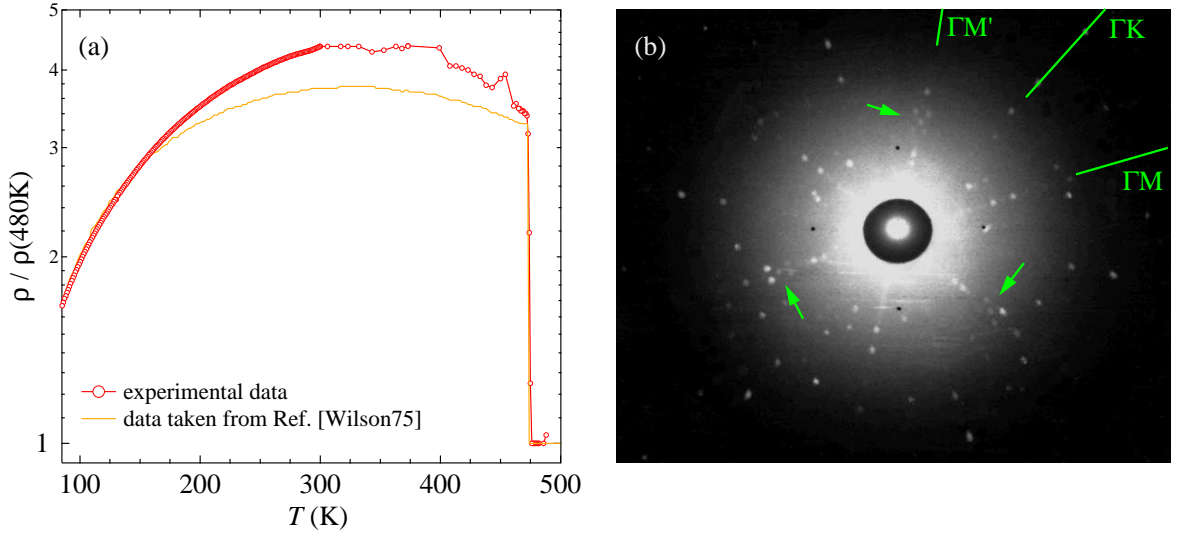
Figure 4.3: *(a) Resistivity of a 1T-TaSe$_2$ single crystal measured by the four-point method compared to published results [Wilson75]. Above and below 300 K different sample holders were used; the pronounced noise in the data is partly due to the instability of the solder contacts at elevated temperatures. (b) Laue photography of a 1T-TaSe$_2$ crystal ($U_A = 25$ kV). Arrows point to features that demonstrate the threefold symmetry of the pattern.*

Since the 2H polytype is the stable form of TaSe$_2$ at room temperature, it is important to avoid that the crystals are transformed from the high temperature 1T polytype into the 2H polytype after the end of the growth process. For this reason, the crystals were rapidly quenched by shooting the ampoules out of the furnace into a basin of ice water. The large majority of the resulting crystals could already be classified by inspection with the bare eye to be the correct 1T polymorph, evident from their shiny golden color, which clearly differs from the silver or black color of the other possible polytypes. Only a few crystals, primarily those in large clusters without direct contact to the wall of the quartz tubes were apparently not quenched fast enough, as their silver color hinted to the 2H polytype.

The classification into the 1T or 2H type is unambiguous when the conductivity is considered. The 1T polytype is characterized by a first-order incommensurate-to-commensurate phase transition of the charge density wave at 475 K, both states being metallic. On the other hand, the 2H phase exhibits a second-order phase transition at 120 K. Below this temperature the compound is in a 3×3 charge density wave state, above this transition it is in the normal, undistorted state. The results of DC transport measurements carried out on a single crystal are plotted in Fig. 4.3 (a). From the comparison to the data of Ref. [Wilson75] one can deduce that the sample must indeed be assigned to the 1T polytype. Even though the temperature dependence of the two curves is not identical in the whole temperature range, the position of the phase transition coincides in both data sets, and also the jump height is reproduced.

A further feature to distinguish the two polytypes can be found in the Laue diffraction pattern. While the structure of the $1T$ polytype is characterized by a *threefold* symmetry, a *sixfold* rotation axis is contained in the point group of the $2H$ form. By close inspection of the Laue diffractogram displayed in Fig. 4.3 (b), features can be identified that occur only every 120°, and thus confirm the threefold symmetry of the sample. The arrows point to features resembling the number five on a dice that occur exactly three times on a full turn. In order to determine the crystals' orientation, the Laue pattern was simulated with the LaueX software [Soyer96]. From the comparison of the experimental diagram with the simulation, it can be inferred that the marked features are located on the line parallel to the ΓM' direction. The other directions then follow straightforwardly.

4.4 Electronic Structure

In the following the electronic structure of $1T$-TaSe$_2$ in its normal state and in the presence of the charge density wave will be presented, serving as a fundament for the metal-insulator transition in the focus of the next section.

In a local picture, the electronic structure of $1T$-TaSe$_2$ is determined by the $5d^1$ configuration of the Ta atom. The odd number of valence electrons produces a metallic conductivity, since the onsite Coulomb repulsion is apparently not strong enough to induce a Mott insulating state. This is not surprising given that the $5d$ shell stretches out much farther in space than the orbitals of the $3d$ compounds, which are often found to be Mott insulators. As a consequence of the octahedral coordination of the $1T$ polytype, the $5d$ levels are expected to split up in the crystal field into t_{2g} and e_g states, with the single electron residing in the lower lying t_{2g} manifold. As pointed out in Section 4.2, the coordinating octahedra are elongated along the crystallographic c direction. This effect, amounting to approximately 5% [Wiegers01], is responsible for the lifting of the degeneracy of the t_{2g} triplet. With the basis of the local coordinate system x, y, and z chosen to coincide with the crystallographic axes a, b, and c,[1] in many transition metal dichalcogenides the t_{2g} orbital with $d_{3z^2-r^2}$ symmetry is occupied, which points along the c axis.

This simple picture of the electronic structure is confirmed by DFT calculations carried out by Dr. Eyert. The calculations were performed in the local density approximation (LDA) using a new implementation of the scalar-relativistic augmented spherical wave (ASW) method [Eyert00]. In order to represent the correct shape of the crystal potential in the large voids of the open crystal structures, additional augmentation spheres were inserted. Optimal augmentation sphere positions as well as radii of all spheres were automatically generated by the sphere geometry optimization algorithm [Eyert98]. Self-consistency was achieved by a highly efficient algorithm for convergence acceleration [Eyert96]. Brillouin zone sampling was done using an increased number of **k**-points ranging from 63 to 6975 points within the irreducible wedge of the hexagonal Brillouin

---

[1]Note that this coordinate system does not coincide with the axes of the coordinating octahedra.
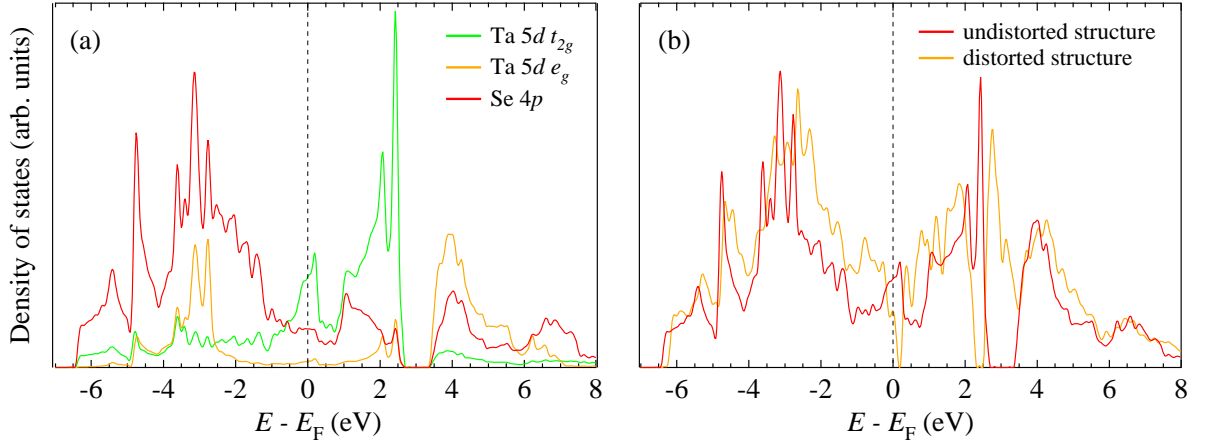
Figure 4.4: *$1T$-TaSe$_2$ density of states obtained by DFT calculations. (a) LDA density of states decomposed into Ta t_{2g}, Ta e_g, and Se contributions, calculated for the ideal $1T$ structure. The Se states strongly hybridize with the Ta derived states. (b) LDA density of states of the ideal structure and of the CDW distorted structure. At the Fermi level, the density of states is suppressed due to the lattice distortion, and an additional gap opens up approximately $0.2\,eV$ above the chemical potential.*

zone in the $1T$ structure. In contrast, for the distorted trigonal low-temperature structure 32 to 864 irreducible points were used. In all calculations the basis set consisted of Ta $6s$, $6p$, $5d$, and $5f$ as well as Se $4s$, $4p$, and $4d$ orbitals, which were treated as valence states.

The density of states calculated for the ideal $1T$ structure is shown in Fig. 4.4 (a). Apparently, both atomic species contribute considerably to the valence band in its full energy range. This is a special feature of $1T$-TaSe$_2$ — in marked contrast to the sulfide, where the Ta and S levels are much less hybridized. This difference is primarily responsible for the different behavior of the Peierls and Mott physics that is found in the two isostructural and isoelectronic compounds.

Around the Fermi energy, the states clearly are of t_{2g} nature. The unoccupied e_g states are separated by a crystal field splitting of approximately $1\,\text{eV}$. The orbital character of the Ta $5d$ band crossing the Fermi energy was identified to be predominantly $d_{3z^2-r^2}$ (not shown), as expected from the trigonal distortion of the coordinating octahedra. Minor contributions come from $d_{x^2-y^2}$ orbitals, and from the d_{xz} orbital with e_g symmetry. This is possibly another distinctive feature with respect to the sulfide, for which it was recently proposed on the basis of tight-binding calculations that the $d_{x^2-y^2}$ and d_{xy} states are of comparable or even larger importance [Rossnagel06].

Panel (b) shows how the electronic structure is altered by the CDW-induced reconstruction of the lattice. As expected for a quasi-two-dimensional system, the nested parts of the Fermi surface become gapped, which is responsible for the observed suppression of the DOS at the Fermi energy. Note, however, that the spectral weight is not completely removed from the Fermi level and that the LDA calculation hence correctly
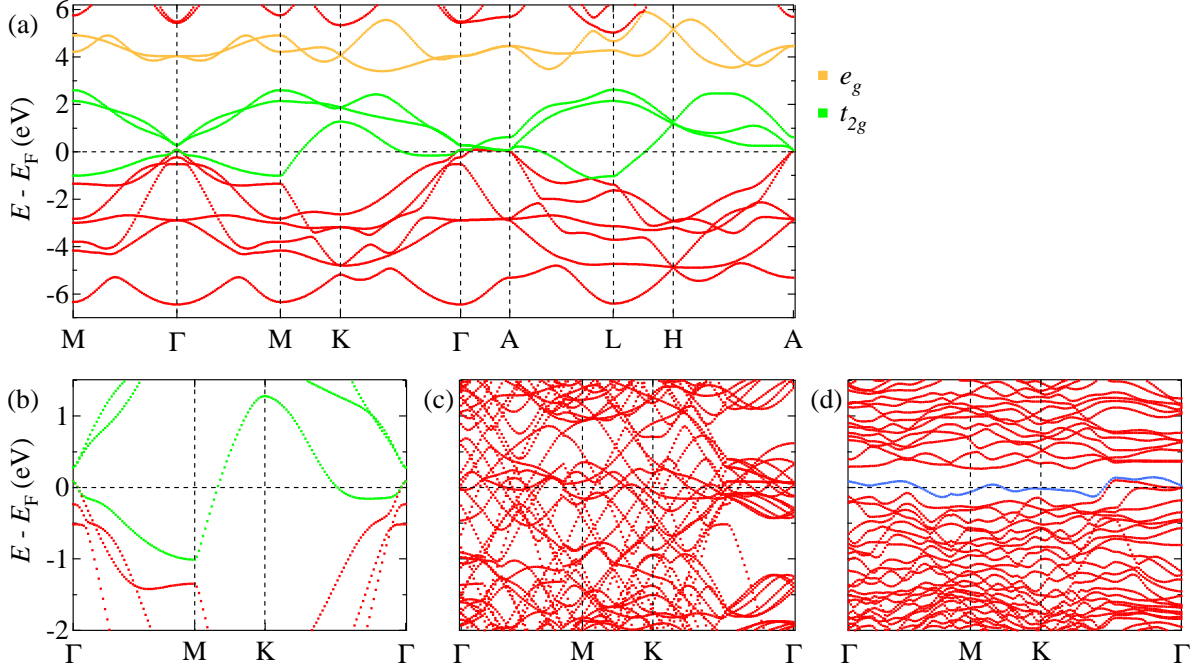
Figure 4.5: *1T-TaSe$_2$ band structure obtained by DFT calculations. (a) Electron dispersions calculated for the ideal 1T structure. Ta 5d bands with predominant t_{2g} and e_g character are plotted in green and amber colors, respectively. (b) Band structure of the ideal 1T structure in a reduced energy range, plotted along the high symmetry paths of the ΓMK plane only. (c) Band structure of the ideal 1T structure, but with a 13fold superlattice. The bands are displayed in the original Brillouin zone, i.e., the paths correspond to the symmetry directions in the Brillouin zone of the unreconstructed crystal. (d) Band structure of the CDW distorted lattice, displayed in the the original Brillouin zone. A separated band (blue) with a width of approximately 0.35 eV emerges at the Fermi level.*

yields a metallic CDW state. Electronic correlations, which are not adequately treated in this DFT approach, are expected to further diminish the quasiparticle weight at the Fermi energy.

A deeper insight into the CDW-induced modifications of the electronic structure is gained by examining the *band structure* obtained from the DFT calculations. Fig. 4.5 (a) shows the electronic dispersions of the ideal 1T structure along certain high symmetry paths in the first Brillouin zone. The bands of predominantly Ta 5d t_{2g} and e_g character are drawn in green and amber, respectively. Note, however, that this classification is not absolute, but shall rather be understood as a tendency. Of course, the Bloch waves corresponding to a band derived from a certain d orbital contain minor admixtures of other d orbitals, too. As expected from the layered crystal structure of 1T-TaSe$_2$ the strongest band dispersions are found in the planes parallel to the crystal layers, e.g., along the paths ΓM or MK. However, non-vanishing band dispersions are also found along the ΓA path, which is perpendicular to the crystal layers. This effect can be attributed to the comparatively strong hybridization of Ta and Se states, which is more

pronounced in the Selenide as for instance in the related compound $1T$-TaS_2 and hence causes a more three-dimensional electronic structure [Horiba02].

In order to understand the effects of the CDW, additionally the band structure was calculated for the same unreconstructed crystal structure but in the superlattice of the $\sqrt{13} \times \sqrt{13}$ CDW phase, leading to the 13fold number of bands, as shown in Panel (c). However, these Umklapp bands are still plotted in the larger Brillouin zone of the undistorted lattice. The relationship between the considered high-symmetry paths of the ideal $1T$ crystal structure and the Brillouin zones of the reconstructed lattice is illustrated in Fig. 4.2 (b). Although the basic principle is the same as the back-folding into a Brillouin zone of half the original size for a one-dimensional system (cf. Fig. 2.7), the changes induced by the $\sqrt{13} \times \sqrt{13}$ distortion are obviously more complex, as the back-folding involves 13 bands.

Switching on now the CDW potential leads to the band structure displayed in Panel (d) of Fig. 4.5. Many of the band crossings are removed by the inclusion of the CDW. As an interesting result, a single band at the Fermi energy stands out that is notably separated from the others. In the ionic picture, where each Ta atom is left with one valence electron, this band hosts the last and 13th Ta $5d$ electron and is therefore half-filled. This is reminiscent of the results of Smith *et al.*, who chose a similar approach to calculate the band structure of $1T$-TaS_2 [Smith85]. They obtained that the Ta $5d$ band collapses into three sub-bands, with a topmost conduction band of only $50\,meV$ width. Their tight binding calculation considered only the Ta $5d$ band and did not include S $3p$ contributions. In the selenide, however, the ligand contribution cannot be neglected due to the strong cation-anion hybridization. As a marked difference to the sulfide results of Smith *et al.*, the DFT calculations for the related compound $1T$-$TaSe_2$ *do not* yield a separation into three sub-bands.

The effect of a single band at the Fermi energy being split-off might even be further enhanced if the spin-orbit interaction were included in the calculations, as it was observed by a tight-binding simulation for the related sulfide compound [Rossnagel06]. Indeed, one would expect that spin-orbit coupling plays a non-negligible role, given the high atomic number of Ta.

The above described theoretically obtained information on the electronic structure can be tested experimentally by photoelectron spectroscopy. Both angle-integrated and angle-resolved measurements were performed in the homelab using He I radiation ($h\nu = 21.2\,eV$) and an Omicron EA 125 HR electron energy analyzer. The acceptance angle of this analyzer determining the angular resolution is approximately $\pm 1°$ in the angle-resolved mode. The total energy resolution amounted to $\approx 50\,meV$. Additionally, a Fermi surface mapping experiment was carried out at the beamline 7.0.1 of the Advanced Light Source (ALS) in Berkeley, USA, utilizing a goniometer capable of two orthogonal polar rotations. The Scienta SES-100 electron analyzer was operated at an angular resolution of $\approx 0.1°$ and a total energy resolution of $\approx 40\,meV$. The energetic calibration of the photoemission spectra was conducted using the position of a Fermi edge, measured on sputtered silver or gold surfaces.
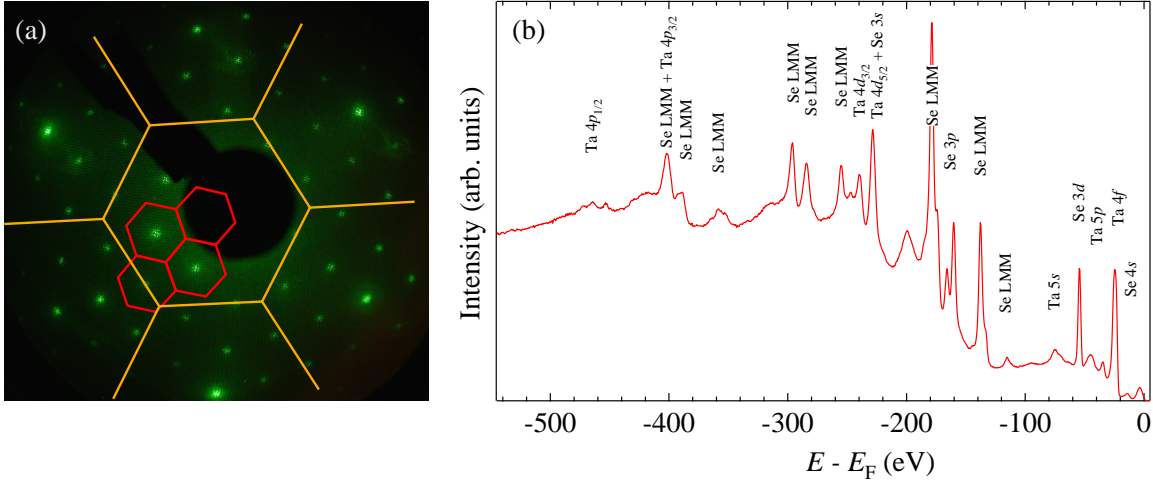
Figure 4.6: *(a) LEED pattern obtained from a cleaved surface of a 1T-TaSe₂ crystal at a primary electron energy of $\approx 80\,eV$. The surface Brillouin zones of the unreconstructed lattice and of the $\sqrt{13} \times \sqrt{13}$ superstructure are indicated by amber and red hexagons, respectively. (b) 1T-TaSe₂ XPS spectrum recorded with AlK_α radiation ($h\nu = 1486.6\,eV$). No indication for oxygen contamination is detected at the O 1s binding energy of 532 eV. A possible C 1s peak at 285 eV cannot be found as it is hidden under a Se Auger line. The unmonochromated x-ray source is responsible for a number of unindexed satellite peaks.*

1T-TaSe₂ crystals were glued with silver epoxy on top of aluminum sample holders, ensuring a good electrical contact to the ground. Fresh surfaces were obtained by *in situ* crystal cleavages that were performed with scotch tape in the fast entry lock of the vacuum system at a pressure of approximately 1×10^{-9} mbar. The resulting surfaces are inert and were not contaminated significantly during the transfer time of typically less than one minute from this pressure into the analysis chamber ($p < 1 \times 10^{-10}$ mbar), as the quasi-two-dimensional crystal structure consists of only loosely coupled layers with saturated bonds. Indeed, long-range ordered surfaces were evidenced by low-energy electron diffraction (LEED) as displayed in Fig. 4.6 (a). The diffraction pattern contains both the reflections of the basic structure, recognizable by their slightly stronger intensity, and the superstructure reflections of the $\sqrt{13} \times \sqrt{13}$ charge density wave. X-ray induced photoemission (XPS) measurements show that the cleaved surfaces are not contaminated by oxygen. In the spectrum plotted in Fig. 4.6 (b) no indication for a O 1s peak can be found. Also a significant contamination of iodine, the transport agent of the crystal growth process, can be ruled out on the basis of the XPS data. Carbon contamination cannot be detected directly, because the C 1s peak at -285 eV is hidden under a Se Auger line. However, the relative intensities of the adjacent Se Auger peaks at -284 eV and -296 eV at least show that there can be no *strong* C 1s contribution.

The results of the angle-resolved photoemission experiments are displayed in Fig. 4.7. Panel (a) shows an intensity plot $I(\mathbf{k}, E)$ of data recorded with He I radiation at room temperature. For the measurement the crystal was oriented along the ΓM line using
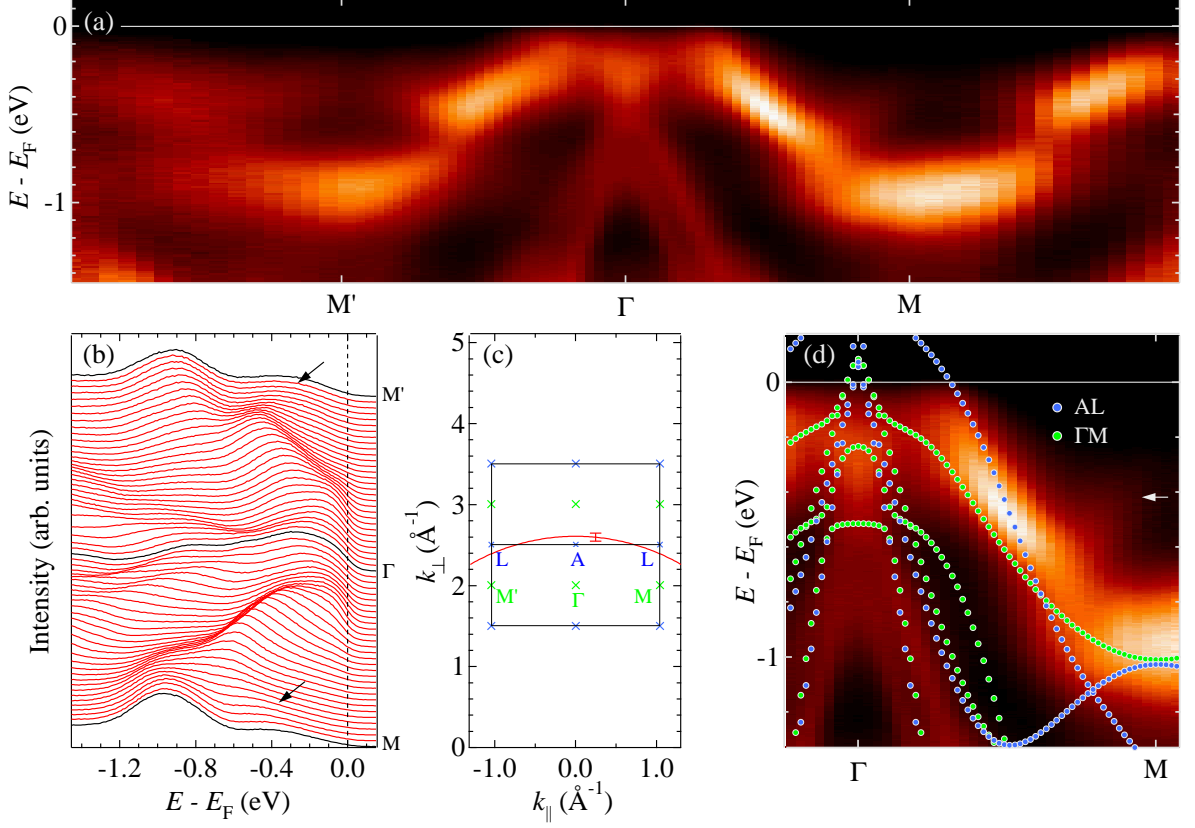
Figure 4.7: *Angle-resolved photoemission of 1T-TaSe$_2$ (hν = 21.2 eV). (a) ARPES intensity plot I($\boldsymbol{k}$, E) covering almost the full path ΓM'ΓMΓ of the original Brillouin zone. Each EDC was normalized to the same integrated intensity. (b) ARPES EDCs measured along the MΓM' path. Arrows mark CDW-induced structures. (c) Cross section of Brillouin zones in the ΓALM plane. The path sampled by the experiment with HeI photons as estimated from Equation 3.5 is indicated in red. (d) ARPES data compared to DFT bands of the ideal 1T structure along the paths ΓM (green) and AL (blue), respectively. Arrows again mark CDW-induced structures that cannot be explained by the calculations.*

its Laue diffractogram, and a very wide angle range from −60° to +60° with respect to normal emission was covered. The corresponding path in reciprocal space is plotted in Panel (c). As discussed in Chapter 3, the component of the wave vector perpendicular to the crystal surface $k_\perp$ can be estimated by Equation 3.5. For the system 1T-TaSe$_2$ an inner potential of $V_0 = 9$ eV was assumed [Buslaps91], and the error bar represents the uncertainty of 1 eV in the choice of V_0. From this calculation it can be seen that the measurement samples a path which is located in the vicinity of the top of the Brillouin zone and is thus closer to the L'AL line than to the M'ΓM line. Nevertheless, the latter nomenclature corresponding to zero perpendicular momentum will be chosen in the remainder of this chapter for simplicity. Turning back now to the photoemission data, Panel (a) clearly shows the symmetry of the dispersions around the central Γ-point. The intensity of the Ta bands is stronger at the M-point than at the M'-point due to matrix

element effects. Upon approaching the Γ-points of the adjacent Brillouin zones, the dispersions do not seem to perfectly reproduce the behavior around the central Γ-point. This fact can probably be traced back to a slight misalignment of the crystal. At about $\pm 1/4\Gamma M$ a band is found to cross the Fermi energy, indicating the metallic nature of the CDW phase of 1T-TaSe$_2$.

The same data set is displayed, in a reduced k range, in Panel (b) as energy distribution curves (EDCs). In this representation of the data, the steeply dispersing feature around Γ is clearly resolved to consist of two different bands. A detailed discussion of this splitting can be found in Ref. [Clerc04], where it is shown that both the crystal symmetry and the spin-orbit interaction are responsible for this effect.

A comparison of the experimental data with the calculated band structure is shown in Panel (d). Both the DFT bands along the ΓM line (green) and along the AL line (blue) are plotted in this graph. As argued above, the calculated bands along the latter path are rather suited to be compared to the photoemission data. Indeed, a better agreement between experiment and theory is found when this path is considered, especially as far as the location of the Fermi vector k_F is concerned. Note, however, that the photoemission experiment with He I radiation primarily probes the *surface* electronic properties. The escape depth of electrons stemming from the Fermi level approximately corresponds to one interlayer distance of 1T-TaSe$_2$. The DFT calculation, on the other hand, describes the *bulk* electronic structure, so that a consistent comparison is, strictly speaking, not possible. As a loophole, it is common practice in the transition metal dichalcogenides to regard the surface electronic structure as being only marginally different from that of the bulk due to the quasi-two-dimensional crystal structure. Each layer only weakly interacts with the adjacent layers by van der Waals forces, and for the surface layer the absence of one neighboring layer is thus regarded as a minor perturbation. However, it shall be warningly remarked at this point that the anisotropy of the electronic structure is rather weakly pronounced in this system compared to other dichalcogenides. Consequently, the difference between surface and bulk electronic properties might be larger in the selenide than, e.g., in the sulfide.

By comparison of the measured and calculated band structure, the topmost narrow experimental band can be identified as being derived mainly from Ta 5d levels, whereas the steep and less intense bands are mainly formed out of Se 4p levels. It is again emphasized, however, that a strong hybridization of Ta and Se states is present in this compound.

At first glance it seems surprising that the experimental band structure — obtained at room temperature — qualitatively agrees with the DFT calculation for the ideal, unreconstructed crystal, while it is known that 1T-TaSe$_2$ is in a CDW state at this temperature. One could naively expect that the spectral weight distribution should rather be compared to the band structure displayed in Fig. 4.5 (d), which was calculated for a CDW distorted TaSe$_2$ crystal. However, this inconsistency is resolved when not only the energetic positions (in other words the eigenvalues) at a certain **k**-point are considered, which define the band structure. In fact, it is equally important to consider also

the spectral weight connected with each state, which is determined by the corresponding eigenvector of a certain $E(\mathbf{k})$ value. It was shown in form of a simple example in Ref. [Voit00] that the spectral weight distribution is concentrated on the original band in the extended zone scheme if the disturbing potential of the CDW is much smaller then the crystal potential of the unreconstructed structure. Applied to the related compound $1T\text{-}TaS_x Se_{2-x}$, in which the selenium ligands are partly substituted by sulfur atoms, it was shown by model calculations that the charge density wave causes only minor corrections to the original spectral weight distribution of the unreconstructed state [Aiura03b, Aiura04]. For this reason, it is justified to study the electronic structure in the extended Brillouin zone of the unreconstructed $1T\text{-}TaSe_2$ crystal structure and to compare the experiments to the corresponding calculations disregarding the charge density wave.

Some effects of the CDW can be found in the experimental data, however: Following the Ta $5d$ band on its decreasing path away from Γ, one observes that roughly at $0.8\Gamma M$ ($E = -0.8\,\text{eV}$) the intensity breaks down. The band seems to be continued not only along the straightforward direction, but also a band bending upwards is found, albeit with much weaker intensity. These shadow bands, marked by arrows in Fig. 4.7 (b,d), can be interpreted as band back-folding due to the charge density wave. Also the Se bands show signatures of CDW-induced changes; the steep bands undergo a more subtle intensity modulation at about $-1.25\,\text{eV}$.

Up to this point, all photoemission data were presented as function of energy and one component of $\mathbf{k}_\parallel$, i.e., along certain directions in $\mathbf{k}$-space. An alternative presentation, namely as constant energy cuts through the Brillouin zone, is given in Fig. 4.8. The displayed intensity maps show photoemission data recorded with synchrotron radiation at the ALS. The photon energy of $h\nu = 110\,\text{eV}$ was chosen such that the probed electronic states in the sample are estimated to be located in the vicinity of the Brillouin zone lid, so that the results are comparable to the He I data in this respect (cf. Fig. 4.7 (c)). Panel (a) shows a constant energy surface that was obtained by integrating the photo-emission intensity in an energy window of $0.2\,\text{eV}$ width, centered $0.3\,\text{eV}$ below the Fermi level. The integration window chosen for Panel (b) is centered at the Fermi level, so that the intensity plot corresponds to a Fermi surface map of $1T\text{-}TaSe_2$. In Panel (a) one recognizes elliptically shaped contours stemming from the Ta $5d$ band, which crosses the $E = E_F - 0.3\,\text{eV}$ plane on its way to the Fermi level. These contours qualitatively match the shape of the Fermi surface, as it is expected for a typical $1T$ polytype of a transition metal dichalcogenide. In the particular case of the unreconstructed $TaSe_2$, band structure calculations yield ellipse-like cross sections of the Fermi surface in the ALH plane [Myron75, Woolley77, Sharma02]. This plane approximately corresponds to the $\mathbf{k}$-space surface that was probed in the ARPES experiments. In the ΓMK plane these six ellipses are expected to grow together to a single connected structure. In consistency with these results, the symmetry of the experimental constant energy surface does not show any signs of the $\sqrt{13} \times \sqrt{13}$ superstructure. As a further observation, the intensity in the Brillouin zone centered at zero parallel momentum is found to be much larger
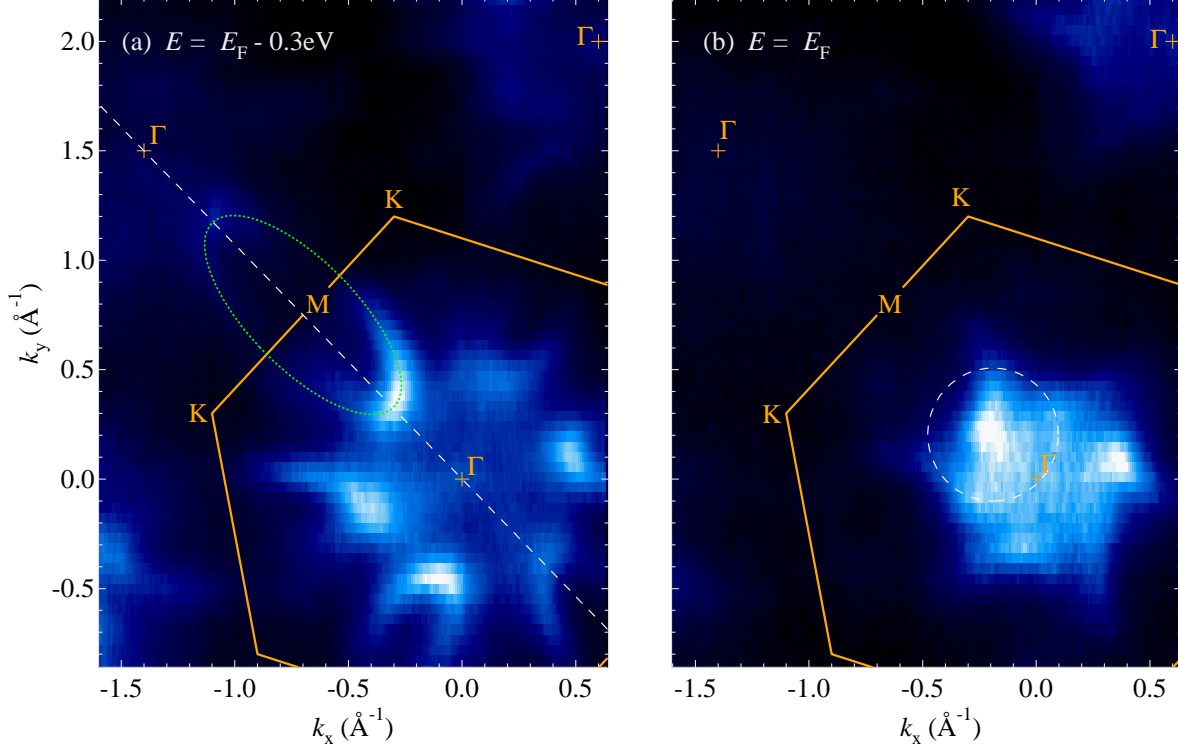
Figure 4.8: *Constant energy intensity maps $I(k_x, k_y)$ of 1T-TaSe₂. (a) Photoemission intensity measured with photons of 110 eV and integrated in an energy window of 0.2 eV centered around $E = E_F - 0.3$ eV. The first Brillouin zone of the unreconstructed lattice is indicated in amber color together with certain high symmetry points. The path $\Gamma M \Gamma$ of the measurements in Fig. 4.7 is shown as a white line. The green ellipse serves as a guide to the eye to follow the constant energy surface. (b) Fermi surface map ($E = E_F$). The white circle indicates the estimated area covered by the angle-integrated measurements of Fig. 4.10.*

compared to the adjacent Brillouin zones. This could by explained as a photoemission matrix element effect, as the intensity from Ta $5d_{3z^2-r^2}$ electrons is expected to decrease with increasing emission angle ϑ proportional to $|Y_{20}|^2$, where $Y_{20} = \sqrt{5/16\pi}(3\cos^2\vartheta - 1)$ is the spherical harmonic with $d_{3z^2-r^2}$ character [Aebi01].

The Fermi surface map displayed in Panel (b) deviates from the above described constant energy surface mainly in two regards. Firstly, the apices of the ellipses move towards the Γ-point, an effect which is readily explained by the dispersion of the Ta band displayed in Fig. 4.7 (d). The second and more interesting observation is the almost complete collapse of intensity in the region around the zone boundary where the ellipses possess their smallest curvature. This is exactly the location where Fermi surface nesting would be anticipated. Considering the expectation formulated in Section 2.2, it would be tempting to interpret the suppression of intensity as partial gapping of the Fermi surface induced by the charge density wave. However, the authors of Ref. [Bovet04] attribute this observation to photoemission matrix element effects. They rather propose that
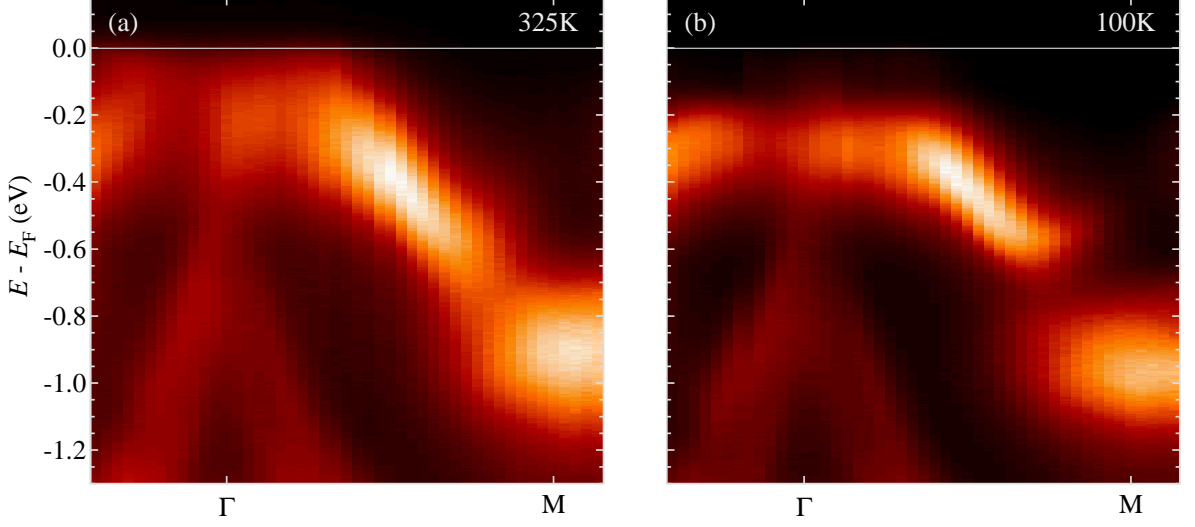
Figure 4.9: *Surface metal-insulator transition in 1T-TaSe$_2$ observed by angle-resolved photoemission (hν = 21.2 eV). (a,b) ARPES intensity plots I($\mathbf{k}$, E) measured at 325 K and 100 K, respectively*

the experimental data hint to a pseudo-gapped Fermi surface, i.e., an overall reduced intensity at the Fermi energy.

Definitely, a more systematic investigation of the electronic structure would be necessary to verify Fermi surface nesting as driving force for the development of a charge density wave in 1T-TaSe$_2$. In particular, this would require to analyze the topography of the Fermi surface in all three dimensions. The band structure calculations yield electronic band dispersions which are not confined to the (a,b) plane, resulting in a relatively pronounced three-dimensional character of the Fermi surface. For a determination of the nesting vector it is therefore essential to regard also the third dimension. In a photoemission experiment, this could be realized by systematically sweeping the photon energy at a synchrotron source.

4.5 Surface Metal-Insulator Transition

Whereas the difference between bulk and surface electronic structure was treated in the previous section as being small enough to reasonably facilitate a comparison between photoemission data and band structure calculations, this section focusses on an effect which is brought about by exactly this difference. A metal-insulator transition will be presented that occurs at the *surface* of 1T-TaSe$_2$, but not in the *bulk* [Perfetti03].

Figure 4.9 shows angle resolved photoemission data recorded at 325 K and 100 K, respectively. The data of both intensity maps thus belong to the same $\sqrt{13} \times \sqrt{13}$ CDW phase of 1T-TaSe$_2$. However a drastic difference is evident when both data sets are compared. The high-temperature measurement yields a *metallic* behavior with the Ta 5d
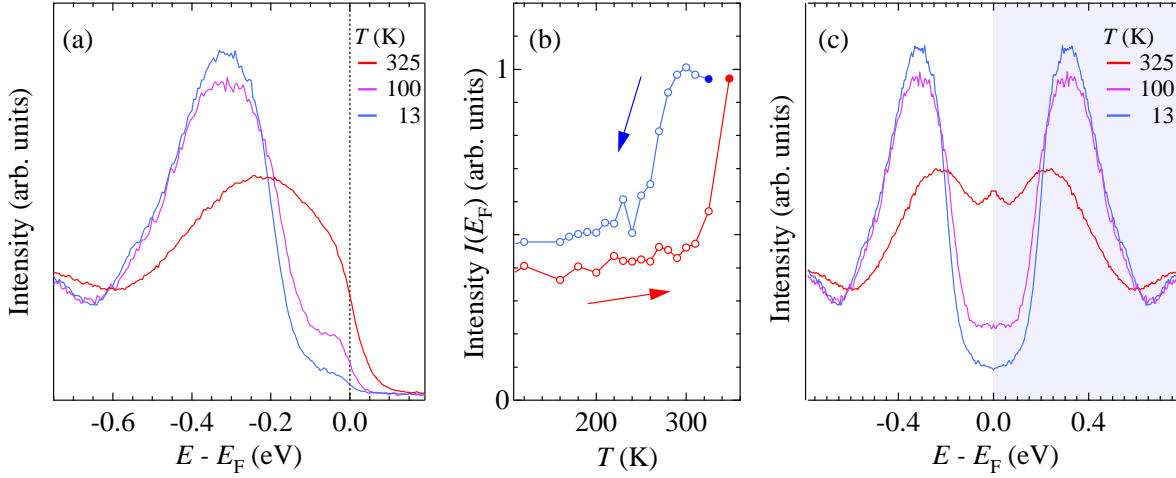
Figure 4.10: *Surface metal-insulator transition in 1T-TaSe$_2$ observed by angle-integrated photoemission (hν = 21.2 eV). (a) Angle-integrated photoemission intensity $I(E)$ recorded at the Fermi wave vector on the ΓM line (cf. Fig. 4.8 (b)) and normalized to the same integrated area. (b) Temperature dependence of the intensity at the Fermi level. The transition shows a large hysteresis. (c) Symmetrized photoemission intensity $I_s(E) = I(E) + I(-E)$ (for details, see text).*

band crossing the Fermi level at $\approx \pm 1/4$ΓM, as discussed in the previous section. In contrast, at low temperature the spectral weight is clearly shifted away from the Fermi level and a gap appears. Further photoemission measurements carried out with synchrotron radiation at the ALS have shown that this gapping affects the complete Fermi surface and not only the Fermi wave vectors lying on the M'ΓM line, thus signalling a truly *insulating* state. However, it is well established that the commensurate phase of bulk 1T-TaSe$_2$ is metallic, as seen for instance in the dc transport measurement of Fig. 4.3. Therefore, the conclusion must be drawn that the observed metal-insulator transition affects only the surface, which is mainly probed in the photoemission experiment. As already mentioned, the escape depth of He I excited electrons corresponds to roughly one interlayer distance, i.e., approximately two thirds of the photoemission information stem from the topmost sandwich layer, and another 20% from the second.

The angle-integrated photoemission data presented in Fig. 4.10 provide further evidence that the observed gap extends over the complete Fermi surface. The spectra were recorded in the angle-integrated mode of the Omicron analyzer, thus counting the photoelectrons with an emission angle $\vartheta \leq 8°$. The area covered in reciprocal space by this measurement is indicated in Fig. 4.8 (b). One can see that a large portion of the Fermi surface is thus taken account of, having in mind that only the asymmetric unit of the Brillouin zone with its threefold symmetry has to be considered. The three spectra shown in Panel (a) reveal a suppression of intensity at the Fermi level below the transition temperature, the fingerprint of the metal-insulator transition. Note, however, that the intensity does not drop to zero, but that a shoulder of remnant intensity persists at the Fermi energy. This intensity is probably due to emission from the bulk. The decline

of remnant intensity with decreasing temperature can be taken as a sign that the surface region undergoing the transition into an insulating state reaches deeper and deeper into the bulk.

The transition temperature can be inferred from the temperature dependence of the signal at the Fermi level depicted in Panel (b). The cooling curve shows a sudden drop of intensity at about 270 K, followed by a rather flat decline, which is attributed to the increasing extent of the insulating zone at the surface. The heating curve is characterized by a strongly delayed recovering of intensity, which is an indication for a first-order phase transition. Above 350 K the hysteresis curve is closed again. This is confirmed by an inspection of the angle-integrated spectra that correspond to the points marked by filled symbols in Panel (b), yielding an exact match of the spectral shapes (not shown).

Below the phase transition, it sticks out that the cooling and heating curves do not come to lie on top of each other. This could be a consequence of pinning effects: The deepest extent of the insulating region, reached at the lowest temperature of the experiment, will not immediately recede upon heating when it is pinned at structural defects. It must be stressed at this point that the metal-insulator transition was found to be very sensitive to the surface quality. Depending on the quality of the cleavage surface and on the exposure to possible contaminants during the experiment, several samples did not show a surface transition at all. The strong dependency on sample quality is also mentioned in Ref. [Colonna05].

Coming now to the question what the nature of the observed phase transition is, it must be stated first that structural changes can be ruled out for several reasons. For the bulk it is obvious that no structural phase transition occurs in the relevant temperature range, as measurements of the resistivity and magnetization show (cf. Fig. 4.3 and Refs. [DiSalvo74, Wilson75]). In order to exclude this possibility also for the surface, LEED measurements were performed in the temperature interval from 100 K to 300 K with a primary electron energy of 60 eV and 100 eV, respectively. In accordance with Ref. [Perfetti03] the LEED patterns demonstrate the identical surface symmetry of the metallic and insulating phase (not shown). Finally it is added that the scanning tunnelling microscopy (STM) results of Colonna *et al.* do not display signs of structural changes at the surface, either [Colonna05].

The observed spectral changes must thus be attributed to an electronic transition. In the following it will be argued that the appearance of a gap is the signature of a first-order Mott transition, which is driven by a CDW-induced reduction of the electronic bandwidth. The spectral form of the angle-integrated photoemission signal is suited to support this interpretation. From DMFT calculations it is known that a Mott metal-insulator transition is characterized by the disappearance of the quasiparticle peak in favor of the lower and upper Hubbard bands. Indeed, such a behavior can be found in the experimental data, albeit obscured by the effect of the Fermi distribution, since the photoemission signal is proportional to the product of the spectral function $A(E)$ and the Fermi distribution $f(E)$. The perturbing effect of $f(E)$ can be removed by a symmetrization procedure: Assuming that particle-hole symmetry holds sufficiently close to

the Fermi energy, i.e., $A(E) = A(-E)$, one can utilize the relation $f(E) + f(-E) = 1$ by considering the symmetrized photoemission intensity $I_s(E) = I(E) + I(-E)$. Then the Fermi distribution cancels out. The photoemission signal symmetrized in this way is plotted in Fig. 4.10 (c) for different temperatures. It is explicitly pointed out, however, that these spectra are not intended for a discussion outside a small energy window around E_F. The result of this procedure is certainly not valid far away from the Fermi level due to the absence of electron-hole symmetry in 1T-TaSe$_2$. The symmetrization shall merely serve as a tool to illustrate the evolution of the spectra close to E_F. In the spectrum measured above the transition the typical three-peak structure is recognized with a quasiparticle peak at the Fermi energy. For the emergence of this feature in the symmetrization procedure the exact position of the Fermi level is crucial. The Fermi energy was therefore determined very carefully by measuring a silver foil at the same experimental conditions. Lowering the temperature leads to a disappearance of the quasiparticle feature in the insulating phase and a transfer of spectral weight to the side bands, which are interpreted as lower and upper Hubbard bands in the Mott picture. Overall, a qualitative agreement with the theoretical DMFT predictions for a Mott transition presented in Section 2.1 is found, albeit with a rather weakly developed quasiparticle peak. This not surprising though, considering the large value of the resistivity of bulk 1T-TaSe$_2$ at room temperature of $2 \times 10^{-3}\,\Omega\text{cm}$ [DiSalvo74] — approximately three orders of magnitude higher than copper.

From the distance of the upper and lower Hubbard bands, the value of 0.6 eV for the onsite Coulomb repulsion can be estimated very crudely, keeping in mind that only the occupied part of the density of states can be measured. A recent scanning tunnelling study, which has the advantage that both the occupied and the unoccupied states can be probed, obtains a value of 0.38 eV for this distance. In contradiction to electron-hole symmetry, it finds the upper Hubbard band to lie much closer to the Fermi level than the lower one [Colonna05].

The question that remains to be answered is: What mechanism triggers the Mott transition at the surface of 1T-TaSe$_2$ — but obviously leaves the bulk in a metallic state? First of all it is pointed out that a Mott transition is usually expected in systems involving $4f$, $5f$, or $3d$ electrons, systems which are characterized by a strong electronic confinement in space and therefore a large onsite Coulomb repulsion. Famous examples for Mott insulators among the $3d$ transition metal compounds are V$_2$O$_3$, NiO, or La$_2$CuO$_4$ [Mott49, Fulde91, Fazekas99a]. Also the material discussed in the following chapter, TiOCl, falls into this category. In 1T-TaSe$_2$ with its $5d$ electron system the Coulomb repulsion is much weaker. As discussed above, the Hubbard U was estimated as 0.38 eV, which is almost an order of magnitude smaller than the corresponding value of TiOCl. Nevertheless, a ratio U/W large enough to induce a Mott transition is possible in TaSe$_2$ due to the reduction of the electronic bandwidth caused by the charge density wave. The magnitude of this effect can be appreciated by inspecting the DFT calculations shown in Fig. 4.5. Whereas the unreconstructed crystal possesses a Ta $5d$ band with a width of ≈ 2.3 eV, the bandwidth is reduced to only 0.3 eV taking into
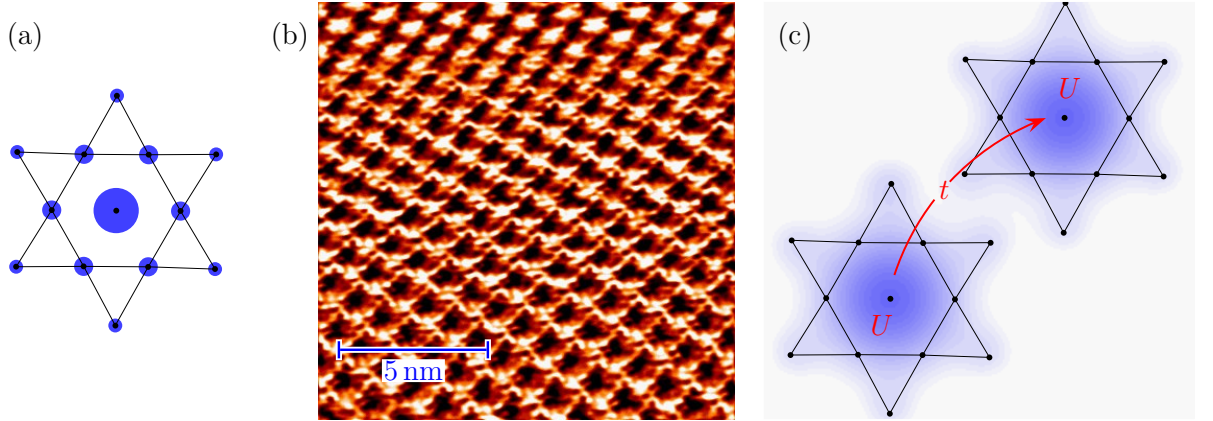
Figure 4.11: *Role of the CDW in the Mott-Hubbard scenario. (a) Contributions of the inequivalent Ta sites to the density of states at the Fermi level, indicated by the symbol size. (b) STM image of the $1T$-TaSe$_2$ surface at $300\,K$ showing clusters with bright intensity ($I = 3\,nA$, $V = -75\,meV$). (c) Sketch illustrating the interpretation of the star-of-David cluster orbitals as the sites of the Hubbard model.*

account the lattice distortion of the CDW. The ratio U/W is hence greater than unity in the CDW phase of $1T$-TaSe$_2$.

In order to get an intuitive picture of this Mott-Hubbard scenario, it is helpful to take a closer look at the separated band drawn in blue in Fig. 4.5 (d). The DFT calculations yield that the various inequivalent Ta sites of the star-of-David structures contribute quite differently to the density of states at the Fermi energy. If one divides the different Ta sites roughly into three categories — the center atom, the atoms in the inner ring, and the atoms in the outer ring —, the average respective contributions amount to 13%, 5.5%, and 4%, respectively. The residual 30% are distributed relatively homogeneously among the remaining 26 Se atoms. This result is illustrated in Fig. 4.11 (a), where the symbol size represents the DOS contribution of each Ta atom. From this result it becomes qualitatively clear that instead of considering simple orbitals at the Ta sites, one should rather consider "molecular" orbitals, which have to be attributed to the star-of-David clusters. The topmost occupied band is then formed by overlapping wavefunctions that are peaked in the center region and decrease towards the edges of the stars. With this notion of the low-energy electronic orbital the interpretation of the STM image depicted in Panel (b) becomes obvious. The image was recorded with an Omicron variable temperature STM at constant tunnelling current of $3\,nA$ and with a sample bias of -75 meV (thus probing the occupied states). Single atoms are weakly recognizable, even though the image is clearly dominated by the symmetry of the $\sqrt{13}\times\sqrt{13}$ superstructure with bright areas that are identified as the centers of the star-of-David clusters. A coarse analysis of the distances shows that this interpretation is consistent with the supercell size expected from x-ray diffraction [Wiegers01].

In the Mott-Hubbard picture, the local Coulomb energy U and the hopping parameter t must accordingly be also defined in the light of the CDW-induced modifications of the

electronic structure: Instead of the single metal atoms which are usually identified as the sites relevant for the Hubbard model, the whole cluster takes over this role in the CDW phase of TaSe$_2$. Consequently the Hubbard U is then the energy cost for double occupancy of one cluster orbital, and the hopping parameter t measures the energy gain associated with the hopping from one cluster to the next. Panel (c) illustrates the underlying idea in form of two sketched cluster orbitals. This picture is able to naturally explain why the crucial parameters U and W, the latter being proportional to the transfer integral t, are both much lower than in typical transition metal systems undergoing a Mott transition.

If the transfer integral t is associated with hopping from cluster to cluster, it is readily understood that the corresponding bandwidth W changes with temperature. Upon cooling the CDW amplitude grows (cf. Section 2.2), in other words, the star-of-David clusters shrink, so that the wavefunction overlap of neighboring clusters is reduced. The transfer integral thus becomes smaller, and with it the bandwidth W.

The temperature induced variation of the CDW is confirmed by the ARPES data, which clearly demonstrate that the CDW-induced changes are more pronounced at low temperatures, as a comparison of Panels (a) and (b) of Fig. 4.9 shows. Further evidence can be found in measurements of Ta $4f$ core levels presented in Ref. [Colonna05], which exhibit an increased energy separation at lower temperature.

In the *bulk* of 1T-TaSe$_2$, the reduction of W is apparently not sufficient to reach the critical threshold value of U/W necessary to trigger a Mott transition. At the *surface*, however, the case is different, and the photoemission measurements evidence a transition into an insulating state. One possible explanation is an enhancement of the CDW at the surface, where the topmost Se atoms benefit from a reduced coordination so that a lattice distortion is connected with a lower energy cost [Perfetti03]. Putting all pieces together, it can be summarized that a surface metal-insulator transition was observed by photoemission experiments, which is driven by a CDW-induced reduction of the bandwidth. This effect is able to modify the balance between the local Coulomb energy and the conduction bandwidth such that the surface of 1T-TaSe$_2$ is driven into a Mott insulating state when cooled below the transition temperature, whereas the bulk remains metallic down to the lowest investigated temperatures. The insulating state is confined to the surface and can therefore only be detected by surface-sensitive techniques such as photoelectron spectroscopy. The extent of the insulating surface zone seems to modestly grow with decreasing temperatures.

4.6 Conclusion and Outlook

It was already mentioned in the introduction of this chapter that the investigation of the 1T-TaSe$_2$ electronic structure by means of photoelectron spectroscopy is the subject of a considerable number of publications. It must be stated, however, that the CDW's influence on the electronic structure could not be resolved experimentally to a completely

satisfying extent. This is due to the fact that the spectral weight distribution is only weakly affected by the CDW potential — in contrast to the band dispersions, which are drastically deformed by the new periodicity of the superstructure. However, for a deep understanding of the interplay between Peierls and Mott physics, it would be desirable to get an experimental handle on the CDW-induced changes. An opportunity to extract the concealed changes lies in polarization-dependent photoemission experiments. In this way it can be utilized that the Ta $5d$ band is characterized by an even symmetry with respect to the ΓALM plane, since it is almost exclusively comprised out of even $d_{3z^2-r^2}$, $d_{x^2-y^2}$ and d_{xy} states. For a suitable choice of the light polarization, the photoemission matrix elements suppress the signal from the electronic structure generated by the intrinsic crystal potential. The remaining intensity should then highlight the weak changes provoked by the CDW potential. This technique was already successfully applied by Aiura and coworkers to $1T$-TaS$_{1.2}$Se$_{0.8}$ [Aiura03b]. Prospective preliminary results for $1T$-TaSe$_2$, obtained in a synchrotron experiment at Elettra in Trieste, Italy, show that it would be interesting to further pursue this idea in order to disentangle the effects of the intrinsic crystal potential, of the CDW potential, and of the electronic correlations leading to the metal-insulator transition.

5 Spin-Peierls Physics in the Titanium Oxyhalides

5.1 Motivation

After the discovery of high-T_c superconductivity by Bednorz and Müller in 1986 [Bednorz86] the interest in the RVB state as a possible explanation for this phenomenon revived. However, it was clear already at that time that the realization of the RVB state can only occur in a small region of phase space. For systems denied to adopt a Néel ordered ground state, there is a wide range of alternative behaviors, and RVB is certainly not the most obvious of these. In the search for the realization of the RVB state in nature, Beynon and Wilson examined the spin-1/2 Mott insulators TiOCl and TiOBr in 1993 [Beynon93]. Although they remained tentative in their conclusion, they considered the oxyhalides promising candidates for the RVB state for a series of reasons.

The basic requirement is of course the spin-1/2 configuration. As laid out in Section 2.4, the low spin is essential for the quantum spin liquid because of the amplified role of quantum fluctuations. In TiOCl and TiOBr the orbital momentum is quenched, just as in the other $3d$ transition metal compounds, and consequently their magnetic moment corresponds to the spin-only value of $S = 1/2$. In this respect, they are the counterparts of the d^9 cuprate high-T_c superconductors. Further arguments are connected with the basic crystal structure of these materials, which will be presented in the following section. The layered titanium oxyhalides are structurally low-dimensional, which is an important prerequisite for RVB, because this again favors quantum fluctuations. Moreover, the triangular arrangement of spins with almost equal Ti–Ti distances resembles the situation depicted in Fig. 2.13 with a geometric frustration of simple AFM order. Also the magnetic susceptibility measured in the group of Wilson [Wilson87, Maule88] fitted into the RVB picture. It showed a very flat dependency on temperature with no signs of a phase transition at low temperatures. This was interpreted by Beynon and Wilson as the Pauli paramagnetic behavior characteristic of the RVB state (cf. Section 2.4).

What made these systems even more attractive is the proximity to the metal-insulator transition, since — according to mean-field theory — the metallization of an RVB system is equivalent to the generation of superconductivity. Another interesting property of the titanium oxyhalides is the orbital degree of freedom. In contrast to the cuprates where the hole resides in the e_g orbitals, the t_{2g} manifold is occupied in the early transition metal compounds. These orbitals are much less Jahn-Teller active, and their near

degeneracy provides a rich variety of interesting physics. One can thus expect that, additional to the spin and lattice degrees of freedom, the orbital sector is involved as well.

The question if the RVB state is realized in the undoped oxyhalides can unambiguously be answered, as their ground state is clearly *not* of RVB nature. This was found in 2003 by Seidel *et al.* when they remeasured the magnetic susceptibility of the chloride [Seidel03]. They discovered two phase transitions, which were hardly pronounced and thus overseen in the data of Wilson *et al.* [Wilson87, Maule88], probably due to an imperfect sample quality. Seidel and co-workers interpreted this phenomenon as the signature of a spin-Peierls instability. Even if the scenario in TiOCl and TiOBr is not a conventional one, it will be shown in this thesis that the titanium oxyhalides nevertheless have to be regarded as spin-Peierls systems. Although not originally intended, Seidel *et al.* discovered a spin-Peierls system with record high transition temperatures of 67 K and 91 K. And as this instability was almost exclusively found in organic systems so far, TiOCl and TiOBr are the only inorganic spin-Peierls systems besides $CuGeO_3$. The spin-Peierls instability has very interesting properties as outlined in Section 2.3, and it has to be analyzed if in the oxyhalides interesting effects occur due to the orbital degree of freedom, which could possibly come into play. This aspect was not included in the theoretical model. Also the effects of a finite interchain coupling have to be examined for their consequences. Even if Seidel *et al.* were not able to find the desired RVB state in TiOCl, it can hardly be viewed as a failure to have uncovered the rich physics, that will be presented in the course of this chapter. It shall be stressed, however, that despite the obvious absence of the RVB state in the undoped compounds, the possibility remains that this state is preferred to the spin-Peierls order when the systems are sufficiently doped.

This chapter is organized as follows: After a brief introduction of the oxyhalides in their normal state at room temperature, the sample preparation and characterization will be presented. In the next section the unconventional spin-Peierls scenario with its two phase transitions will be illuminated. The determination of the electronic structure at room temperature by experimental and computational means is the central section of this chapter. Before concluding with the discussion of conducted and intended doping studies, it will be shown that it is possible to trigger an insulator-metal transition in TiOCl by applying external pressure, which strengthens the hope in the search for superconductivity in these compounds.

5.2 Normal State

The oxyhalides TiOCl and TiOBr are characterized by the trivalency of the Ti atom in a $3d^1$ configuration. Due to strongly pronounced correlation effects in the $3d$ transition metals, the odd number of electrons does not lead to a metallic state as it would be expected from simple Bloch theory. Conversely, the oxyhalides are Mott insulators, and op-

Table 5.1: *Structural parameters and atomic separations of TiOCl [van Smaalen06] and TiOBr [Schnering72] at room temperature. For the definitions of the Ti–Ti distances, see Fig. 5.2. Units in Å.*

|	Unit Cell			Ti–Ti Distance	
	a	b	c	Ti–Ti$_b$	Ti–Ti$_{abc}$
TiOCl	3.779	3.355	8.027	3.355	3.172
TiOBr	3.787	3.487	8.529	3.487	3.193

tical spectroscopy observes a charge gap of $\approx 2\,\text{eV}$ [Maule88, Rückamp05a, Kuntscher06].

As emphasized before, the details of the crystal structure are of fundamental importance for the competition of the different ground states of a spin-1/2 system. For instance, low dimensionality will weaken the tendency of the system to order antiferromagnetically as it favors quantum fluctuations over a static spin configuration. Also geometrical frustration is an important aspect, as it raises the probability for the establishment of an RVB state by complicating a simple Néel ordered or spin-Peierls distorted ground state.

The titanium oxyhalides are layered compounds, but not this structural two-dimensionality is the determining factor for the question which ground state is chosen by the system. It is rather the dimensionality of the electronic system, or more precisely, of the low lying electronic excitations. A central point is therefore what the strongest interaction paths are, as they can lower the effective dimensionality of the electronic system. Indeed, Seidel *et al.* found that the magnetic behavior of the chloride in the room temperature phase rather hints to a one-dimensional character [Seidel03]. Above approximately 130 K the paramagnetic susceptibility can be nicely described by a Bonner-Fisher behavior, characteristic for one-dimensional Heisenberg spin chains. Seidel and co-workers fitted this part of their susceptibility data to the Bonner-Fisher curve, in this way extracting a value of 660 K for the nearest neighbor exchange J of the Heisenberg Hamiltonian. The underlying reason for this one-dimensional nature will be put forward in the following detailed description of the room temperature crystal structure.

The structural determination of TiOCl was first accomplished by Schäfer and co-workers in 1958 [Schäfer58]. The oxyhalides TiOCl and TiOBr are both isostructural to the quasi-two-dimensional FeOCl, which crystallizes in the orthorhombic space group *Pmmn* (59) with $Z = 2$, i.e., a unit cell comprises two atoms of each sort. In Table 5.1 the lattice constants are summarized. One notices that they are slightly larger in the bromide, which of course results from the larger anion radii.

The structure can be described as consisting of buckled Ti-O bilayers that are sandwiched between two halogen sheets and repeat themselves along the crystallographic c axis. Two neighboring bilayers are shown in Fig. 5.1. They interact only weakly through van der Waals forces mediated by the halogen ions. The local symmetry of each Ti site is *mm2*, i.e., there exist two mirror planes perpendicular to the crystallographic a and b
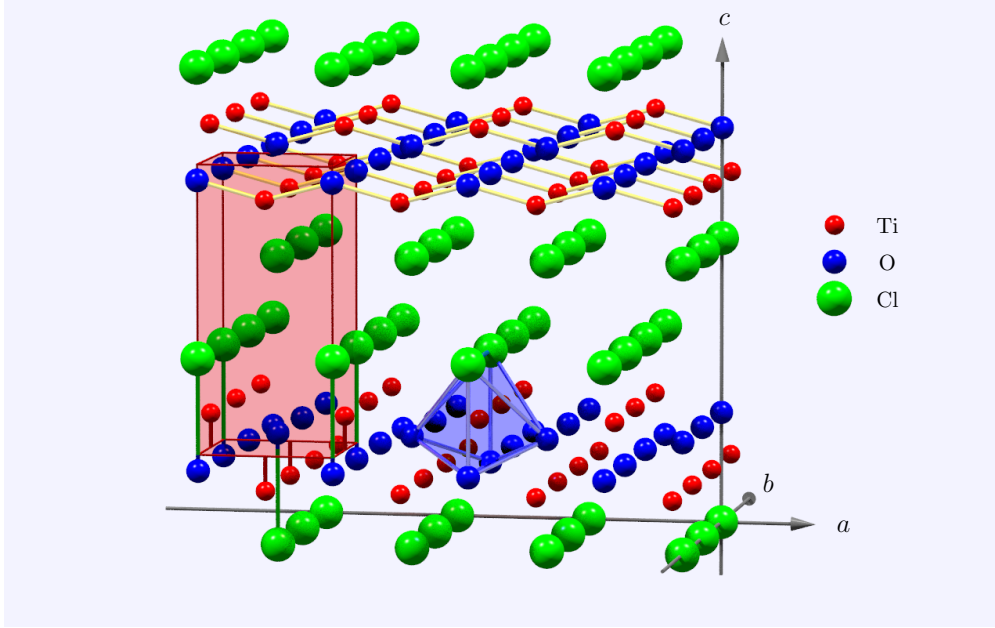
Figure 5.1: *FeOCl-type crystal structure of TiOCl and TiOBr. Yellow bonds emphasize the buckled Ti-O bilayers. A unit cell is highlighted in red together with the relative position of certain atoms with respect to its basal plane. The coordinating octahedron of a Ti ions, formed out of four O and two Cl ion, is indicated in blue.*

axes, respectively, and the c axis is a twofold rotation axis. Each Ti ion is surrounded by a distorted octahedron of four oxygen and two halogen ions, as indicated in the figure. These octahedra share corners along the a axis and edges along the b axis.

In Fig. 5.2, a view of the Ti ions in a single sandwich layer is shown, omitting the O and Cl ions for simplicity. The Ti ions are arranged in two rectangular arrays on different levels. Note that the distance Ti–Ti$_{abc}$ between two adjacent Ti ions of different levels is slightly shorter than the distance Ti–Ti$_b$ along the b axis on the same level, as listed in Table 5.1. The resulting triangular configuration of Ti sites is responsible for the geometrical frustration of a simple AFM or spin-Peierls order.

To answer the question of dimensionality, one has to take a look at the local environment of the relevant Ti ions, as the basis for the low lying excitations is mainly comprised of the Ti $3d$ electrons. The electronic structure is thus determined by the octahedral coordination of the Ti ion. The octahedral cages dictate the local coordinate system for the description of the Ti $3d$ orbitals: As indicated in Fig. 5.2, the z axis of the local coordinate system coincides with the a axis, and the x and y axis are rotated by 45° with respect to the b and c axes, so that they roughly point in the direction of the surrounding ligands.

The single $3d$ electron will reside in the t_{2g} triplet, as these orbitals point midway between the repelling ligands. The direct cation–cation overlap is promoted in the oxyhalides by the t_{2g} orbitals' orientation, in contrast to the late transition metal com-
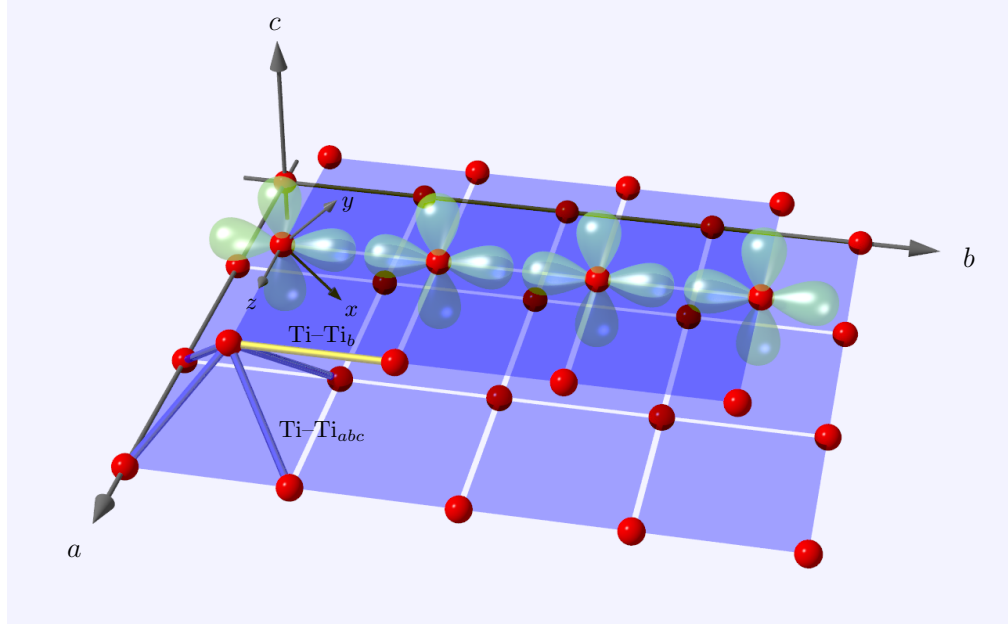
Figure 5.2: *Rectangular arrangement of Ti sites in two adjacent sheets parallel to the (a,b) plane. For simplicity O and Cl ions are not shown. The direct connection Ti–Ti$_b$ between two sites along the b direction (yellow) and the slightly shorter Ti–Ti$_{abc}$ connections (blue) are highlighted. Linear chains are formed along the b direction by Ti $3d_{xy}$ orbitals, indicated in green. Note that the local coordinate system (x,y,z) does not coincide with the global reference frame (a,b,c).*

pounds, where superexchange plays a larger role. The greater size at given valence of the titanium ion compared to a copper ion, for instance, intensifies this effect. As a further consequence of the orientational aspect, the t_{2g} electrons are generally less susceptible to Jahn-Teller distortions than the e_g subshell relevant for the late transition metal compounds. From this point of view, orbital degeneracy is generally more likely in the Ti d^1 systems than in the d^9 cuprate systems. However, one has to keep in mind that in TiOCl and TiOBr the coordinating octahedra are strongly distorted, so that a non-negligible splitting of the t_{2g} manifold can be expected. Indeed, LDA+U calculations identified the d_{xy} derived band as slightly split off from the bands with d_{xz} and d_{yz} character [Seidel03, Saha-Dasgupta04]. According to these calculations, the single Ti $3d$ electron will therefore occupy the d_{xy} orbitals, which point in the direction of the next Ti site along the crystallographic b direction. The resulting chains of overlapping orbitals are illustrated in Fig. 5.2. Note that the lobes perpendicular to the chain do not point at any of the neighboring atoms. From this, it is clear that the predominant hopping path will involve only the Ti sites along the one-dimensional chain direction.

Saha-Dasgupta *et al.* quantified this statement by means of a tight-binding downfolding procedure [Saha-Dasgupta04]. They showed that the transfer integral t is much larger along the b direction than, for example, along the slightly shorter connection of two Ti sites in adjacent Ti-O sheets. However, the latter hopping parameter, which
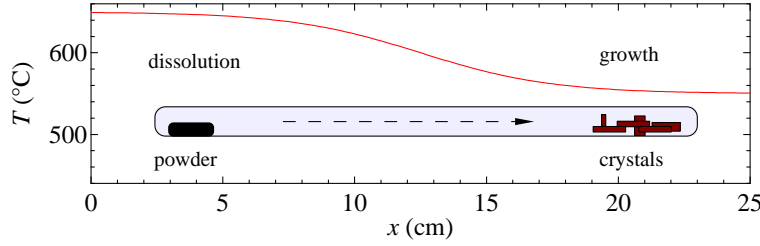
Figure 5.3: *Sketch of the chemical vapor transport setup. A quartz tube with the reactants at one end is exposed to the temperature gradient of a multi-zone furnace.*

connects sites on different chains, is nonzero and therefore responsible for a coupling between the chains. In Section 5.4.3 it will be laid out, that this coupling can be the origin of interesting physics. The experimental determination of the dimensionality of TiOCl and TiOBr is one of the central points treated in Section 5.5.

5.3 Sample Preparation and Characterization

Single crystals of TiOCl were grown by the chemical vapor transport method [Schäfer62, Nitzsche67], as sketched in Fig. 5.3. A closed quartz tube is brought into a temperature gradient with the reactants at the hot end. TiOCl single crystals will then grow at the colder end of the quartz tube. The origin of the transport lies in the dependence of the chemical equilibrium on temperature. In the hotter dissolution zone, the reactants will preferably go into the gas phase, whereas in the growth region, the equilibrium is shifted to the side of the solid phase. However, one has to keep in mind that this is a reversible process — dissolution and growth will always take place in both zones. In the pressure regime of several bar, which is a realistic pressure for the typical amount of reactants in the quartz tube, the transport is governed by thermal convection. This is aided by a slight inclination of the quartz ampoule. In the growth zone, the gas phase is supersaturated and spontaneous nucleation will set in. Statistical density fluctuations lead to aggregation, but the aggregates will in general dissolve again. Only when they have reached a certain size they are energetically stable. Then the resulting seeds can grow in the supersaturated ambience and develop into macroscopic crystals. The temperature gradient and the concentrations have to be chosen such that on one hand, the probability of seed creation stays low enough for an unperturbed growth of separated single crystals, and on the other hand, the growth rate does not become too small.

Based on the procedure described by Schäfer *et al.* [Schäfer58], the parameters were optimized over a period of more than two years. In this process, approximately 40 batches of TiOCl crystals were produced from different reactants and with different parameters. Initially TiOCl was synthesized from $TiCl_3$ and TiO_2 according to the reaction equation

$$2TiCl_3 + TiO_2 \rightleftharpoons 2TiOCl + TiCl_4. \tag{5.1}$$

Table 5.2: *Durations and temperature gradients of the TiOCl crystal growth phases.*

| Duration	Temperature (°C)	
	Dissolution Zone	Growth Zone
4 h	450	800
3 d	650	550
1 d	300	550
3 d	650	550
1 d	300	550
3 d	650	550
1 d	300	550
14 d	650	550
4 h	300	550

However, it was found that sightly better results can be achieved using the starting materials of the reaction

$$\text{TiCl}_4 + \text{Ti} + 2\text{TiO}_2 \rightleftharpoons 4\text{TiOCl}, \qquad (5.2)$$
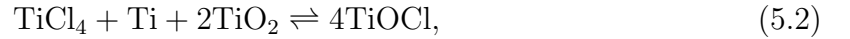
with the constraint that the liquid TiCl_4 is more complicated to handle than the TiCl_3 powder.

The disadvantage of the chemical reaction described in Equation 5.1 is that besides TiOCl also TiCl_4 is produced, which is a very reactive fluid at room temperature. The experience was often made that the TiOCl crystals were wetted with a thin film of TiCl_4. At the first contact with air this film heavily reacted and thus spoiled the surface of the TiOCl crystals.

In the following the crystal growth procedure will be described, giving a detailed account of the parameters that resulted from the optimization process: Quartz ampoules of 180 mm length and with an inner diameter of 12 mm were degassed for several hours at 1000 °C. They were then filled with the reactants TiCl_4, Ti, and TiO_2 (baked beforehand under vacuum at 300°C for several hours) in an Argon glove box and sealed under vacuum ($p < 10^{-4}$ mbar). TiCl_4, whose boiling point is at 135 °C, acts as a transport agent for this reaction. A slight deviation of -5% to -10% of the TiCl_4 mass from the stoichiometric value was used in order to slow down the transport and thus improve the crystal quality. The growth regions of the ampoules were then baked free of residues of the filling process by exposing them to a temperature of 800 °C in a three-zone or ten-zone furnace for several hours, while keeping the dissolution region at a temperature of 450 °C. This treatment was followed by a phase where the direction of the temperature gradient was repeatedly switched forth and back. Periods with a "forward" temperature gradient of 650°C at the dissolution zone to 550°C at the growth zone were followed by
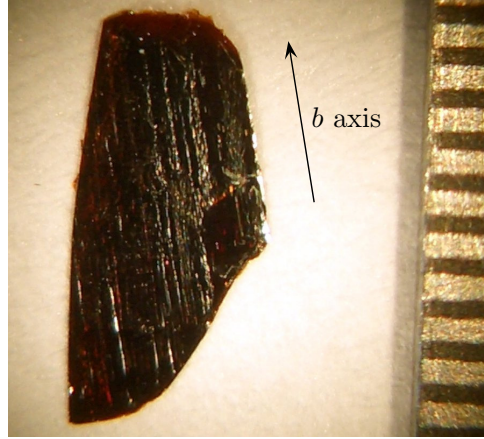
Figure 5.4: *TiOCl crystal grown with the CVT method. The direction of the b axis is indicated. The scale units on the right hand side correspond to .5 mm.*

an inverse "backward" temperature gradient at a lower base temperature. The aim was to dissolve the smallest of the developing crystals in each cycle, so that only the larger ones survive. Instead of many small crystals, that will eventually grow together in a single large structure, separated crystals are generated by this procedure, that can grow without disturbing each other. This is followed by a stage of transport with a "forward" temperature gradient of approximately two weeks. Before the ampoules are taken out of the furnace, the gradient is switched again to the "backward" direction, so that remaining reactants in the gas phase condense in the dissolution zone. The durations and temperature profiles of the different stages described above are summarized in Table 5.2.

Figure 5.4 shows a photography of a TiOCl crystal that was obtained by this method. Typical crystal dimensions are $4\,\text{mm} \times 2\,\text{mm} \times 0.1\,\text{mm}$. Very thin TiOCl crystals have a red color, whereas thicker ones appear black. The red color can be explained by the optical gap of $\approx 2\,\text{eV}$ [Maule88, Rückamp05a, Kuntscher06].

TiOBr samples were courteously supplied by Prof. van Smaalen, synthesized in an analogous manner as described in Ref. [Palatinus05].

The TiOCl crystals were characterized with various experimental techniques, of which XRD, scanning electron microscopy (SEM), and energy dispersive x-ray analysis (EDX) will only be listed. The results of Laue diffraction and dielectric measurements will be briefly presented. Laue diffraction is a very helpful instrument to judge the crystal quality of TiOCl crystals. In Fig. 5.5 (a) a typical Laue diffractogram of a relatively good crystal is shown. From the Laue pattern the orientation of the crystal can be deduced. The directions of the crystallographic axes a and b are parallel to the two orthogonal lines of the $(1, 0, l)$ and $(0, 1, l)$ reflections, respectively. They can be discriminated easily using the line of the $(1, 1, l)$ reflections, which encloses an angle $\theta = \arctan b/a = 41.6°$ with the line of the $(0, 1, l)$ reflections. In many cases one can also infer the orientation of the crystal just by eye. Often the crystals possess a needle-like shape, with the b direction
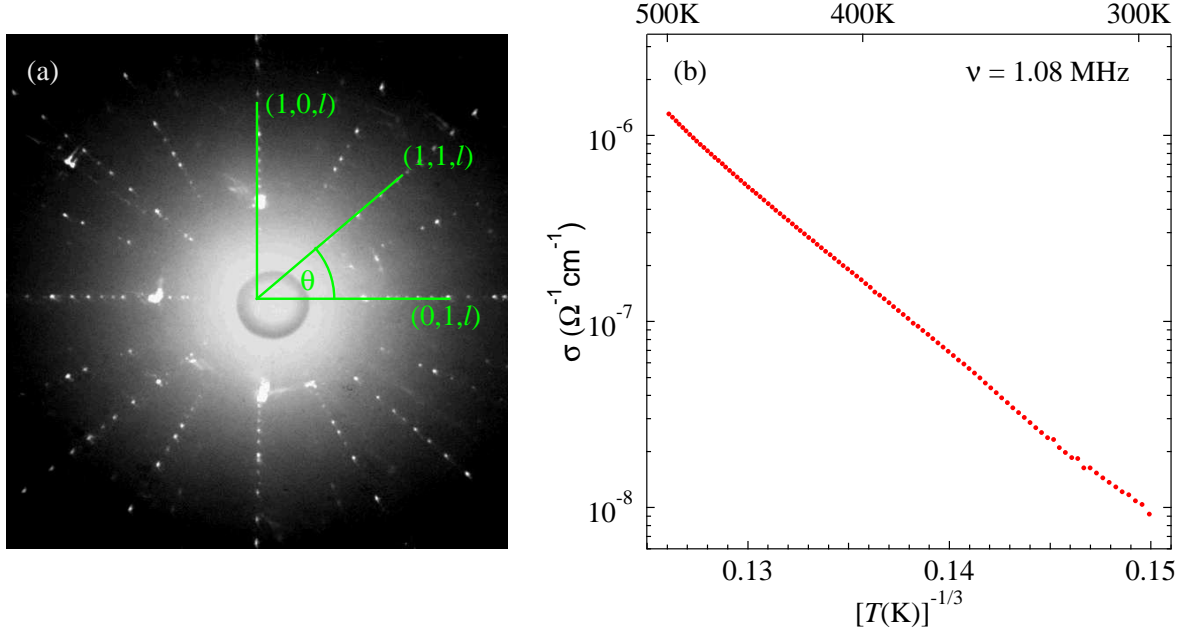
Figure 5.5: *(a) Laue photography of a TiOCl crystal ($U_A = 25\,kV$). (b) Temperature dependence of the conductivity of a TiOCl single crystal measured by dielectric spectroscopy at a frequency of 1.08 MHz. The conductivity is plotted logarithmically vs. $T^{-1/3}$.*

parallel to the needle axis. Another indicator of the crystal orientation is the texturing of the surface parallel to the b axis that can frequently be observed (cf. Fig. 5.4).

DC transport measurements were carried out by Dr. Obermeier at Prof. Horn's chair. Due to the highly insulating character of TiOCl, only a lower bound of $10^6\,\Omega$cm for the resistivity along the b axis at room temperature could be estimated. More success in determining the charge transport properties of TiOCl was achieved by dielectric measurements, performed by Dr. Lunkenheimer at Prof. Loidl's chair. The conductivity at 1.08 MHz, which should not deviate substantially from the dc conductivity, is displayed in Fig. 5.5 (b). In this graph, the conductivity is plotted logarithmically vs. $T^{-1/3}$. The resulting linear curve is indicative for variable range hopping [Madelung78], a mechanism of charge transport via localized impurity states in a two-dimensional insulator. This model predicts a conductivity proportional to $\exp[-(T_0/T)^{1/3}]$, where T_0 is a constant containing basically the density of impurity states at the chemical potential. Note, however, that fitting the conductivity with $\exp[-(T/T_0)^{1/4}]$, corresponding to variable range hopping in three dimensions, matches comparably well. The temperature range of 300 K to 500 K covered by the measurement does not allow to determine the concrete nature of charge transport. The absolute value of $\approx 10^8\,\Omega$cm for the resistivity at 300 K is consistent with the estimate of the dc measurements.

Furthermore, the TiOCl crystals' high quality was demonstrated by measurements of the magnetic susceptibility, as will be described in detail in the following section.

5.4 The Spin-Peierls Scenario

5.4.1 Phase Transitions

Evidence from the Magnetic Susceptibility: Two Phase Transitions

In 2003 Seidel *et al.* discovered two successive phase transitions when they measured the magnetic susceptibility of TiOCl. Figure 5.6 shows the result of a measurement performed by Dr. Klemm with a SQUID magnetometer on TiOCl crystals grown in Augsburg [Hoinkis05].

In Panel (a) the susceptibility data are plotted versus temperature in the range from 2 K to 400 K. The magnetic behavior can be outlined as follows: In the high temperature range the susceptibility displays a rather flat and isotropic behavior that can be described by the Bonner-Fisher curve of a one-dimensional Heisenberg spin chain. A deviation from this smooth progression is clearly noticeable at $T_{c_2} = 91$ K, where a kink appears in the susceptibility. Even more pronounced is the anomaly at $T_{c_1} = 67$ K, that expresses itself as a sharp drop of the magnetization.

Panel (b) shows a blow-up of the data in a reduced temperature region around the transition temperatures. The cooling and heating curves are plotted, revealing the nature of the anomaly at T_{c_1}: The thermal hysteresis of ≈ 1.5 K is indicative of a first-order phase transition. Directly below T_{c_1} the curve is flat, until a Curie tail caused by magnetic impurities begins to dominate the susceptibility at lower temperatures. Below 60 K the curve can be fitted nicely with a Curie term $\chi_{\text{Curie}} = C/T$ and a constant offset χ_0, as shown in Panel (a). After subtraction of χ_{Curie}, the susceptibility is basically temperature independent below T_{c_1}.

The concentration of paramagnetic impurities can be estimated using the fit of the Curie tail. Under the assumption of $S = 1/2$ defects (e.g., Ti^{3+} in structural defects), a value of 0.3 % is obtained. This is an upper bound for the impurity concentration, as the Curie tail is a measure of the concentration of unpaired spins and any defects or impurities are likely to create more than one unpaired spin. In the literature only Ref. [Kataev03] gives a number for the impurity concentration in TiOCl, which is higher than the above result by a factor of two. Moreover, the constant offset χ_0 of the displayed data is a factor 2 to 4 smaller compared to other results published in the literature [Seidel03, Kataev03, Rückamp05a]. The small concentration of paramagnetic impurities and the low constant offset, together with the hysteretic behavior of $\chi(T)$ at T_{c_1}, which was not found in the published susceptibility data so far, can be taken as further arguments for the excellent quality of the TiOCl crystals.

On the basis of the susceptibility data, Seidel *et al.* interpreted TiOCl as a non canonical spin-Peierls system. The drop of the susceptibility at T_{c_1} was interpreted as the opening of a spin gap, connected with a dimerization of Ti sites and formation of singlet pairs. However, for a canonical spin-Peierls system only one phase transition is expected. Furthermore, this transition should be of second order. This is in clear contrast to the
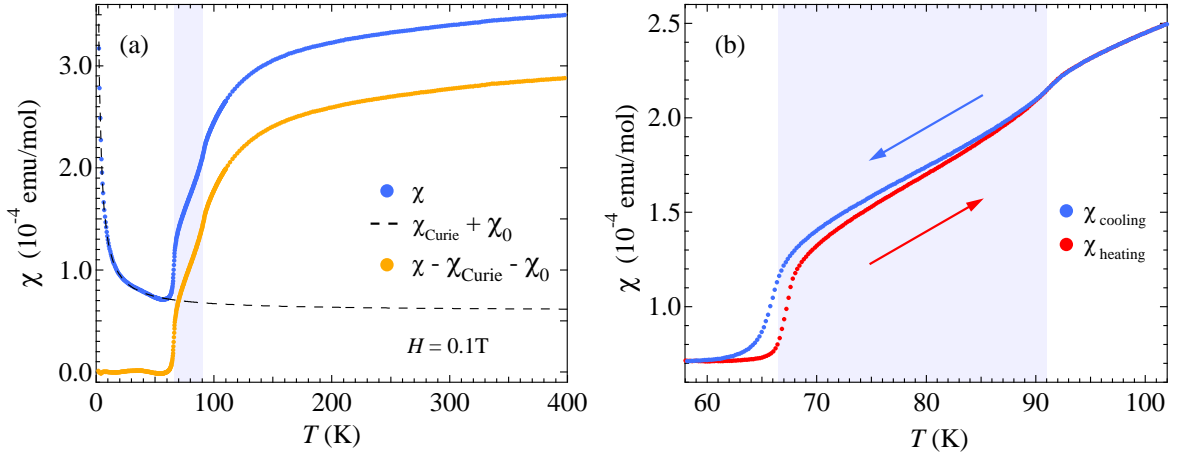
Figure 5.6: *Temperature dependence of the magnetic susceptibility of TiOCl measured by SQUID magnetometry. The three phases are highlighted by different background colors. (a) Raw data and data after subtraction of a constant offset and a Curie contribution. (b) Cooling and heating curve without Curie subtraction in a reduced temperature range.*

susceptibility data, which exhibit a first-order phase transition at T_{c_1} and a second-order phase transition at T_{c_2}. The natural question if TiOCl and TiOBr can be classified as spin-Peierls systems in spite of these inconsistencies with a conventional spin-Peierls scenario was answered by x-ray diffraction studies: They demonstrated that the anomaly at T_{c_1} must indeed be interpreted as a spin-Peierls transition, yet one of non-canonical nature. This was achieved by finding a dimerization of the Ti sites that accompanies a spin-Peierls transition, as will be laid out in the following section. The nature of the second phase transition observed, which could not be interpreted by the susceptibility measurement alone and was speculatively attributed to orbital ordering [Imai03], was also unravelled by x-ray measurements: In Section 5.4.3 it will be shown that the intermediate phase between T_{c_1} and T_{c_2} is characterized by an incommensurate modulation of the atomic positions. Coming from the high temperature regime, this incommensurability sets in at T_{c_2}, before the modulation locks in a periodicity commensurate with the crystal lattice below T_{c_1}.

The magnetic susceptibility of TiOBr displays a behavior very similar to that of TiOCl [Lemmens05]. Also two phase transitions are observed. They are interpreted as spin-Peierls transitions of the same nature as those described above in the case of TiOCl. Although the focus in the following sections lies on the compound TiOCl, it will become clear that the low temperature and the intermediate state of TiOBr are analogous to TiOCl, however, with lower transition temperatures. Table 5.3 compares the transition temperatures and exchange constants of the two compounds. It is worthy to repeat that the energy scales of TiOCl are the highest of any known inorganic or organic spin-Peierls compound.

Table 5.3: *Transition temperatures and nearest neighbor exchange constants of TiOCl [Hemberger05, Seidel03] and TiOBr [Rückamp05a].*

	T_{c_2}	T_{c_2}	J
TiOCl	67 K	91 K	660 K
TiOBr	28 K	48 K	375 K

Evidence from Heat Capacity Measurements: The Role of Fluctuations

More information about the two phase transitions comes from measurements of the heat capacity of TiOCl [Hemberger05]. All the microscopic degrees of freedom that come into consideration as competitors on going through the phase transitions can contribute to the specific heat. For TiOCl and TiOBr, the lattice, magnetic, and orbital degrees of freedom have to be named in this context.

Experiments with a commercial measurement system (PPMS) manufactured by Quantum Design were performed by Dr. Hemberger at Prof. Loidl's chair. The temperature range from 2 K to 300 K was covered. In Fig. 5.7 the results of this investigation are displayed. Panel (a) shows the specific heat of TiOCl, plotted as C/T versus T. The heat capacity is characteristic for a three-dimensional solid with a Debye temperature of approximately 200 K. Superimposed, the footprints of the structural instabilities are visible at T_{c_1} and T_{c_2}. The effects of the phase transitions on the specific heat are remarkably weak and are almost lost under the large phonon-derived heat capacity contributions. It is clear that the entropy covered by the two anomalies is comparably small. Applying an external magnetic field of up to 5 T did not lead to any observable effect at temperatures considerably higher than 5 K. The moderate magnetic fields used here neither shift the transition temperatures, nor do they seem to affect the entropies involved in the phase transitions. This is not surprising given that the energy of a 5 T magnetic field is of order $5\,\text{T} \times \mu_B \approx 3\,\text{K}$, which is negligibly small compared to the intrinsic magnetic energy scale of TiOCl as estimated from $T_{c_{1,2}}$ or the exchange constant J. The mean-field critical field for example, which is necessary to destroy the spin-Peierls order, was stated in Section 2.3 to be $\mu_B H_c \approx 0.75\,k_B T_c$.

In order to analyze the nature of the detected anomalies in terms of first- or second-order phase transitions, heating/cooling cycles across the phase transitions were performed. As the experimental setup utilizes a relaxation method, each data point is related to the average over a temperature interval above the initially stabilized temperature rather than to an exact temperature [Lashley03]. This means that for the cooling sequence the temperature is decreased between the data acquisition and increased during the acquisition process itself. Thus, in the case of hysteretic, i.e., first-order behavior, the actual transition, together with the corresponding release of latent heat, is fully captured only in the heating branch of the measuring sequence. Around T_{c_1} a significant difference between heating and cooling can be detected, as shown in Fig. 5.7 (b).
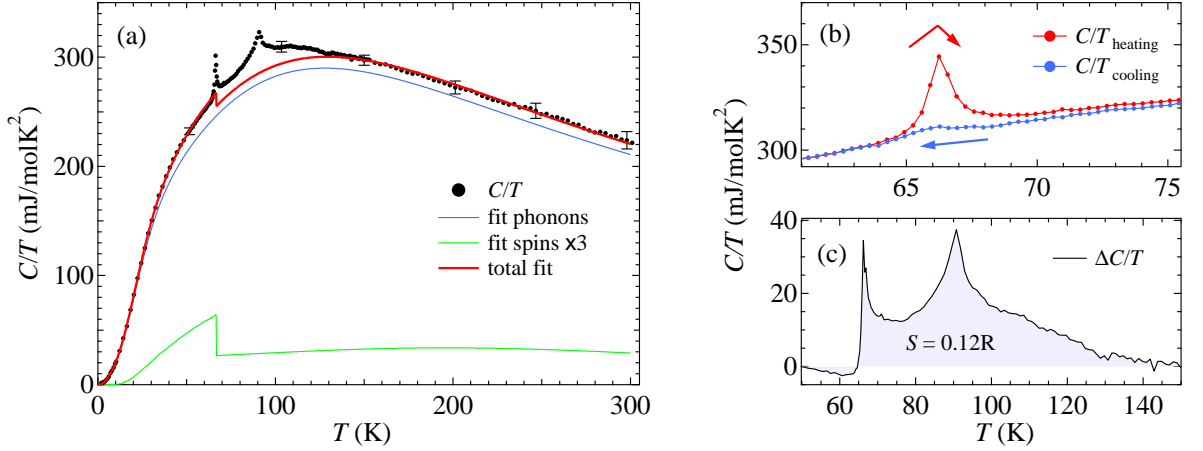
Figure 5.7: *Heat capacity of TiOCl, plotted as C/T versus T. (a) Experimental data and fit of specific heat, decomposed in spin- and phonon contributions. The vertical bars indicate experimental uncertainties and reveal the scatter of C/T in different measuring cycles with different temperature stimuli on different samples. (b) Temperature region around T_{c_1} remeasured with a reduced relaxation amplitude of $\delta T = 0.5\,K$ in a heating and subsequent cooling cycle. (c) Difference between calculated and measured heat capacities. The area under the curve corresponds to the released entropy.*

This again points to a first-order phase transition, in accordance with the susceptibility results. No such feature could be found for the upper instability at T_{c_2}.

In the following analysis, the experimental data will be fitted with a theoretical model consisting of two parts: A phonon-derived and a spin-derived component. The latter one is dominated by the phonon contribution for all temperatures. Nevertheless, a straightforward analysis of the thermal properties of TiOCl is possible. The spin part is split in two temperature regimes: Above T_{c_1} it is modelled by a Bonner-Fisher type of behavior taking into account an exchange coupling $J = 660\,\text{K}$; for the low-temperature regime, i.e., below the spin-Peierls transition at T_{c_1}, the expected exponential decrease of the spin part of the heat capacity is simulated according to a BCS-like mean-field treatment [Mühlschlegel59] with an activated behavior and an energy gap $2\Delta = 3.52\,k_{\text{B}}T_{c_1} = 236\,\text{K}$. These two regimes were connected by a heat capacity jump of 1.43 times the contribution of the spin chain directly at T_{c_1}, as described in Section 2.3. The spin-derived heat capacity, plotted in Fig. 5.7 (a), is thus modelled without any free parameter. It is clear, that this can only be a very rough analysis, specifically having in mind that the actual gap in TiOCl seems to be much larger. It will be described in Section 5.4.4 that the spin gap was estimated as $2\Delta \approx 430\,\text{K}$ by means of NMR measurements [Imai03]. As another shortcoming of the above description, the transition is actually of first order. The disregard of these experimental facts gives an underestimation of the jump height of the magnetic specific heat at the spin-Peierls transition and a decay too broad below, leading indeed to observable differences between the measured data and the calculation closely below T_{c_1}. However, the overall entropy balance is not affected by the shortcomings of this simple model.

The phonon system was fitted assuming one Debye and two Einstein-type contributions, yielding a total of five free parameters, namely, the mean Debye (Θ_D) and two Einstein temperatures ($\Theta_{E_{1,2}}$), and the ratio of Debye to Einstein modes $R_{D/E}$, as well as the ratio between the Einstein modes R_{E_1/E_2}. The number of degrees of freedom, which of course should be nine per formula unit of TiOCl, was kept fixed. The experimentally determined heat-capacity values for $T < 65\,\mathrm{K}$ and $T > 130\,\mathrm{K}$ were used for the fit of the heat capacity, and the parameter-free spin contributions were included. The total heat capacity, spin, and phonon contributions are plotted in Fig. 5.7 (a). Despite the oversimplifications mentioned, the model describes the experimental heat capacity astonishingly well. The parameters as determined by the best fit seem to be realistic: The characteristic temperatures, $\Theta_D = 188\,\mathrm{K}$, $\Theta_{E_1} = 352\,\mathrm{K}$, and $\Theta_{E_2} = 614\,\mathrm{K}$, with the ratios $R_{D/E} = 0.30$ and $R_{E_1/E_2} = 0.51$ determining the relative weight of Debye and Einstein modes, are reliable keeping in mind that the optical-phonon modes in TiOCl range from approximately $100\,\mathrm{K}$ to $700\,\mathrm{K}$, with dominant modes close to the values obtained for $\Theta_{E_{1,2}}$ in References [Caimi04, Lemmens04]. Comparing the model heat capacity to the measured one in Fig. 5.7, good agreement is found for the smooth temperature evolution at low ($T < T_{c_1}$) and high ($T > T_{c_2}$) temperatures. As clearly seen, the main deviations arise in the temperature region between the two instabilities. The good agreement concerning the smooth part of the heat capacity may seem surprising in the light of this simplified model. On the other hand, the phonon part is reasonably close to a realistic description involving the true phonon spectrum, and the spin part of the heat capacity bears only a small weight. This model can therefore be regarded as a reliable estimate of the regular part of the specific heat and the anomalous contribution due to the phase transitions at T_{c_1} and T_{c_2} can be separated out.

Panel (c) of Fig. 5.7 displays this extra heat capacity in a limited temperature range from $50\,\mathrm{K}$ to $150\,\mathrm{K}$. The integral over this region gives an estimate of the entropy ΔS being released when going through both transitions. ΔS is with $0.12R$ ($\pm 0.02R$) vanishingly small compared to $R\ln 2$ expected for a spin-1/2 system or an orbital doubly degenerate state. In the present case even a $R\ln 3$ contribution could be expected for an order-disorder transition of the degenerate orbitals within the t_{2g} triplet. The small value of the entropy change suggests that the orbital degrees of freedom do not play a part in the phase transitions in addition to the considered lattice and spin contributions. Comparing the narrow peak at T_{c_1} with the anomaly at T_{c_2}, it can be seen that the larger fraction of the entropy is covered under the latter instability. As the entropy measures the degree of disorder in a system, this experimental observation shows that the amount of order that is created upon cooling through T_{c_2} outweighs the corresponding amount at T_{c_1}. The origin of this behavior cannot be understood at this point, as the structural changes that accompany the phase transitions were not discussed yet. It will become clear in the following sections, however, that the periodic lattice distortion connected with a spin-Peierls transition sets in at T_{c_2}, which explains the large entropy change. At T_{c_1}, where the periodicity changes from an incommensurate to a commensurate value, the arising order is obviously relatively small.

As an interesting result of this investigation, the area under the curve $\Delta C/T$ in Panel (c) extends up to considerably higher temperatures. This is a manifestation of the fact that a great portion of the entropy is not released until much higher temperatures than T_{c_2} are reached. In this temperature regime, apparently a form of short-range order is maintained. The occurrence of a fluctuation regime in the titanium oxyhalides is not surprising, having in mind that quantum fluctuations are especially important in quasi-one-dimensional systems and in systems with spin-1/2.

This experimental finding is in line with nuclear magnetic resonance (NMR) and ESR measurements [Imai03, Kataev03], which exhibit also fluctuation effects up to 135 K. A decrease of low frequency spin excitations by two orders of magnitude between 135 K and T_{c_2} lead Imai *et al.* to interpret this temperature interval as a pseudogap regime. In the ESR data the suppression of magnetic excitations is expressed in form of a diminished linewidth. Also from Raman and infrared spectroscopy indications of a fluctuation regime of TiOCl were reported [Lemmens04, Caimi04]. Lemmens *et al.* notice a softening of phonon modes in this temperature regime. The infrared spectra of Caimi and co-workers display a narrowing of phonon modes at low temperatures that can be explained by a suppression of spin excitations due to the forming of spin dimers. Also the asymmetric shape of phonon modes is lost when this process sets in. Again the temperature borderline of these changes is not given by $T_{c_{1,2}}$, but is rather connected to the higher temperature scale of the fluctuation regime.

A further fingerprint of fluctuations was observed in an EXAFS experiment, carried out by Dr. Pfalzer at the ANKA–XAS beamline in Karlsruhe. From Ti K-edge spectra taken at various temperatures in the range from 15 K to 300 K it can be concluded that the short-range symmetry of the Ti sites' environment remains distorted *above* the pase transitions [Pfalzer05]. The signatures of short-range structural distortions, so to say spin-Peierls fluctuations, were found even up to room temperature.

From the results presented so far, it is evident that the lattice degrees of freedom plays an important role for the described fluctuations. However, one cannot decide on the precise microscopic nature of the fluctuations from these measurements alone; specifically the question to what extent the orbital degree of freedom is involved cannot be answered. Orbital fluctuations were at least considered compatible with observations of Raman scattering [Lemmens04] and with the results of density-functional calculations [Saha-Dasgupta04]. On the other hand, recently Rückamp and co-workers [Rückamp05a] concluded from cluster calculations that the orbital ground state is determined by a crystal-field splitting of approximately 0.25 eV, stabilizing the occupation of the d_{xy} levels[1] and thus strongly suppressing orbital fluctuations in the examined temperature range. This issue will be examined in detail in Section 5.5.3, where first experimental information that confirm the predictions of Rückamp *et al.* is presented.

---

[1]Note that Rückamp *et al.* choose the crystallographic axes as a basis for the local coordinate system, instead of orienting it along the axes of the TiO_4Cl_2 octahedron, as it is practiced widely in the literature and in this thesis. In Rückamp's notation the $d_{x^2-y^2}$ orbitals are occupied in the ground state.
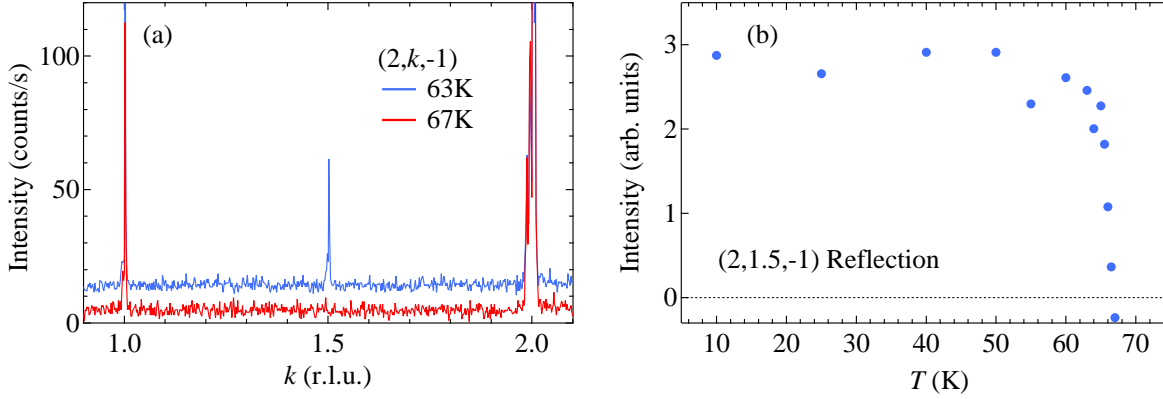
Figure 5.8: $(2, 1.5, -1)$ *superlattice reflection of TiOCl observed by x-ray diffraction. (a) Scan along the* $(2, k, -1)$ *line in reciprocal space slightly below and above* T_{c_1}. *The* $T = 63\,K$ *data are shifted by 10 counts/s for clarity. (b) Temperature dependence of the integrated intensity of the* $(2, 1.5, -1)$ *reflection. At* $T = 67\,K$ *the intensity was determined as less than zero (zero within standard uncertainty).*

5.4.2 Spin-Peierls Phase

Even though the suppression of spin fluctuations in the low temperature phase corroborates a spin-Peierls scenario in the oxyhalides, it must be clearly stated that the occurrence of a first-order phase transition followed by a second instability stands in the way of interpreting TiOCl and TiOBr as conventional spin-Peierls systems. It was the success of x-ray experiments to give doubtless evidence for the spin-Peierls nature of these compounds. In a collaboration with Prof. van Smaalen, x-ray diffraction studies were carried out on TiOCl single crystals, revealing the lattice dimerization that accompanies the formation of spin singlets [Shaz05].

The experiments were performed by Dr. Shaz with synchrotron radiation at beamline D3 of Hasylab (DESY, Hamburg) employing monochromatized radiation of wavelength $0.5000\,\text{Å}$. A single crystal of dimensions $0.05 \times 0.11 \times 0.01\,\text{mm}^3$ was mounted on a carbon fiber attached to a closed-cycle helium cryostat on a four-circle diffractometer. X-ray diffraction was measured by a point detector.

In a first experiment, scans in reciprocal space were performed at $T = 10\,\text{K}$ along various high symmetry lines. Superlattice reflections were only found at $(h, k + 1/2, l)$ positions, indicating a doubling of the unit cell along b. A few of the strongest superlattice reflections were selected for temperature-dependent measurements. The scans established that the relative positions of these reflections are independent of temperature. Figure 5.8 (a) displays scans along the $(2, k, -l)$ line, where the appearance of a superstructure below T_{c_1} can clearly be seen.

The integrated intensities of the superlattice reflections were found to be independent of temperature at low temperatures, but then they dropped suddenly to zero at $67\,\text{K}$, as it is shown for the $(2, 1.5, -1)$ reflection in Fig. 5.8 (b).

In order to perform structure refinements, the integrated intensities of all experi-

Table 5.4: *Structural data of TiOCl determined by single crystal XRD in the low temperature phase and at room temperature. Crystallographically independent atoms are labelled with arabic numbers.*

		$T = 10\,\mathrm{K}$				$T = 395\,\mathrm{K}$		
space group		$P2_1/m$				$Pmmn$		
cell parameters (Å)	a	3.783			a	3.779		
	b	6.683			b	3.355		
	c	8.031			c	8.027		
symmetry operators		x	y	z		x	y	z
		$\frac{1}{2}+x$	$\frac{3}{4}-y$	$-z$		$\frac{1}{2}+x$	$\frac{1}{2}-y$	$-z$
		$\frac{1}{2}-x$	$\frac{3}{4}-y$	$-z$		$\frac{1}{2}-x$	$\frac{1}{2}+y$	$-z$
		$-x$	y	z		$-x$	$-y$	z
						$\frac{1}{2}-x$	$\frac{1}{2}-y$	$-z$
						$-x$	y	z
						x	$-y$	z
						$\frac{1}{2}+x$	$\frac{1}{2}+y$	$-z$
atomic coordinates	Ti1	0.000	0.257	0.123	Ti	0.000	0.500	0.119
(fractions of unit cell)	Ti2	0.000	0.743	0.117	O	0.000	0.000	-0.055
	O1	0.000	0.004	-0.054	Cl	0.000	0.000	0.332
	O2	0.000	0.496	-0.061				
	Cl1	0.000	-0.002	0.330				
	Cl2	0.000	0.502	0.338				

mentally accessible Bragg reflections were measured at $T = 10\,\mathrm{K}$. The best fit to the diffraction data was obtained for a supercell with monoclinic symmetry and space group $P2_1/m$. A fit to a completely different structure model with acentric orthorhombic symmetry converged with only marginally smaller reliability, but involves three crystallographically independent Ti and Cl sites. This contradicts the NMR observation of only two inequivalent Ti and Cl sites below T_{c_1} [Imai03] and can therefore be discarded in favor of the structure with $P2_1/m$ symmetry. This model correctly predicts two crystallographically independent Ti and Cl sites. The structural data of the low temperature state according to this model are listed in Tab. 5.4 together with those for the room temperature structure.

The point group in the low temperature phase contains only the reflection in the (b,c) mirror plane, whereas the (a,c) mirror plane and the twofold rotation around c are lost.
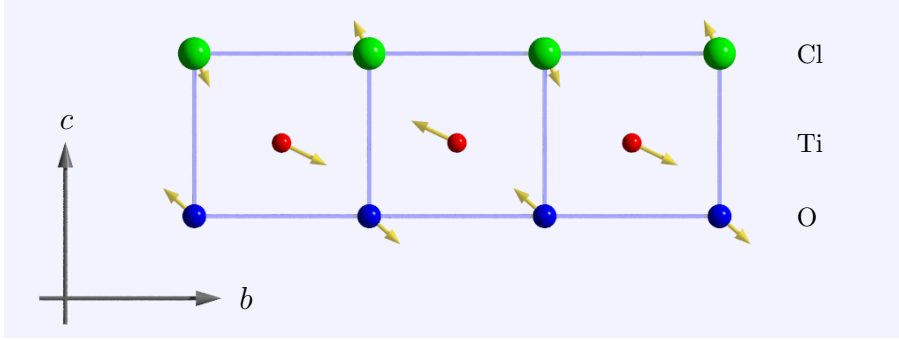
Figure 5.9: *Lattice distortion within a single ribbon in the spin-Peierls state of TiOCl. Arrows indicate the atomic displacements, which are exaggerated by a factor of 20.*

One ribbon parallel to b contains the six crystallographically independent atoms, all of which are in the mirror plane. Accordingly, the displacements of the atoms are restricted to the (b,c) plane. Such a ribbon is displayed in Fig. 5.9 with arrows indicating the shifts of the atomic positions. The pattern of displacements clearly shows a dimerization of the chain of Ti atoms, while the displacements of O and Cl atoms are such as to minimize the elastic strain of the structure. This interpretation is supported by comparing the interatomic distances in the superstructure and the basic structure. The largest variation of $0.18\,\text{Å}$ is found for the alternating distances on the Ti chains along b, indicating the formation of Ti–Ti pairs on these chains. The shortest Ti–Ti distance is between chains, but its variation in the superstructure is much less than the variation of distances along the chains, thus supporting the model of pair building on the chains as opposed to the formation of singlet pairs between electrons on neighboring chains. The variation of Ti–O distances $(0.049\,\text{Å})$ and of Ti–Cl distances $(0.024\,\text{Å})$ are much smaller than the variation of Ti–Ti distances along the chains, showing that the dimerization is indeed triggered by the magnetic exchange along b. In a recent publication Schönleber *et al.* provide a simple argument why the displacements of the Ti sites are not simply parallel to the **b** axis [Schönleber06]: This kind of displacement would lead to an unfavorable variation of Ti–O bonds of *neighboring* ribbons. This is resolved by the introduction of a component along the **c** axis, such that Ti and O displacements in *neighboring* ribbons are almost parallel and the corresponding Ti–O bonds do not change in length. Summarizing, the superstructure that develops below T_{c_1} is a surprisingly simple dimerization of Ti sites on chains along the b axis. It is indeed justified to speak of a spin-Peierls state where spins pair on chains of Ti atoms via direct exchange.

Analogously, TiOBr adopts a spin-Peierls state upon cooling, as well. Palatinus and co-workers determined the structure of TiOBr below T_{c_1} and came to a result very similar to that described above for the TiOCl case, but with modulations only about half the size [Palatinus05]. From this, they deduce that also the relevant interactions are smaller in TiOBr, in accordance with the lower transition temperatures.

5.4.3 Intermediate Phase

In contrast to the spin-Peierls phase, for which the interpretation could already be found from the susceptibility data by Seidel *et al.* [Seidel03], it was much harder to figure out the nature of the intermediate state between T_{c_1} and T_{c_2}. Also the phase transition scheme with a second order transition followed by a first order transition upon cooling could not be explained by a simple spin-Peierls picture. In Ref. [Rückamp05a] the authors presented Ginzburg-Landau arguments that are able to give a plausible answer to these questions. Under the assumption of a non-vanishing interchain coupling, they showed that minimizing the free energy involves an incommensurate order of Ti sites. This order is not constricted within the chain direction. Rückamp *et al.* in fact argued that the formation of a dimer on one chain will push away Ti ions on neighboring chains in the directions perpendicular to the chains. In this way, displacements along the b direction couple to displacements along a and c. From the resulting effective interchain coupling the authors deduce an incommensurate component perpendicular to the chains. Furthermore, the incommensurability is predicted to decrease with temperature. Minimizing the Ginzburg-Landau free energy leads to a lock-in transition into a state with a commensurate order when the incommensurate component is sufficiently small at low temperatures.

From the experimental side, first hints towards the formation of an incommensurate order in the intermediate phase came from NMR experiments [Imai03]. The local electric field gradient, probed in the NMR measurement, suggests the existence of numerous inequivalent Ti and Cl sites in the TiOCl lattice. However, from this observation one cannot decide which microscopic degree of freedom is the origin of the incommensurability. A first proof of incommensurability was given for the bromide by x-ray diffraction, showing that it is the *lattice* that is modulated in the intermediate state [van Smaalen05]. In the following an x-ray diffraction experiment carried out by Dr. Krimmel will be described that was able to resolve the lattice distortion in the intermediate phase of TiOCl [Krimmel06]. The only remaining piece of the puzzle was thus revealed, showing that the two compounds TiOCl and TiOBr possess analogous phases and instabilities.

The experiments were conducted at the beamline BW5 of Hasylab (DESY, Hamburg). An incident photon energy of $100\,\mathrm{keV}$ was used. The sample was mounted in a cryomagnet allowing for temperatures from $1.6\,\mathrm{K}$ to $300\,\mathrm{K}$ in horizontal fields up to $B = 10\,\mathrm{T}$. The sample with a size of $1 \times 1 \times 0.01\,\mathrm{mm}^3$ was oriented with the (b,c) plane in the horizontal scattering plane.

The central result of this investigation – the peak splitting of the superlattice reflections in the intermediate phase – is presented in Fig. 5.10. At T_{c_1} the superstructure reflections split into four incommensurate satellites with an incommensurate h-component $\pm\delta$ and a smaller k-component $\pm\epsilon$, as sketched in Fig. 5.10 (a). The reflections $(\pm\delta, 0.5 - \epsilon, 0)$, $(\pm\delta, 1.5 + \epsilon, 0)$, and $(\pm\delta, 2.5 - \epsilon, 0)$ were observed, consistent with space group $Pmmn$. They were missed in the XRD experiment described in the previous section due to the choice of measurement paths in reciprocal space. The coor-
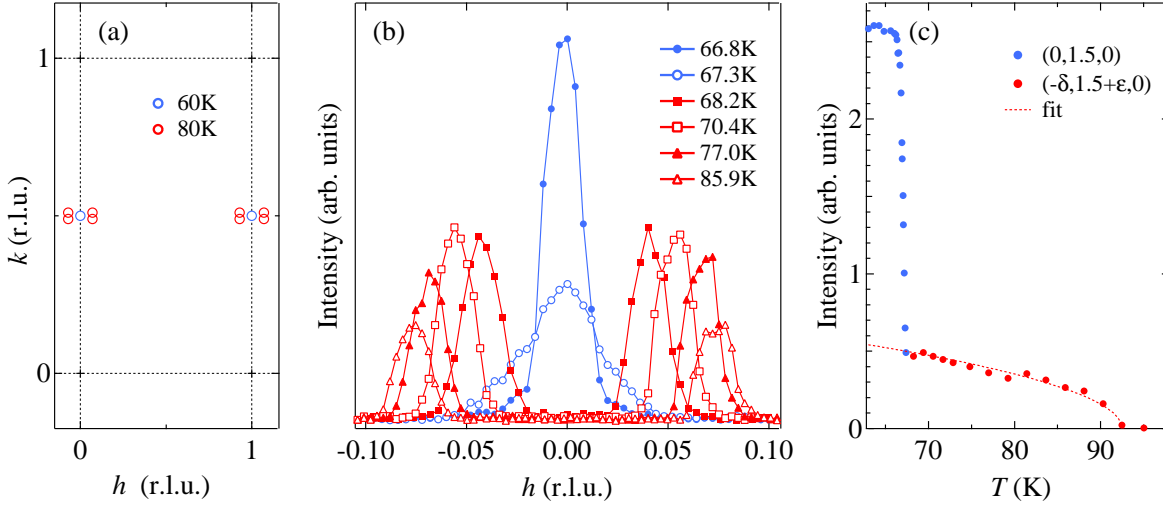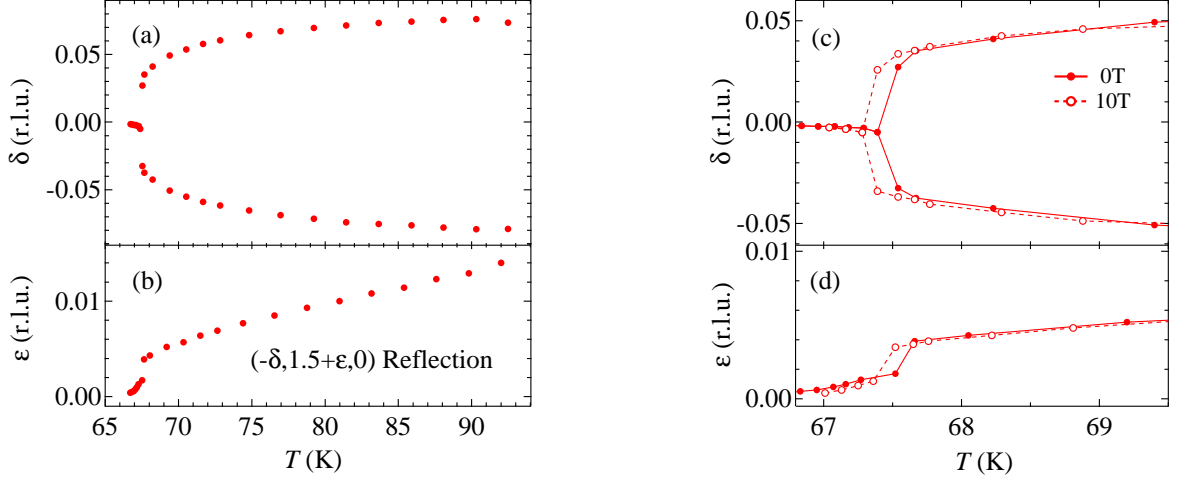
Figure 5.10: *Commensurate and incommensurate superstructure reflections of TiOCl observed by x-ray diffraction. (a) Sketch of the (a^*, b^*) plane in reciprocal space with the positions of the superstructure reflections in the spin-Peierls phase and in the intermediate phase. (b) Evolution of the $(0, 1.5, 0)$ reflection on passing through the first phase transition at T_{c_1}. The k value for each h scan along the a^* direction was optimized and hence slightly deviates from $k = 1.5$. The peak splitting is indicative of an incommensurate modulation in the intermediate phase. (c) Intensities of both the commensurate and the incommensurate reflections. The line represents a fit with the function $I(T) = I_0 \sqrt{1 - T/T_{c_2}}$ with $T_{c_2} = 92.5\,K$.*

dinates δ and ϵ of the incommensurate reflections were found to be $0 \leq \delta \leq 0.078$ and $0 \leq \epsilon \leq 0.0143$. Due to the small value of ϵ it is hard to resolve the double peaks at $(h, 0.5 \pm \epsilon, 0)$.

In Panel (b) scans in reciprocal space along the a^* direction are shown, clearly demonstrating the peak splitting of the original $(0, 1.5, 0)$ reflection. The intensities of the superstructure reflections are plotted vs. temperature in Panel (c). The temperature dependence of the commensurate reflection was already obtained in the experiment of the previous section (cf. Fig. 5.8), and a comparison yields no significant differences. The abrupt decrease of the intensity and a thermal hysteresis evidenced upon cycling the temperature confirms the first order of the phase transition between the spin-Peierls and the intermediate phase. As a new result, also the temperature dependence of the incommensurate peaks is shown. The gradual decrease of intensity on approaching T_{c_2} is indicative of a second order phase transition. Motivated by the BCS description of the spin-Peierls transition, the intensities of the incommensurate reflections were fitted by the function $I(T) = I_0 \sqrt{1 - T/T_{c_2}}$ with $T_{c_2} = 92.5\,\mathrm{K}$, yielding a good match with the data.

A further indication for the first order character of the phase transition between the dimerized and the incommensurate phase is the jump-like behavior of the incommensurate components δ and ϵ shown in Fig. 5.11. From Panels (a) and (b) it can be seen

Figure 5.11: *Incommensurate components ϵ and δ of the $(\pm\delta, 1.5 + \epsilon, 0)$ reflection of TiOCl in the intermediate phase. (a,b) Temperature dependence of δ and ϵ in zero magnetic field over the whole temperature range of the intermediate phase. (c,d) Comparison of the incommensurate positions in zero magnetic field and in an external field of $B = 10\,T$ in more detail around T_{c_1}.*

that the peak splitting takes place abruptly at T_{c_1}. The incommensurate components increase monotonically until the satellites disappear at $92.5\,\mathrm{K}$ and the orthorhombic room temperature structure is recovered.

The results for the bromide are almost identical to those of TiOCl. Complete structure determinations of the chloride [Schönleber06] and of the bromide [van Smaalen05] show that the modulation can be described by a single propagation vector $\mathbf{q} = (\delta, 0.5 + \epsilon, 0)$. The displacements correspond basically to an incommensurate version of the Ti site dimerization in the spin-Peierls phase. The components in the b direction are much larger than those along a.

In order to investigate possible field effects, the incommensurate components in zero magnetic field and in an applied field of $B = 10\,\mathrm{T}$ are compared in Panels (c) and (d) in an expanded view around T_{c_1}. For both δ and ϵ, a small, but significant shift $\Delta T_{c_1} = -0.13\,\mathrm{K}$ of the phase transition temperature is observed in the external field of $10\,\mathrm{T}$ along the chain direction. The direction of the shift towards lower temperatures is in line with the theoretic expectation for a spin-Peierls transition described in Section 2.3. The magnetic field has the effect of lowering the Fermi energy of the pseudofermions and drives the propagation vector away from commensurability. Even though the field strength is not sufficient to induce an incommensurate state at zero temperature, because the benefit from a commensurate modulation is too great, the field influences the equilibrium position of the interactions and thus lowers the transition temperature.

Moreover, also the *intensities* of the satellite reflections exhibit slight changes, thus confirming a small field induced modification of the incommensurate crystal structure.

One can summarize that the experimental observations are in line with the predictions

of Rückamp *et al.* described above: The modulations possess incommensurate components both along the b and the a axis, which is due to the coupling of Ti sites in different chains. These components become smaller upon cooling, shown in Fig. 5.11 (a,b), and therefore a lock-in phase transition of first order leads to a state with commensurate order below T_{c_1}. Also the dependence on an external magnetic field corroborates this scenario. Even though the energy scale of the applied field is small compared to the intrinsic magnetic energy scale of TiOCl, as already mentioned before, an effect could be observed. The external field leads to a shift of the transition temperature T_{c_1} towards lower temperatures, which indicates a stabilization of the incommensurate structure. From the Ginzburg-Landau free energy it can be seen that the phase transition at T_{c_1} is governed by the competition of intrachain and interchain exchange. The application of an external magnetic field then slightly shifts the equilibrium position of these competing interactions. Note however, that the authors of Ref. [Schönleber06] recently suggested a slightly different origin of the incommensurate modulation. They argued that it is not necessary to assume *magnetic* interchain interactions to explain the incommensurate order, but that also the *elastic coupling* of atoms in neighboring chains can be made responsible for this phenomenon.

5.4.4 The Spin Gap

It was already concluded by Seidel *et al.* that the low-temperature state is characterized by a spin gap: A drop of the magnetic susceptibility at T_{c_1} is observed in SQUID and ESR measurements [Seidel03, Kataev03, Zakharov06]; Raman and infrared spectroscopy find a suppression of spin excitations, which is interpreted as a consequence of the spin gap [Imai03, Lemmens04, Caimi04]. Whereas these observations are *qualitatively* in line with the interpretation of the titanium oxyhalides as spin-Peierls systems, the obvious proceeding is then to check also the *quantitative* agreement of experiment and theory. The mean field theory for a conventional spin-Peierls system predicts the BCS value of $2\Delta = 3.5 k_B T_c$ for the spin gap, where the question remains, which transition temperature has to be chosen in this non-canonical case with two phase transitions.

On the experimental side, it is in principle possible to extract the gap size from a fit of several experimentally accessible quantities that show activated behavior. For example, the magnetic susceptibility displayed in Fig. 5.6 is exponentially suppressed by the spin gap in the low temperature phase. However, the details of the fitting procedure are far from trivial due to the temperature dependence of the spin gap. Under the assumption that the gap size is proportional to the amplitude of the spin-Peierls distortion, its temperature variation will be similar to that displayed in Fig. 5.10 (c), where the intensity of the superstructure reflections is plotted versus temperature. It is thus essential for any fit that — without further knowledge of the temperature dependence of Δ — only data points at temperatures sufficiently below T_{c_1} are considered. In the interesting temperature range, where the spin gap can be reasonably assumed as constant, the SQUID data are dominated by the Curie tail, and a meaningful fit to an exponential law is thus

not possible. This perturbing effect is absent in the NMR data of Imai *et al.*, who were able to perform an exponential fit of the spin-lattice relaxation time in the temperature interval from $40\,\mathrm{K}$ to T_{c_1} [Imai03]. They obtained a value of $2\Delta = 430 \pm 60\,\mathrm{K}$ for the activation energy. It is pointed out however, that the underlying assumption of a constant spin gap is *not* well satisfied in this temperature range. Hence, the extracted value is likely to overestimate the true value of Δ at $T = 0$. Comparing the activation energy to T_{c_2}, i.e., the transition temperature where the spin-Peierls order sets in, a ratio of $2\Delta/k_{\mathrm{B}}T_{c_2} \approx 4.7$ is obtained.[2] A possible explanation for this deviation from the mean field result can be found in the importance of fluctuations described in the previous chapter, e.g., evidenced in the measurement of the heat capacity. For an ideally one- or two-dimensional system, a transition into a state with broken symmetry at finite temperatures is forbidden by the Mermin-Wagner theorem. In the real system, the Ti chains are coupled three-dimensionally, and therefore this theorem does not strictly apply. However, the fluctuations will have the effect of lowering the transition temperatures. Moreover, the geometric frustration of Ti dimerization in the TiOCl lattice can lead to a downshift of the transition temperatures. In this light the high ratio $2\Delta/k_{\mathrm{B}}T_{c_2}$ does not seem surprising.

A possibility to circumvent the problem of an exponentially small signal in the temperature range below T_{c_1} lies in μSR measurements, where the experimentally accessible quantity — the electronic relaxation rate λ — is inversely proportional to the suppressed spin fluctuation rate. μSR experiments were carried out in collaboration with Prof. Blundell's group, using the MuSR and ARGUS spectrometers at the ISIS facility near Oxford, United Kingdom. Unfortunately, it was observed that the relaxation rate saturates below $55\,\mathrm{K}$ due to an effect inherent to this technique, and so the data are not well suited for a fit to obtain the zero temperature value of the spin gap, either.

An opportunity to determine the spin gap more directly can be seen in neutron scattering experiments. By means of inelastic neutron scattering (INS), it should be possible to directly measure not only the magnitude of the spin gap, but also its temperature and **q**-dependence. Similarly to the μSR measurements, an experimental difficulty must be seen in the required sample mass of the order of $1\,\mathrm{g}$, given the mass of approximately $1\,\mathrm{mg}$ for a typical TiOCl single crystal. For an INS experiment in collaboration with Dr. Krimmel at the Institute Laue-Langevin in Grenoble, France, a sample of approximately $1\,\mathrm{g}$ of co-aligned crystals was provided. However, due to technical problems the experiment could not be performed, and therefore the plans to study the spin gap via INS had to be rescheduled to a future measurement shift.

---

[2]Note that the authors of Ref. [Imai03] obtained twice as large a ratio, as they seemed to have mistakenly included an additional factor 2. For a rigorous derivation of the correct connection between the spin gap and the activation energy, cf. Ref [Ehrenfreund77].

5.5 Electronic Structure

In the preceding sections the properties of the spin-Peierls state and of the intermediate state were discussed in detail. It was argued that fluctuations play an important role in an extended temperature range, but the microscopic nature of the fluctuations could not be identified on the basis of the experimental evidence described. In particular, it is of interest if the orbital degree of freedom is involved, as suggested by the small Jahn-Teller susceptibility of the t_{2g} orbitals. This question can be answered by an analysis of the electronic properties. A further interesting point addressed in this way is the electronic dimensionality. As reported in Sec. 5.2, the magnetic susceptibility shows a one-dimensional behavior in the paramagnetic phase, but only an analysis of the electronic structure can determine the interaction paths and the ratio of intrachain and interchain coupling.

In this chapter a thorough investigation of TiOCl and TiOBr in the normal state, both by theoretical and experimental means, is presented. Photoelectron spectroscopy (PES) was performed at room-temperature and slightly above. The experiments are complemented by LDA+U and Hubbard model calculations. Before the angle-resolved measurements are discussed, which provide momentum-resolved information on the electronic structure, the valence density of states will be examined in the following section. The last section focusses on polarization-dependent measurements that allow to determine the symmetry of the occupied orbitals.

5.5.1 Valence Density of States

The electronic structure of TiOCl and TiOBr were determined theoretically by DFT calculations in the group of Prof. Valentí. The generalized gradient approximation (GGA) [Perdew96] and the so-called LDA(GGA)+U approximation [Anisimov93] were employed using the full-potential linearized augmented plane-wave code WIEN2k [Blaha01]. Since the LDA+U calculations are performed on a spin-polarized state, both a ferromagnetic and an antiferromagnetic alignment of the Ti spins along the b direction were considered. The latter was found to be lower in total energy compared to the FM state [Saha-Dasgupta04]. In all calculations $RK_{\max} = 6$ and $56 \, \text{k}$ irreducible points were used for Brillouin-zone integrations. The values for the onsite Coulomb repulsion U and onsite exchange J_0 were taken to be $3.3 \, \text{eV}$ and $1 \, \text{eV}$, respectively, which accounts well for the intersite chain exchange constant derived from the magnetic susceptibility.

In Fig. 5.12 (a) the atomically-resolved GGA density of states of TiOCl is presented [Saha-Dasgupta04]. The calculation yields a clear separation of states with predominant Ti $3d$ character at the Fermi energy and states derived mainly from O and Cl p levels at higher binding energies. As expected for the octahedral environment of Ti sites, the d band is split into t_{2g} and e_g subshells, with the single electron residing in one of the t_{2g} orbitals, which point between the O and Cl ligands and are therefore lower in energy. The GGA calculation incorrectly suggests a metallic behavior. This is an artefact
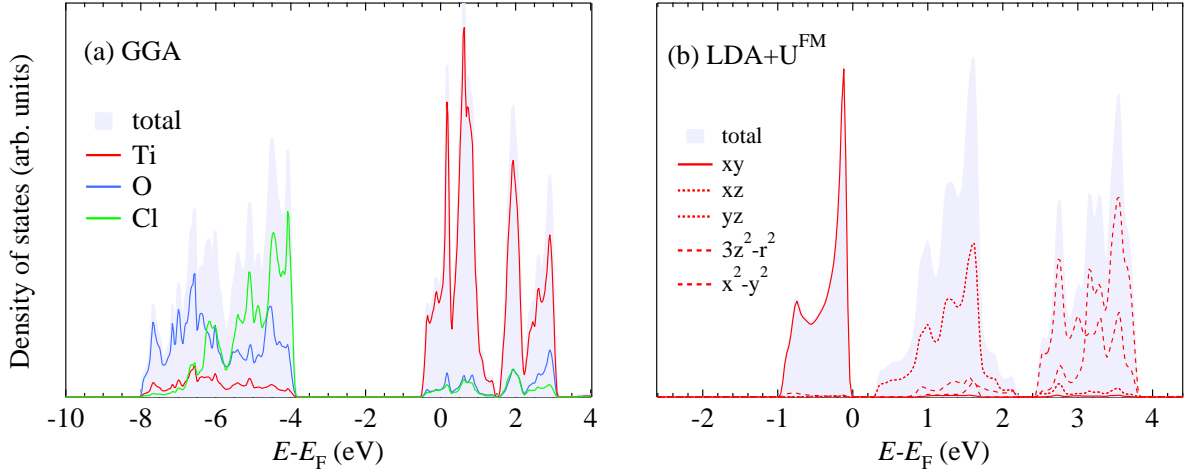
Figure 5.12: *TiOCl density of states obtained from DFT calculations. (a) GGA density of states decomposed into Ti, O, and Cl contributions. The Ti $3d$ states are split by the crystal field in t_{2g} levels below $\approx 1.5\,eV$ and e_g levels above this energy. (b) Orbitally-resolved Ti d contribution to the density of states, calculated in the LDA+U^{FM} approximation. Additional to the t_{2g}-e_g splitting a correlation gap has opened up.*

caused by the inadequate treatment of the Coulomb term in this approximation [Saha-Dasgupta04] and not surprising, having in mind that TiOCl is a system with an odd number of valence electrons — a situation that automatically leads to a metallic state when electronic correlations are neglected, as for instance in the single-particle Bloch theory. A better description of the electron–electron interaction is obtained by the LDA(GGA)+U approach, which is carried out on a spin-polarized state. Focussing on the interesting low energy part of the DOS, in Panel (b) the Ti density of states is projected onto states with different orbital character. For the calculation a FM spin arrangement was assumed. It can be seen that additional to the t_{2g}-e_g separation, the $3d_{xy}$ band is split off, and a gap at the Fermi energy appears in accordance with the insulating nature of TiOCl. Remarkably, the Ti DOS below the Fermi energy has almost zero admixture of states with d_{xz}, d_{yz}, or e_g symmetry.

These theoretical results can be checked experimentally by angle-integrated photo-emission. To this end measurements were performed, mainly in the homelab using He I (21.2 eV) and Al K$_\alpha$ (1486.6 eV) radiation and an Omicron EA 125 HR electron energy analyzer. Additionally, synchrotron radiation experiments were carried out at the SIS beamline of the Swiss Light Source (SLS) at the Paul-Scherrer-Institute in Villigen, Switzerland, using a Scienta SES 100 analyzer and a photon energy of 60 eV. The layered structure of the oxyhalides facilitates easy surface preparation by *in situ* crystal cleavage. The long-range order of the resulting surfaces can be inferred from the LEED pattern in Fig. 5.13 (a). XPS measurements show that the cleaved surfaces are clean, as only titanium, chlorine and oxygen core levels were detected. In particular, it can be concluded from the data plotted in Panel (b) that the surfaces are not contaminated by
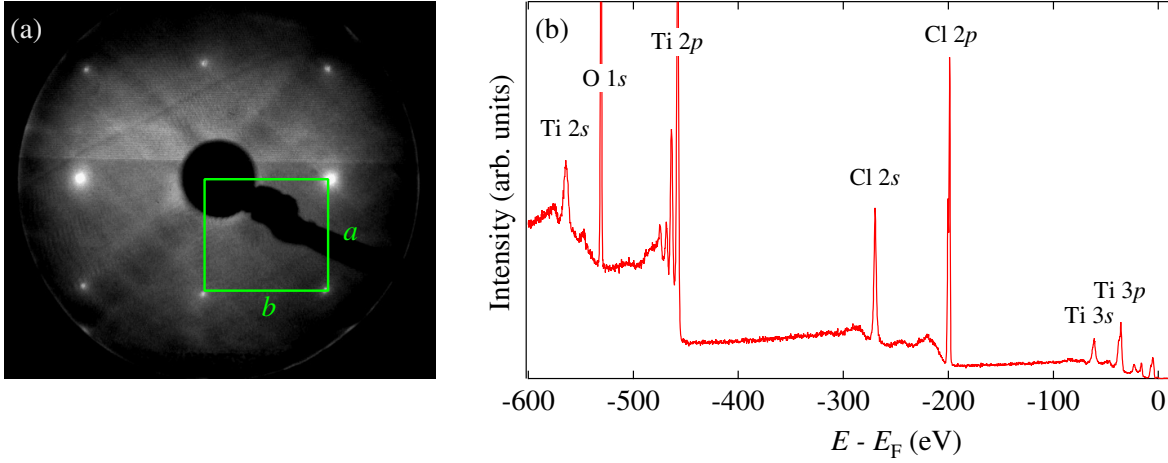
Figure 5.13: (a) LEED pattern obtained from a cleaved surface of a TiOCl crystal at a primary electron energy of $\approx 60\,eV$. A unit cell of the primitive rectangular surface lattice with axes a and b is indicated. (b) TiOCl XPS spectrum. Note the absence of carbon contamination, as no indication of a C 1s peak, which would be expected at a binding energy of 285 eV, can be found.

carbon. Because of the high electrical resistivity of the samples, all photoemission data were taken at room temperature or above in order to minimize sample charging.

Figure 5.14 shows angle-integrated photoemission spectra measured with 21.2 eV, 60 eV, and 1486.6 eV photons [Hoinkis05]. The data of Panels (a) and (b) were recorded in an angle-resolved mode with an energy resolution of 60 meV and 80 meV, respectively, in steps of 1° along the crystallographic b direction and summed up to an angle-integrated result. Note, however, that the angle integration thus only extends over a single path in reciprocal space. For the Ti d band, this is a good approximation to an integration over the entire Brillouin zone for the following reason: From LDA and LDA+U studies [Seidel03, Saha-Dasgupta04] the dispersion along the a and c axes is expected to be negligible compared to the b-axis dispersion. An experimental confirmation, at least for the chloride, is given in the following section. For the O/Cl p manifold, the situation is different. While the dispersion along the c direction will be certainly small due to the layered crystal structure, the dispersion turns out to be comparable for the orthogonal directions a and b within the layers. The above method therefore yields only a limited representation of a complete integration in momentum space for these bands. The spectrum of Panel (c) was measured in the angle-integrated mode of the analyzer, i.e., with an acceptance angle of $\pm 8°$. The spectrum thus integrates amply over the Brillouin zone, whose edges correspond to an angle of less than 3° at these high kinetic energies. The energy resolution is dominated by the line width of the monochromated x-ray source and amounts to about 350 meV.

All three experimental spectra consist of two well separated regions. From the comparison of theory and experiment one can identify the low-binding-energy peak as Ti 3d-like, whereas the states between $-9\,eV$ and $-4\,eV$ are predominantly derived from
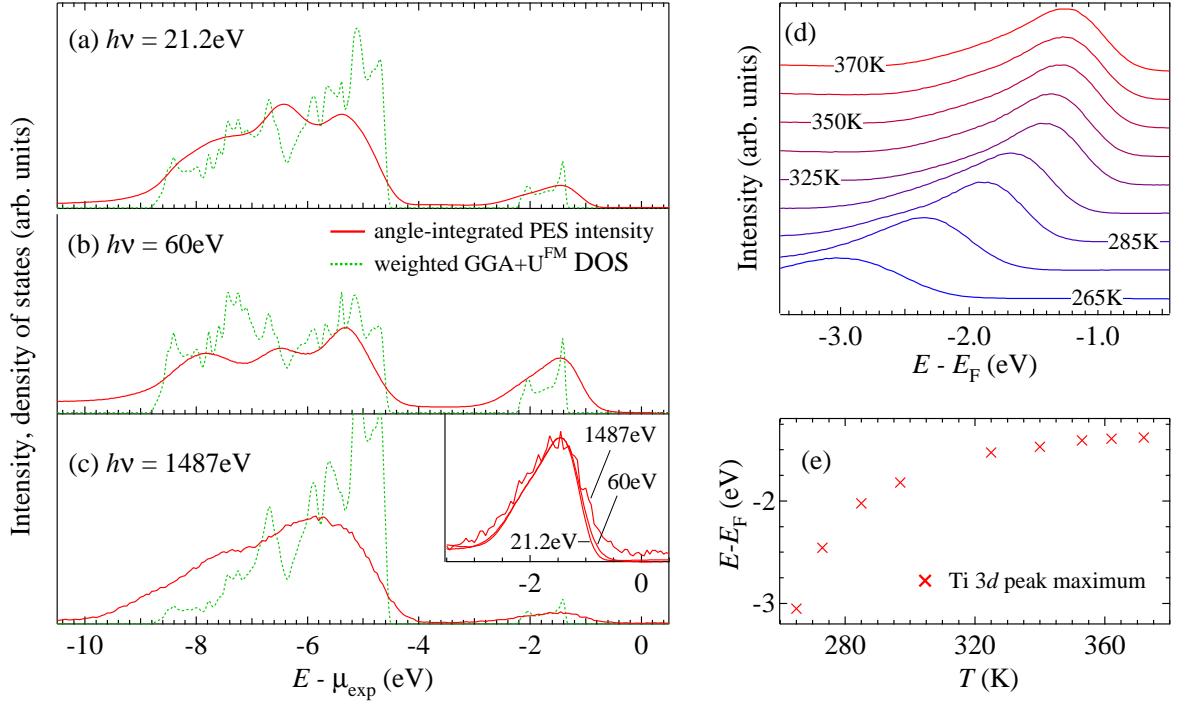
Figure 5.14: *Photon energy and temperature dependence of TiOCl photoemission. (a,b,c) Angle-integrated photoemission spectra recorded with different photon energies compared to the GGA+U^{FM} density of states weighted with photoemission cross sections. (d) Evolution of the Ti 3d peak as a function of temperature. (e) Temperature dependent shift of the Ti 3d peak maximum caused by charging effects.*

Cl 3p and O 2p levels. The differences between the spectra measured at different photon energies, normalized to the same integrated area, can be traced back to matrix element effects. One observes that the Ti 3d band is most strongly pronounced in the synchrotron data with a photon energy of 60 eV, whereas the relative Ti signal is much weaker in the x-ray induced experiment. The 3d peaks of the three measurements are compared in the inset. They are essentially of identical shape, only the $h\nu = 1487$ eV spectrum shows slight deviations, as it was measured with a significantly larger energy resolution and sits on a higher constant background. This experimental observation confirms the GGA result that the admixture of O and Cl p states to this peak is vanishingly small. Otherwise, the superposition of d and p orbitals would produce different shapes at the various excitation energies due to matrix elements effects. It can be seen very clearly how such effects influence the spectral form of composite bands when considering the Cl/O manifold. While the energetic position and the width are the same, the shape strongly differs between the three measurements. This is not surprising, given that this broad structure is comprised out of 12 bands carrying two electrons each. Consequently, cross section effects will lead to different spectral shapes of the total sum of these bands.

Before the experimental spectra can be compared to theoretical results, a few remarks

concerning the energetic alignment are necessary. Due to the high resistivity of the oxyhalides, charging effects were observed that grew in extent with decreasing temperature. In Fig. 5.14 (d) angle-resolved photoemission spectra ($h\nu = 21.2\,\mathrm{eV}$) are plotted for various temperatures. Upon cooling the spectra progressively shift to higher binding energies, with the effect that it is not possible to conduct photoemission experiments significantly below room temperature. In particular, the temperature region of the phase transitions is not accessible for this technique.

From the temperature dependence of the Ti 3d peak, depicted in Panel (e), it can be seen that the charging is almost negligible at and above $\approx 370\,\mathrm{K}$. In this situation the maximum of this peak is located at 1.45 eV below the experimental chemical potential μ_{exp}, which corresponds to the Fermi edge position of a silver foil. Based on this result, all TiOCl photoemission spectra are aligned accordingly. The energy position of the Ti 3d-peak in TiOBr depends on temperature in a very similar way. It was aligned to the same value of 1.45 eV below μ_{exp}.

In order to simplify a comparison with the experiment, the theoretically obtained spectra discussed in the following were also shifted in energy to match the experimental data. In Panels (a–c) the photoemission spectra are compared to GGA+U results that were generated by weighting the atomic contributions of the density of states with the according photoemission cross sections [Yeh85] for the different photon energies. The overall shape of the theoretical DOS and the experimental spectra are rather similar. With the chosen energy alignment the relative separation between Ti 3d and the ligand p states still appears $\approx 0.5\,\mathrm{eV}$ too small in the calculations. The value of 2 eV for the correlation gap as determined from optical spectroscopy [Maule88, Rückamp05a, Kuntscher06] is in reasonable agreement with the photoemission data and the LDA+U calculations (not seen here, as the figure displays only the occupied DOS).

Concerning the p bands, it is clear that a detailed match of the spectral form cannot be expected. As pointed out above, the photoemission spectra of Panels (a) and (b) do not represent a complete integration over the Brillouin zone. Furthermore, the weighted GGA+U DOS is a very simplified approach to model the matrix element effects in photoemission. Nevertheless, one notices that the general trend of the photon energy dependence is reproduced. In particular, the Ti weight is strongest for $h\nu = 60\,\mathrm{eV}$, in accordance with the experimental observation. For this excitation energy, the cross section of Cl states is suppressed in relation to Ti and O states. Consequently both the experimental and theoretical $h\nu = 60\,\mathrm{eV}$ spectra display a comparably small weight at the low-binding-energy onset of the p bands. Before discussing the shape of the Ti 3d band — as obtained from theory and experiment —, the differences in the TiOCl and TiOBr valence densities of states will be analyzed.
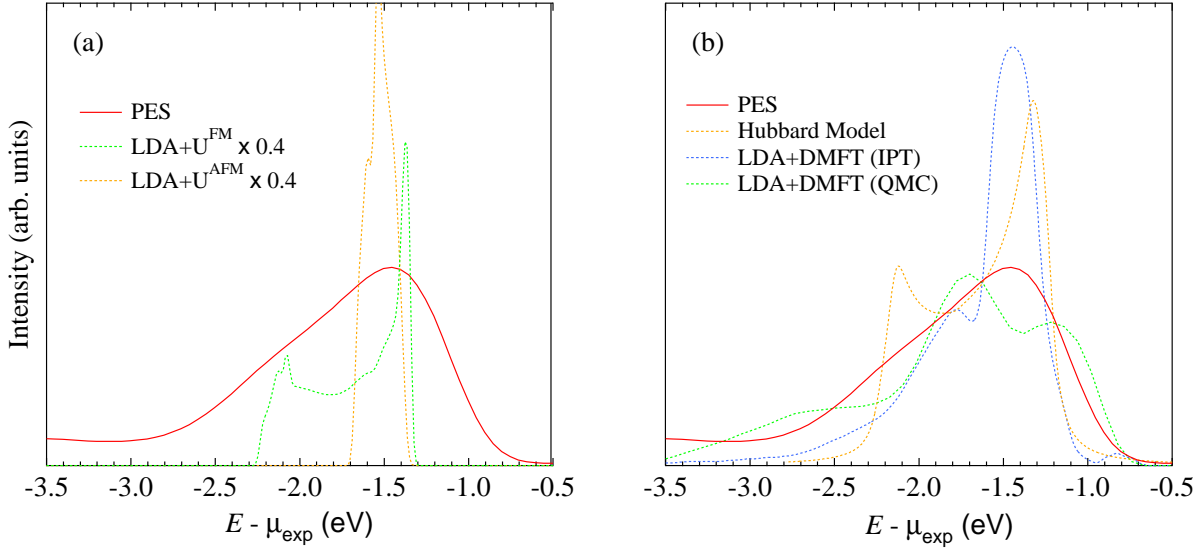
Figure 5.15 shows angle-integrated photoemission spectra and GGA+U densities of states for both compounds. In contrast to the above discussion, which focussed on the excitation energy dependence, no weighting with cross sections was conducted. The measurements were performed with 21.2 eV photons and with a resolution of 60 meV (TiOCl) and 110 meV (TiOBr), respectively. Comparing the Ti 3d peak of TiOCl
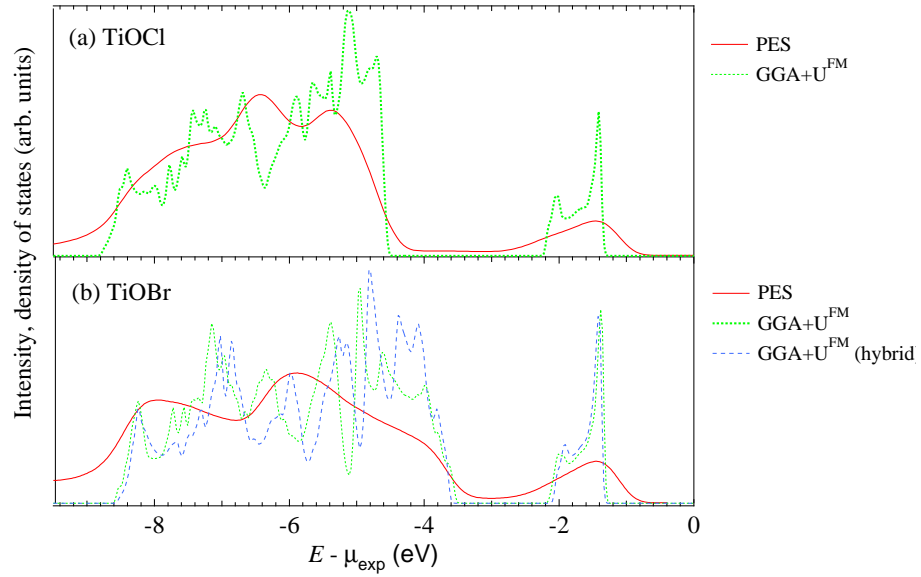
Figure 5.15: *Comparison of the TiOCl and TiOBr valence density of states. (a) Angle-integrated photoemission spectrum and GGA+U density of states of TiOCl. (b) Angle-integrated photoemission spectrum of TiOBr compared to two GGA+U^{FM} results. The first one is the density of states of a regular TiOBr crystal, whereas the second one is calculated for a fictitious hybrid compound, viz., TiOCl with the crystal structure of the bromide.*

and TiOBr, one notices that the experimental results as well as the GGA+U densities of states are almost identical for the two compounds. Consequently, an equally poor match between theory and experiment is found for each compound. A better agreement between the calculated and the experimental spectra is found as far as the width of the p bands is concerned. In the bromide this width is considerably larger, which results in a smaller d–p separation. In order to address the question whether this difference is caused by the change in chemistry or rather related to the structural expansion, a third calculation was performed. There a hypothetical compound was assumed with the crystal structure of TiOBr, but with Br substituted by Cl. In Panel (b) the resulting density of states is plotted. From the comparison to the TiOBr DOS it can be deduced that the size of the d–p gap decreases from the Cl to the Br system mainly due to the expanded unit cell of TiOBr.

In the following the focus lies on the Ti $3d$ part near the chemical potential, which is shown as a blow-up in Fig. 5.16. In Panel (a) the experimental data are compared to two LDA+U calculations. The weighting with cross sections for the atomic species is not necessary for this band, as it consist almost exclusively of Ti states. It would therefore not change its spectral form by this procedure (cf. Fig. 5.14 (a–c)). Beginning with the LDA+U DOS assuming a ferromagnetic spin arrangement, one sees that the experimental $3d$ spectrum has a similar asymmetry as the LDA+U^{FM} DOS, but is much broader. It is emphasized that the experimental width is perfectly reproducible and

Figure 5.16: *Ti 3d part of the angle-integrated photoemission spectrum of TiOCl ($h\nu = 21.2\,eV$) compared to the density of states obtained from various calculations. (a) LDA+U with ferromagnetic and antiferromagnetic spin order ($U = 3.3\,eV$). (b) 1D Hubbard model, LDA+DMFT using iterative perturbation theory (Ref. [Craco04]), and LDA+DMFT using quantum Monte Carlo (Ref. [Saha-Dasgupta05]). All spectra are normalized to the same integrated area.*

not due to instrumental broadening, which is much smaller. In the above analysis of LDA(GGA)+U spectra, always the *FM* configuration was assumed. This is not well justified, one would rather like to approximate the system by an *AFM* configuration, which seems the more natural choice considering the Bonner-Fisher-type susceptibility. Remarkably, in this case the comparison to the LDA+U DOS yields an even stronger disagreement — the Ti band is significantly reduced in width. This is in contrast to the naive assumption that antiferromagnetically aligned spins allow for an increased hopping probability of neighboring sites compared to ferromagnetic spins, which cannot itinerate due to the Pauli exclusion principle. Therefore the AFM configuration would be expected to lead to an increased band width, opposite to the GGA+U result.

Note that LDA+U accounts for the onsite Coulomb interaction only in a mean-field way and is thus effectively still a one-electron theory for statically ordered systems. One may thus speculate that the origin for the conflicting 3d widths lies in pronounced electronic correlation effects and/or fluctuations of spin-Peierls or orbital nature beyond the scope of LDA+U. Electronic correlation effects can in principle be accounted for by a combination of LDA and dynamical mean field theory (LDA+DMFT) or by suitable many-body models. Panel (b) shows a comparison of the experimental Ti 3d spectrum to two different LDA+DMFT calculations. They are taken from Refs. [Craco04] and [Saha-Dasgupta05] and used different impurity solvers and basis sets. While the LDA+DMFT curves indeed display a broadening much closer to that of the experiment, none of these curves can sufficiently explain the shape of the experimental data. The striking
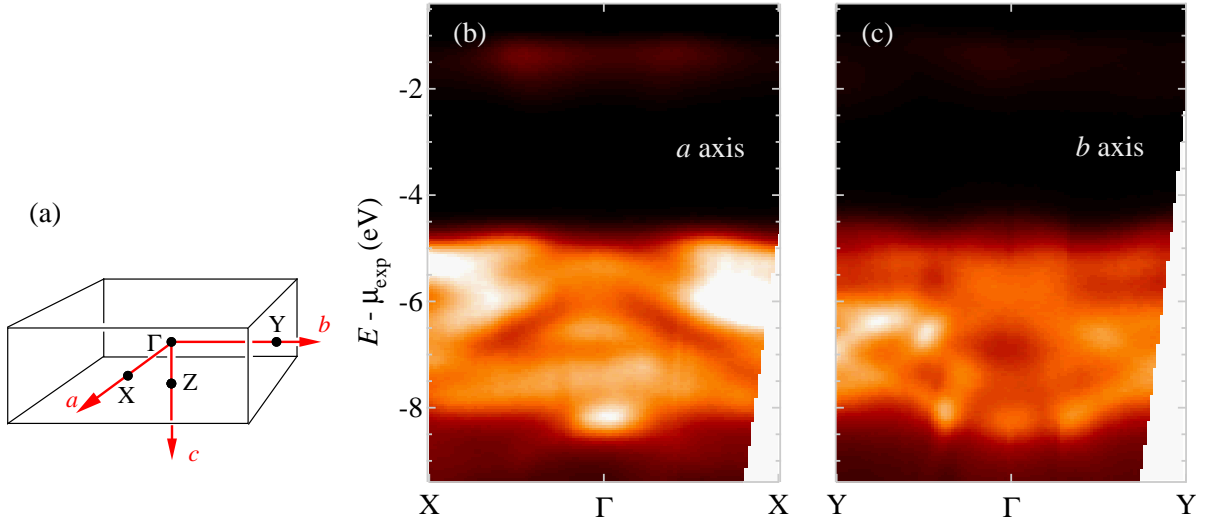
Figure 5.17: *Angle-resolved photoemission of TiOCl single crystals. (a) Orthorombic Brillouin zone with the high-symmetry points Γ, X, Y, and Z. (b,c) ARPES intensity plots $I(\mathbf{k}, E)$ and EDCs along the crystallographic axes a and b, corresponding to the XΓX and YΓY lines in the Brillouin zone.*

disagreement between the two LDA+DMFT calculations should probably be traced back to the fact that, contrary to the multi-orbital QMC solver, the IPT solver is quite uncertain for anisotropic multi-band problems [Lichtenstein98].

As a further approach to explain the experimental findings, the one-particle spectral function of the 1D Hubbard model at half band-filling was determined by Prof. Jeckelmann and Dr. Benthien using the dynamical density-matrix renormalisation group (DDMRG) method [Jeckelmann02, Benthien04]. The calculations were performed on 32-site chains with open boundaries, and up to 200 density-matrix eigenstates were kept. The parameters $U = 3.3\,\text{eV}$ and $t = 0.23\,\text{eV}$ were chosen in accordance with the DFT calculations, the broadening of the spectra is $\eta/t = 0.2$. The resulting density of states is also shown in Fig. 5.16 (b), but it is found again that the bandwidth and the detailed spectral shape of the photoemission data are not reproduced.

It must be thus concluded that the experimentally determined valence density of states in the paramagnetic phase of TiOCl is far from being understood.

5.5.2 Electronic Dispersion and Dimensionality

Turning now to the angle-resolved photoemission data, the electronic dispersions of TiOCl and TiOBr will be discussed [Hoinkis05]. The photoemission experiments were performed with He I radiation using an Omicron EA 125 HR electron energy analyzer with the resolution set to 60 meV for the TiOCl and 110 meV for the TiOBr measurements. The angular acceptance was $\pm 1°$ in both cases.

In Fig. 5.17 the chloride data are presented as intensity plots $I(\mathbf{k}, E)$ in a broad energy
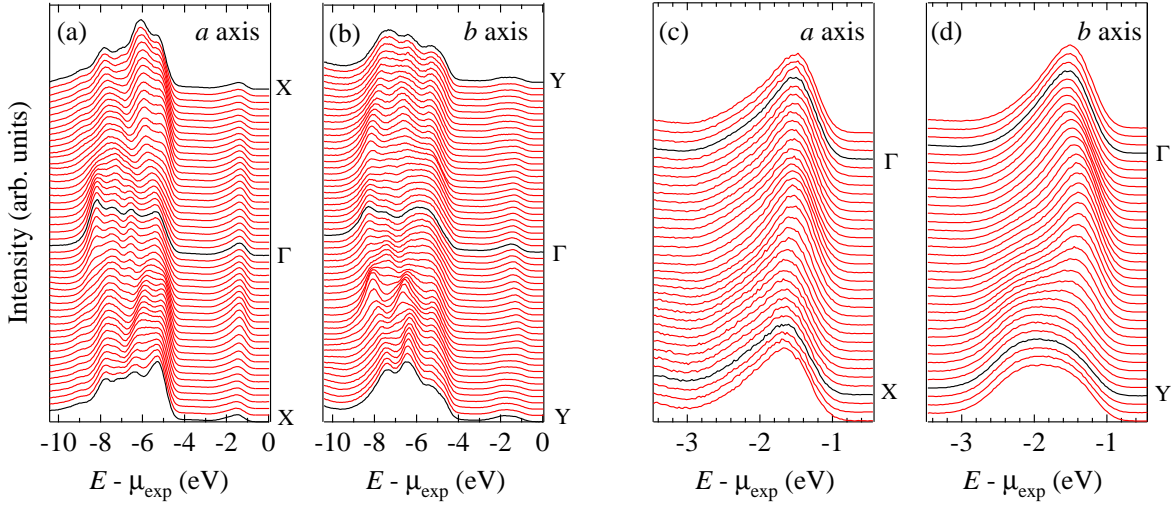
Figure 5.18: *(a,b) ARPES EDCs of the full TiOCl valence band along the crystallographic axes a and b. (c,d) Ti 3d part of the EDCs.*

range. In Panel (a) the orthorhombic Brillouin zone is sketched together with the high-symmetry points conventionally used to describe the measurement paths in reciprocal space. In this thesis measurements along the crystallographic directions a and b are labelled with the paths ΓX and ΓY, although strictly speaking, this is only true for a vanishing k-component along the c axis, which is perpendicular to the crystal surface. The matter is complicated by the fact that this component $k_\perp$ is not conserved in the photoemission process and therefore not easily determined. However, for quasi-two-dimensional compounds it is justified to neglect the perpendicular dispersion, and so the value of $k_\perp$ becomes irrelevant, as discussed in Chapter 3.

For a presentation of photoemission data in a broad energy range, it is important to consider the energy dependence of the wave vector $k_\parallel$ according to Equation 3.4. As an example to illustrate this effect, the emission angle of 27.6° corresponds approximately to the Y-point for He I excited electrons stemming from the Ti $3d$ band. An electron with a binding energy of 8 eV emitted under the same angle possesses a 26% smaller momentum $k_\parallel$. Panels (b) and (c) show measurements along the two crystallographic directions a and b. The energy dependence of the wave number described above was accounted for in this plot, leading to the white space in the lower corners of the images.[3] As can be seen, there is well-pronounced dispersion particularly in the Cl $3p$/O $2p$ part of the spectra between -9 eV and -4 eV. This view is particularly suited to reveal the clear symmetry of the dispersions with respect to the Γ-point.

An alternative presentation of the same data is given in Fig. 5.18, where the energy

---

[3]Note that this effect is not taken account of in the ARPES intensity plots of this thesis apart from Fig. 5.17, since the effect can be neglected when the energy range shown is small compared to the excitation energy.

distribution curves (EDCs) are plotted. Panels (a) and (b) show the spectra in the same energy window, and again the vigorous dispersion in the O/Cl manifold becomes apparent. This behavior and the clear symmetry of the dispersions are indicative of the good crystal surface quality.

Panels (c) and (d) show an enlargement of the Ti $3d$ part of the ARPES spectra. From a comparison of the bare EDCs one can easily see that the spectral changes along the b axis are considerably stronger than along the a axis. This observation confirms the quasi-one-dimensional electronic (and magnetic) nature of TiOCl and corroborates the LDA+U prediction that 1D chains are formed by direct hopping via Ti $3d_{xy}$ orbitals along the b direction. Note, however, that the dispersion along the a axis is still finite as seen from a closer inspection of the **k**-dependence of the peak maximum, which moves to slightly higher binding energy from Γ to X. The size of the a axis dispersion is directly related to the interchain coupling, which plays an important role for the complex spin-Peierls transition behavior, as outlined in Section 5.4.3.

The Ti $3d$ spectra of the a-axis ARPES data are all of a rather similar asymmetric shape. Starting from Γ, the band initially changes its binding energy only slightly, reaches a maximum at about $\frac{1}{2}\Gamma$X, and then disperses downwards until the X-point. The spectral changes in the b-axis data, depicted in Panel (b), are somewhat more complex. They start out at Γ with a single peak at $\approx 1.5\,\mathrm{eV}$ below the chemical potential. With increasing momentum the peak shifts clearly towards μ_{exp} and reaches its smallest binding energy about halfway between Γ and the zone edge. For even larger momentum the peak rapidly drops in intensity and seems to move back to slightly higher binding energy. At the same time a new feature appears at $\approx -2.5\,\mathrm{eV}$ until at the zone boundary (Y) the spectral shape has evolved into a broad hump. This behavior and the relatively large broadening of these structures have been reproducibly observed on many different samples and is hence to be taken as intrinsic.

A comparison of the experimental a-axis dispersion to that of the LDA+U$^{\mathrm{FM}}$ calculation is displayed in Fig. 5.19 (a,b) and yields qualitative agreement concerning size and direction of the dispersion. Note again, however, that the LDA+U bands had to be shifted in energy to give a good match to the ARPES data.

The lower panels of Fig. 5.19 show the experimental b-axis dispersion as ARPES intensity plot in comparison with various theoretical calculations. Starting with the theoretical LDA+U$^{\mathrm{FM}}$ dispersion calculated for the high-temperature (non-dimerized) structure, a pronounced disagreement with the experiment is found, particularly in the second half of the ΓY direction: Here the theoretical bands continue to disperse upwards, whereas the experimental dispersion turns over and bends downwards until at the Y-point the spectral weight distribution is strongly broadened and reaches down further to higher binding energies than at Γ. Assuming an antiferromagnetic spin alignment in the LDA+U approach doubles the unit cell and hence results in a dispersion symmetric about $\frac{1}{2}\Gamma$Y (Panel (e)). Although LDA+U$^{\mathrm{AFM}}$ thus reproduces the dispersion maximum halfway along ΓY, it does clearly not account for the asymmetric experimental behavior. Motivated by speculations that the unusual high-temperature behavior of
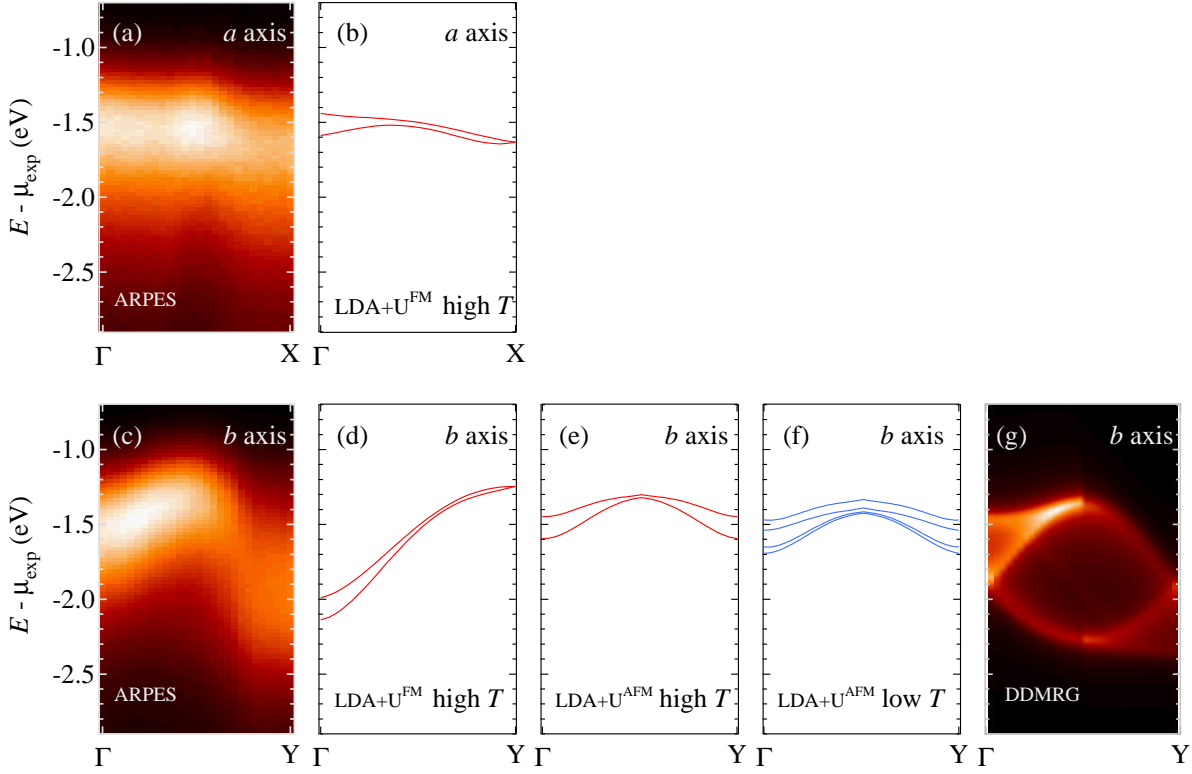
Figure 5.19: *Experimentally determined Ti 3d dispersion of TiOCl compared to various calculations. (a) ARPES intensity plot $I(\mathbf{k}, E)$ of the a-axis dispersion. (b) Corresponding LDA+U$^{\mathrm{FM}}$ bands. (c) ARPES intensity plot $I(\mathbf{k}, E)$ of the b-axis dispersion. (d,e) Corresponding LDA+U$^{\mathrm{FM/AFM}}$ bands calculated for the high-temperature structure ($U = 3.3\,eV$, $J_0 = 1\,eV$). (f) LDA+U$^{\mathrm{AFM}}$ bands calculated for the dimerized low-temperature structure. (g) One-particle spectral function of the Hubbard model calculated by the DDMRG method ($U = 3.3\,eV$, $t = 0.23\,eV$).*

TiOCl could be caused by fluctuations of the spin-Peierls order parameter, Panel (f) shows LDA+U$^{\mathrm{AFM}}$ dispersions for the dimerized low-temperature phase. Note that such fluctuation effects have been observed in *charge*-Peierls systems well above the actual transition temperature [Schäfer01]. However, as evident from the figure, the effect of (fluctuating) dimerization results in band doubling but is otherwise rather small and hence cannot explain the phenomenology of the ARPES data.

Panel (g) finally displays the momentum-resolved spectral weight distribution of the 1D single-band Hubbard model, calculated within DDMRG for the U and t parameters of the LDA+U calculations. In this case the spectra are entirely of incoherent nature and correspond to momentum-dependent continua. They are structured in intensity due to the phase space available for decomposition of a real (photo-)hole into separate collective spinon and holon excitations, which were introduced in Section 2.4. Lines of singularities are found dominating the excitation continuum. For example, the low binding energy

singularity in the first half of the Brillouin zone arises from hole fractionalization in which the spinon propagates with the entire excitation energy, leaving zero energy for the holon channel. It therefore reflects the dispersion of a bare spinon, whose bandwidth scales with the exchange integral J, and is referred to as the *spinon branch*. The *holon branch* is characterized by the opposite energy partitioning, i.e., completely in favor of the holon channel. Two holon branches cross exactly in the center of the Brillouin zone, at a lower energy than the minimum of the spinon branch. From there a branch with stronger intensity disperses upwards, reaching a maximum at $\frac{1}{2}\Gamma Y$, where it meets the spinon branch. The weaker pronounced branch, also referred to as "shadow band", disperses downwards from Γ. The dispersion of the holon branches is expected to scale with the transfer integral t.

Comparing the DDMRG result with the ARPES data, several corresponding features are found such as the initial upward dispersion (due to spin and charge branches in the Hubbard model [Benthien04]), the dispersion maximum at $\frac{1}{2}\Gamma Y$, and the asymmetric shift of weight to larger binding energy towards the Y-point. Also the overall energy width of the spectral weight distribution is greater than in the LDA+U calculations. On the other hand, the experiment does not show the pronounced spin-charge splitting between Γ and $\frac{1}{2}\Gamma Y$ predicted by DDMRG, nor the holon "shadow band" [Benthien04].

In addition, the spectral functions of two closely related Hubbard-type models in the Mott-insulating phase were calculated: An extended Hubbard model including a nearest-neighbor Coulomb repulsion V, and the t-t'-U model [Daul00] that takes into account a next-nearest-neighbor hopping t'. The resulting spectral functions (not shown) for $V/t < 2$ and $t'/t < 0.5$, respectively, display no qualitative differences compared to the simple Hubbard model spectral function. However, the spectral weight of the spin branch in the t-t'-U model is significantly reduced for appropriate parameters ($U/t = 15.7$, $t'/t = 0.14$) [Saha-Dasgupta04]. This may indicate why the spin-charge splitting is not resolved experimentally.

Overall, the agreement is much better for the Hubbard model calculations than for the LDA+U band dispersions, suggesting that the experimental spectra are indeed dominated by electronic correlation effects. However, the following two arguments can be brought forward suggesting that the 1D single-band Hubbard model cannot really be expected to account fully for the photoemission spectra. First of all, this model completely ignores the orbital degrees of freedom. The crystal-field splitting between the d_{xy} ground state and the excited $d_{xz,yz}$ states is only a few $100\,\text{meV}$ [Seidel03, Rückamp05b] and hence virtual excitations into these states will be even more important than the double occupations on the same site (with energy scale $U = 3.3\,\text{eV}$) already contained in the single-band model. Therefore, it would be highly desirable to compare the ARPES spectra to that of a suitable multi-orbital Hubbard model, which however is still out of reach for the DDMRG.

As second argument, it is pointed out that interchain interactions were found to play an important role for the spin-Peierls physics of TiOCl, as discussed in Sec. 5.4.3. It must thus be examined carefully if neglecting the two-dimensional coupling in the 1D
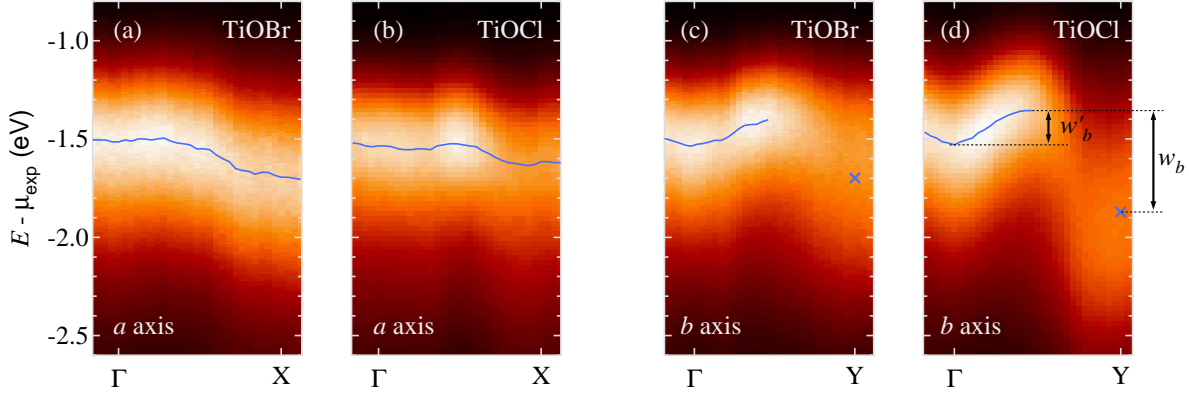
Figure 5.20: *ARPES intensity plots $I(\mathbf{k}, E)$ of TiOBr and TiOCl along the crystallographic axes a and b, corresponding to the $X\Gamma X$ and $Y\Gamma Y$ lines in the orthorhombic Brillouin zone. Blue lines indicate the peak positions of the EDCs. The blue crosses mark the first moment of the EDCs at the Y-points.*

Hubbard model can be responsible for the disagreement between experiment and model calculation.

A comparison between the isostructural compounds TiOBr and TiOCl now opens the possibility to further explore the possible reasons for this discrepancy [Hoinkis06]. In Fig. 5.20 the spectral weight distributions of the Ti $3d$-band of both compounds are presented. The four panels show ARPES intensity plots $I(\mathbf{k}, E)$ along the crystallographic axes a and b, together with lines and markers that serve as a guide-to-the-eye for the spectral dispersions. The lines indicate EDC peak maxima obtained by a peak fitting procedure. For both compounds, this works well along the a direction and in the first half of the path from Γ to Y, i.e., along b in direct space. In the second half, however, the EDCs lose their single-peak-like shape: An additional feature at higher binding energies appears and thereby the spectra gradually change their form to end up in a broad hump, as described above. Thus, a fit with a single peak is not adequate here. Instead, the first order moment of the EDCs at the Y-point (indicated by crosses in Fig. 5.20) was taken as a measure.

The dispersions of the bromide both along the crystallographic a and b axes show a strong *qualitative* resemblance to the chloride. For a *quantitative* comparison of the electronic dispersions between the two compounds, the parameters w_a, w_b, and w_b' are listed in Table 5.5. The unprimed quantities refer to the overall dispersion widths, while w_b' measures the width of only the inner part of the dispersion in the region from Γ to about $\frac{1}{2}\Gamma$Y. These widths are determined either from the difference of the maximal and minimal peak energies along the corresponding paths in $\mathbf{k}$-space as obtained by the fitting procedure (see lines in Fig. 5.20), or the difference between the maximum peak energy and the first order moment at the Y-point in case of w_b (see markers in Fig. 5.20). The errors indicated reflect the scatter from several samples and measurements.

As is immediately read off from Table 5.5 the overall dispersion width along b is

Table 5.5: *Dispersions w_a, w_b, and w'_b of the Ti 3d-band in TiOBr and TiOCl, measured from the maximum to the minimum energy of the peak for the a direction, and from the maximum energy of the peak to the first moment of the Y-point EDC for the b direction, respectively.*

	TiOBr	TiOCl
w_a	0.27(3) eV	0.12(3) eV
w_b	0.26(5) eV	0.47(5) eV
w'_b	0.13(1) eV	0.17(1) eV

significantly *smaller* in TiOBr with respect to TiOCl — contrary to the *a* direction, where the dispersion width is *larger* in TiOBr. Given that both systems and in particular their electronic structures are governed by the same physics we hence conclude that the anisotropy of TiOBr is less pronounced than in TiOCl. This is in line with the trend in the relevant hopping integrals as derived from downfolding LDA+U results. Furthermore, it was observed that the Bonner-Fisher curve indicative for 1D Heisenberg chains does not provide a good fit for the high-temperature magnetic susceptibility of TiOBr in contrast to TiOCl [Lemmens05]. Without knowledge of the precise origin of the observed dispersions one has to be careful to take the ratio $w_b/w_a \sim 1$ in TiOBr as evidence that this system actually is almost ideally two-dimensional or at least close to one. Nevertheless the non-negligible interchain coupling can not be discarded on the basis of these data.

Focussing now on the central part of the dispersion along the *b* axis marked by lines in Panels (c) and (d), it is pointed out that within the single-band 1D Hubbard model this part corresponds to the (ω, k) region of the spinon and holon branches (see Fig. 5.19 (g)). Hence, depending on a dominating spinon or holon character of the experimental dispersion, the width w'_b should scale linearly either with the exchange constant J or with the hopping integral t, as outlined above. The value of J can be extracted from magnetic susceptibility measurements [Seidel03, Rückamp05a]. The transfer integral t can be inferred from the Hubbard model perturbation expression for the exchange constant, $J = 4t^2/U$ (cf. Equation 2.31), and should thus scale as $t \propto \sqrt{J}$. Alternatively it can be deduced from an appropriate downfolding procedure of LDA+U band calculations [Lemmens05]. An account of these quantities is given in Table 5.6. The values of J for TiOBr and TiOCl differ by -45% (with respect to the value in TiOCl), whereas the experimental dispersion width is smaller in TiOBr by only 23%. Hence, an interpretation of the observed dispersion as spinon branch is clearly *not* suggested by this comparison.

On the contrary, the experimental width w'_b nicely matches the transfer integral as obtained from $t = \sqrt{JU}/2$ which is smaller in the bromide by 26% compared to the chloride. A similarly fair agreement is achieved with t from the LDA+U downfolding studies [Lemmens05] where the effective d_{xy}-d_{xy} hopping parameter along the *b* axis is smaller in TiOBr by 19% with respect to TiOCl. From this analysis it follows that the

Table 5.6: *Comparison of TiOBr and TiOCl with respect to various parameters possibly relevant for the observed dispersions: Width of the central part of the Ti 3d-band dispersion along b (w'_b), exchange constant J obtained from the magnetic susceptibility [Rückamp05a], transfer integral t derived from J, and the transfer integral t of downfolding LDA+U studies [Lemmens05].*

	TiOBr	TiOCl	$\Delta x/x$
1D dispersion w'_b	0.13 eV	0.17 eV	-23%
J from magnetic susceptibility	32 meV	58 meV	-45%
$t = \sqrt{JU}/2$	0.16 eV	0.22 eV	-26%
t from LDA+U	0.17 eV	0.21 eV	-19%

experimentally observed dispersions scale with t, not with J and thus can clearly be identified as charge excitations. In this light, it seems unlikely that the experimentally observed spectral dispersion is a superposition of both holon and spinon excitations.

Turning back to the starting point, i.e., the single-band 1D Hubbard model, a simple explanation for the lack of a spinon branch and shadow band would be that the two-dimensional coupling in these compounds under the particularities of a triangular lattice is already large enough so that generic 1D features of the spectral weight distribution can not persist. One would be then left with a lower Hubbard band that — though incoherent in nature — could still display sizable dispersion alike to the experimental observation. Clearly, this issue demands for a more detailed theoretical investigation. Alternatively, one could stick to the 1D Hubbard model and cite the coupling of phonons, multiorbital or spin-Peierls fluctuation effects as possible causes for the complete suppression of the generic 1D phenomenology. However, from the organic quasi-one-dimensional conductor TTF-TCNQ it is known that the phonons, which should couple equally strong to the electrons in this CDW system and are of even higher energy, do not suppress or smear out the spectral features of spin-charge separation and shadow band [Claessen02,Sing03]. Moreover, as already stated the orbital degrees of freedom are quenched in the oxyhalides and spin-Peierls fluctuations should not be very important so far above the transition temperatures. Therefore these two effects are probably not very effective.

In view of the above results one is thus left in a situation where on the one hand the spin-Peierls ground state of both oxyhalides studied here is dominated by 1D interactions while the analysis and discussion of the electronic dispersions at room temperature as well as the incommensurate order in the intermediate phase point to the importance of 2D (frustrated) interchain interactions. It remains interesting to see whether or not an anisotropic Hubbard model type description taking account of the magnetic interchain frustrations on the underlying triangular lattice is capable of better describing the electronic properties of this class of materials positioned in the regime between 1D and 2D correlations.

5.5.3 The Orbital Degrees of Freedom

As already pointed out in Section 5.4.1, fluctuations play an important role in the paramagnetic phase of the oxyhalides. This expresses itself, for instance, in an anomalous broadening of the TiOCl phonon lines in Raman and infrared spectroscopy [Lemmens04, Caimi04], indicating strong coupling of the lattice to the electronic (spin or orbital) degrees of freedom. In order to decide, if the orbital degree of freedom is indeed involved, it is important to evaluate the energy of a local excitation within the t_{2g} subshell. The LDA calculations yield that the d_{xy} state is lowest in energy, but a precise quantitative statement concerning the excitation energy to the higher lying d_{xz} and d_{yz} states is not possible on the LDA basis.[4]

While on one hand Jahn-Teller effects are generally less pronounced in t_{2g} orbitals and one would thus expect that the orbital degeneracy is lifted by a rather small crystal-field splitting, it must be noticed on the other hand that the coordinating octahedra are strongly distorted. The question naturally arises if the size of the energetic splitting allows for orbital fluctuations, or if this degree of freedom is quenched in the oxyhalides.

As a first *theoretical* answer, LDA+U calculations for frozen lattice distortions corresponding to the relevant phonon modes have shown that the orbital ground state may switch from $3d_{xy}$ to $3d_{xz,yz}$ for a sufficiently large amplitude [Saha-Dasgupta04]. Such a dynamical Jahn-Teller effect would lead to an orbitally mixed character of the time-averaged ground state. In contradiction to this result, recent cluster calculations combined with polarization-dependent optical data predict an energy value of $\approx 0.25\,\mathrm{eV}$ for the transition to the first excited state [Rückamp05a]. This result — much larger than the energy scale available through thermal fluctuations — certainly rules out orbital fluctuations. Unfortunately, this transition is not directly infrared active in the high-temperature structure and was therefore not observed in the optical transmittance measurements.

An *experimental* confirmation of this value for the smallest orbital excitation energy comes from ESR measurements. In a collaboration with Prof. Loidl's chair, ESR measurements were performed on TiOCl single crystals [Zakharov06]. From an analysis of the experimentally obtained g-factor it was possible to extract a value of $0.3 \pm 0.1\,\mathrm{eV}$ for the energy of the first excited state, in good agreement with the cluster calculations.

A more direct way to determine the orbital character of the occupied Ti $3d$ states experimentally will be presented in the remainder of this section [Hoinkis05]. Polarization-dependent photoemission measurements were carried out utilizing an Omicron AR 65 spectrometer equipped with a He discharge lamp and a rotatable polarizer. Additional polarization experiments with linearly polarized synchrotron light were performed at the SIS beamline of the Swiss Light Source using a Scienta SES 100 analyzer.

Experimental information on orbital symmetry can be obtained from these experiments making use of selection rules realized for special experimental geometries, as

---

[4]Note that the local excitation is not connected with charge transport, hence it should not be confused with the Mott gap of the LDA+U calculation depicted in Fig. 5.12 (b).

(a)

(b)
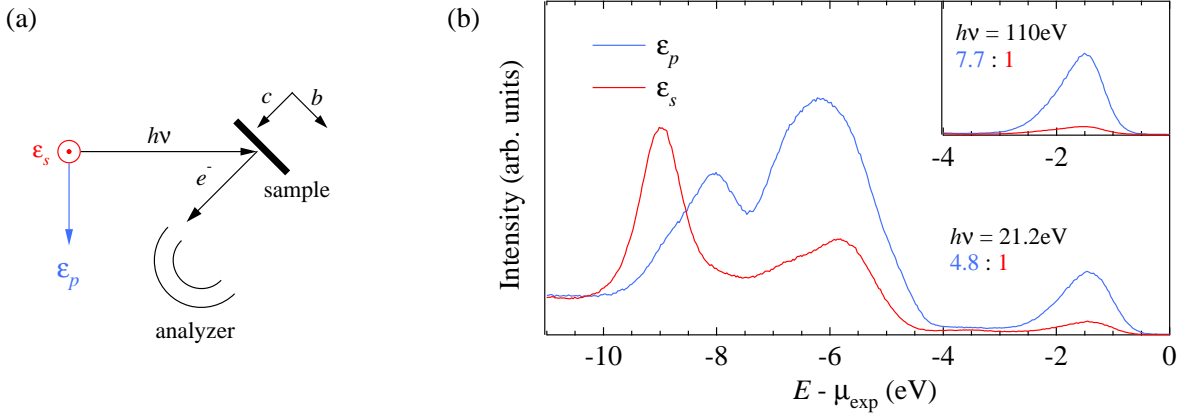
Figure 5.21: *Polarization-dependent photoemission experiment on TiOCl. (a) Sketch of the experimental setup. (b) Photoemission spectra measured at the Γ-point with parallel and perpendicular light polarization, respectively (T = 300 K). The inset shows the corresponding photoemission spectra measured at another photon energy (T = 365 K).*

outlined in Chapter 3. Assume the direction of the incident linearly polarized light and the emission direction of the photoelectrons lie within the same crystal mirror plane, as sketched in Fig. 5.21 (a). Then, with the polarization vector within (ε_p) and perpendicular (ε_s) to the mirror plane, the ejected electrons can stem only from states with well-defined even or odd parity with respect to this plane, respectively [Damascelli03]. The d_{xy}-derived band states of TiOCl are even with respect to the (b,c) mirror plane while the $d_{xz,yz}$ states are odd (cf. Fig. 3.2). Photoemission from d_{xy} states is hence dipole-allowed only for parallel light polarization ε_p, whereas $d_{xz,yz}$-emission can be observed for perpendicular polarization ε_s only.

Figure 5.21 (b) displays the results of such an ARPES experiment obtained with 21.2 eV photons at room temperature. The spectra were recorded at normal emission (i.e., at the Γ-point) with parallel (blue) and perpendicular (red) polarization, respectively. Since a laboratory He lamp with a rotatable polarizer was used, the photon flux is not changed by switching the polarization, and the spectra can be normalized to equal integration times per channel. At first glance, one can see that the intensity distribution over the whole valence band indeed is strongly affected by polarization effects. Focussing on the Ti 3d states reaching down to about 3.5 eV below μ_{exp}, their spectral weight is significantly reduced but not completely suppressed upon switching the polarization from parallel to perpendicular, indicating the dominance of d_{xy} emission. The residual 1 : 4.8 weight for perpendicular polarization can be quantitatively accounted for by the finite degree of light polarization ($\approx 85\%$), a possible small sample misalignment, and the effect of thermally activated symmetry-breaking phonons.[5] Similar data for the Ti 3d derived part of the electronic structure using polarized synchrotron radiation is depicted

---

[5]Note that the phonons involved in the dynamical Jahn-Teller effect discussed in Ref. [Saha-Dasgupta04] *do not* break the mirror symmetry of the (b,c)-plane.

in the inset of Panel (b). These spectra were recorded at a photon energy of $110\,\text{eV}$ and a temperature $T = 365\,\text{K}$ and normalized to equal photon flux. Due to the higher polarization degree of the synchrotron radiation the residual relative weight for perpendicular polarization is even further reduced. It is emphasized that this contribution does not vary down to room temperature within experimental accuracy, again indicating that phonon-induced orbital fluctuations are not important in this temperature range.

The photoemission data hence constitute direct experimental evidence that there is no sizable dynamical Jahn-Teller admixture of d_{xz} and d_{yz} states to the d_{xy} ground state at room temperature. This implies that orbital fluctuations play no role for the low-temperature physics of TiOCl.

5.6 Pressure-Induced Insulator-Metal Transition

The prospects of RVB superconductivity are the motivation for the efforts to metallize the Mott insulator TiOCl. For this purpose two different approaches come into consideration: A Mott insulator can in principle be driven into a metallic phase by shifting the chemical potential away from half-filling. Alternatively, tuning the crucial parameter U/W will also result in an insulator-metal transition once a critical threshold is overcome. Whereas the first route based on changing the *band-filling* of the system will be described in the next section, the pressure-induced insulator-metal transition [Kuntscher06] presented in the following is possibly an example for a *bandwidth-controlled* Mott transition.

Pressure-dependent measurements of both the optical transmittance and reflectance were performed by Prof. Kuntscher's group at room temperature using a Bruker IFS 66v/S FT-IR spectrometer with an infrared microscope (Bruker IRscope II). A diamond anvil cell (DAC) was used for the generation of pressures up to $18\,\text{GPa}$. The pressure was determined by the ruby luminescence method [Mao86]. For the transmission measurements various pressure transmitting media were used [CsI, methanol:ethanol (4:1)-mixture, argon]. The results qualitatively agree, but the pressure-induced effects occur at lower pressure ($\Delta P \approx 4\,\text{GPa}$) for CsI powder due to less hydrostatic conditions, as expected [Loa99]. For the reflectance measurements finely ground CsI powder was used as pressure transmitting medium to ensure direct contact of the sample with the diamond window. For each transmittance and reflectance measurement a small piece (about $80\,\mu\text{m} \times 80\,\mu\text{m}$) was cut from a single crystal with a thickness of $\leq 5\,\mu\text{m}$ and placed in the hole of a steel gasket. The reproducibility of the results was ensured by several experimental runs on different pieces of eight crystals.

The pressure-dependent transmittance was studied in a wide frequency range (2000–22000 cm^{-1}) for the polarization directions $\varepsilon \parallel a,b$. The intensity $I_\text{s}(E)$ of the radiation transmitting the sample was measured and normalized by a reference intensity $I_\text{r}(E)$. The latter was obtained focussing the incident radiation spot on the empty space in the gasket hole next to the sample for each pressure. The ratio $T(E) = I_\text{s}(E)/I_\text{r}(E)$ is a measure of the transmittance of the sample.
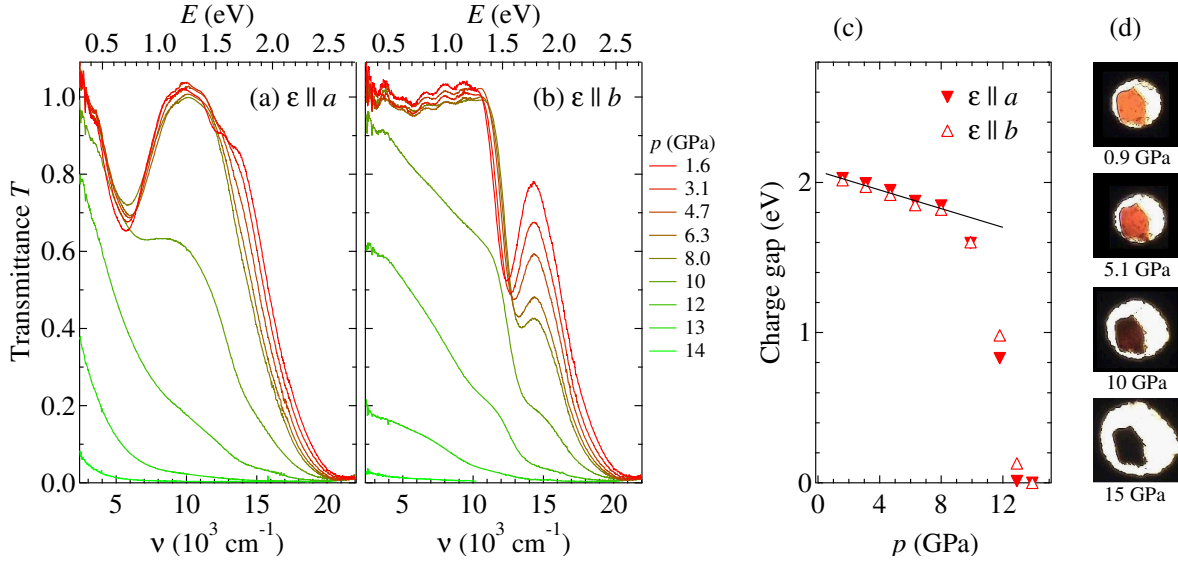
Figure 5.22: *Pressure-dependent optical measurements on TiOCl. (a,b) Pressure dependence of the transmittance $T(E)$ for the polarizations $\varepsilon \parallel a$ and $\varepsilon \parallel b$. (c) Charge gap, estimated from a linear extrapolation of the absorption edge, as a function of pressure. The full line corresponds to a linear fit to the data for $p \leq 8\,GPa$. (d) View inside the diamond unit cell during the pressure-dependent optical measurements.*

Reflectance measurements were carried out in the frequency range 2000–$11000\,\mathrm{cm}^{-1}$, using the intensity reflected from the inner diamond-air interface of the empty DAC as a reference.

Figure 5.22 (a) shows the pressure-dependent transmittance spectra of TiOCl for pressures up to $13.9\,\mathrm{GPa}$. Above $13.9\,\mathrm{GPa}$ the transmitted signal is zero. For the lowest applied pressure, pronounced absorption features are observed at around $0.66\,\mathrm{eV}$ and $1.53\,\mathrm{eV}$ in the $\varepsilon \parallel a$ and $\varepsilon \parallel b$ transmittance spectra, respectively. These two features can be attributed to excitations between the Ti $3d$ energy levels, whose degeneracy is lifted by the crystal field. As pointed out before, the transition to the first excited state is not infrared active. The observed features thus correspond to transitions from the d_{xy} ground state into the second excited state still in the t_{2g} subshell, and into the third excited state in the e_g subshell. Since the transmittance measurements were carried out on very thin samples (thickness $\leq 5\,\mu\mathrm{m}$), a precise determination of the positions of the two orbital excitations was possible. The values at zero pressure are in agreement with previously published results [Rückamp05a, Rückamp05b]. The crystal field splitting grows in amplitude with increasing pressure, indicated by the shift of the orbital excitations to higher frequencies. Apparently slight changes of the crystal structure, like modifications of the strong distortions of the TiO_4Cl_2 octahedra, are induced by the applied pressure.

For the lowest applied pressure, the transmittance is suppressed by excitations across the charge gap of approximately $2\,\mathrm{eV}$ [Rückamp05a]. The gap width can be estimated

by a linear extrapolation of the absorption edge. The results of this analysis, shown in Panel (c), yield a slow linear decay with increasing pressure up to $\approx 8\,\mathrm{GPa}$. Upon further increasing the pressure, the absorption edge rapidly shifts to lower energies, until at $\approx 12\,\mathrm{GPa}$ the transmittance is suppressed over the whole studied frequency range. This abrupt closure of the charge gap must be interpreted as the spectroscopic fingerprint of an insulator-metal transition.

The shift of the absorption edge out of the visible frequency range below $13000\,\mathrm{cm}^{-1}$ or $1.6\,\mathrm{eV}$ can be directly observed in form of a change in sample color. Panel (d) shows views inside the DAC at different pressures. At ambient pressure the thin sample is of a partly transparent, red appearance. Upon increasing the pressure above $8\,\mathrm{GPa}$ the sample becomes progressively opaque, as the visible fraction of the transmitted light rapidly shrinks. For $p > 12\,\mathrm{GPa}$ the sample is black. It must be noted, however, that the pressure-induced closure of the charge gap does not seem to be completely reversible, as parts of the sample do not recover their original color upon pressure release.

Also the reflectance measurements deliver indications for a pressure induced metal-insulator transition [Kuntscher06]. These experiments can be viewed as being complementary to the transmittance measurements, as they yield a significant signal only in the pressure regime where the samples' transmittance is small. At $\approx 12\,\mathrm{GPa}$ the reflectance abruptly increases in the whole energy range (not shown), demonstrating the transition-like character of the pressure-induced changes in the optical response.

These results — the suppression of the transmittance accompanied by a change of sample color and the increase of the reflectance — clearly indicate that a metallic state is induced in TiOCl at high pressure. The interpretation of this phenomenon as a bandwidth-controlled Mott transition is based on the well-established observation of insulator-metal transitions induced by *chemical* pressure in various inorganic and organic compounds. The spectroscopic signatures were demonstrated just recently in measurements of the dc and optical conductivity of pyrochlore-type molybdates [Kézsmárki04,Kézsmárki06]. The application of pressure (either external or chemical, i.e., by modifying the chemical composition) in general influences the bond lengths and bond angles, and hence modifies the width of the electronic bands near the Fermi energy. Assuming that the crystal-structure symmetry is not changed upon pressure application, this would be the first spectroscopic study of a bandwidth-controlled insulator-to-metal transition induced by *external* pressure.

However, the possibility of the transition being driven by a lattice-deformation instead of the bandwidth-reduction cannot be ruled out on the basis of the optical data. Such a scenario is suggested by the non-reversible character of the transition. This issue could be cleared up by a pressure dependent crystal-structure study, which is intended for the future.

In any case, the proximity to the metallic state in TiOCl is demonstrated by this experiment, thus founding the hope in the search for unconventional superconductivity.

5.7 Conclusion and Outlook

Even though it was shown in detail in this chapter that the undoped titanium oxyhalides adopt a spin-Peierls ground state, i.e., a state which can rather be described as a valence band solid than as a valence band liquid, it is not unlikely that upon doping the RVB state is favored. As pointed out in Section 2.4, mobile holes created by doping have the effect of stabilizing the RVB state.

Motivated by this prospect, several routes to dope TiOCl have been attempted. In a first doping study, titanium atoms were substituted by scandium or vanadium in the crystal growth process. Sc substitution corresponds to hole doping, as Sc is the adjacent transition metal with one electron less than Ti, whereas doping with V adds one extra electron per dopant to the system. Various doping concentrations were tested, ranging from 1% up to 50%. Unfortunately this did not lead to the anticipated metallization of the system. It seems that delocalization is more difficult to achieve for this inhomogeneous d^1/d^0 or d^1/d^2 electron count on the cation array compared to the d^9/d^8 mix in the cuprates created by anion substitution. The introduced disorder being associated with the change of the primary cations is obviously too large, so that doped charge carriers become Anderson-localized. This hypothesis is corroborated by ARPES measurements that showed a complete absence of electronic dispersion in the d band of the materials doped in this way. A similar effect was evidenced by ARPES on TiOCl samples sputtered *in situ*. The idea behind this experiment was to remove oxygen or chlorine atoms from the top layer, which corresponds to an effective electron doping. An XPS analysis showed that largely the Cl species is affected by the sputtering, which is not surprising as these atoms comprise the top-most surface layer. A series of sputter experiments was conducted, each of which consisted of several sputtering cycles with subsequent photoemission measurements to inspect the changes in the electronic structure. As a result, the conductivity of the TiOCl crystals was enhanced significantly, so that it was possible to measure down to $14\,\mathrm{K}$ without excessive charging up of the sample. However, the electronic dispersion vanished completely long before a change in the conductivity was detectable. The induced disorder seemed to dominate the spectra, just as in the V and Sc doping experiments.

From these lessons the conclusion has to be drawn that doping should be conducted in a more gentle way, without disturbing the system too much. One possible solution would be to substitute the anions, and the most obvious choice for this is to replace oxygen by nitrogen, motivated by the existence of the isostructural nitride halides ZrNCl and HfNCl. Unfortunately, up to date it was not accomplished to substitute a relevant amount of oxygen by nitrogen, neither by partly replacing the crystal growth reactants by NH_4Cl, nor by directly trying to introduce the nitrogen in the crystals under high pressure and high temperatures in an autoclave. However, these experiments are still in an early stage, and one cannot rule out a success along this route in the future.

The most promising way appears to be the *in situ* evaporation of alkali metal atoms. Ideally they intercalate and donate their valence electrons without introducing a great

amount of disorder. First photoemission results, collected by S. Glawion in Würzburg, are very promising in the sense that the electronic dispersion of the Ti d band has not yet vanished, but it is significantly altered without changing the size of the charge gap. The spectra are not shown in this thesis as this is a very preliminary result. The *in situ* evaporation — in this case of Sodium atoms — has so far only been attempted once, and it is clear that these findings have to be validated and analyzed in more detail. Specifically, it must be examined if the sodium atoms really intercalate or simply stay at the surface and possibly oxidize there, and it is not clear yet how to interpret the observed band dispersions. Nevertheless, it was shown that it is possible to gently dope a TiOCl crystal without destroying its crystal structure to such an extent that the electronic dispersion is lost. Summarizing, the alkali metal intercalation seems to be a very promising candidate for doping the oxyhalides.

Even though the outlined doping attempts did not result in a metallization as anticipated, the prospects of success should not be underestimated, as the following arguments show. First of all, the insulator-metal transition under pressure presented in the previous section is named in this context, as it proves the proximity to a metallic state in TiOCl. Second, the LDA+DMFT study by Craco *et al.* is quoted [Craco04], which predicts the possibility of a band-filling induced insulator-metal transition with multi-orbital correlations. The authors even tentatively suggest that electron doped TiOCl may exhibit unconventional superconductivity if a metallic state is reached, in accordance with the mean-field results presented in Section 2.4. However, these results have to be handled carefully, as the choice of the iterative perturbation theory (IPT) for the impurity solver is debated for the multi-orbital case [Saha-Dasgupta05]. Last but not least, it was already successfully demonstrated that the isostructural compounds ZrNCl and HfNCl can be effectively doped by alkali metal intercalation. Remarkably, it was possible to drive the nitride halides into a superconducting state, however mediated by conventional electron-phonon coupling.

The prospect of a possible superconducting phase based on the RVB state is especially exciting due to the predictions of Anderson in his pioneering paper of 1987 [Anderson87a]. For an optimal doping level of $x = U/t$, which yields the realistic value of 6% for the case of TiOCl, from his theory a superconducting transition temperature of up to the order of J is expected. It need not be overly emphasized, that this energy scale of $660\,\mathrm{K}$ for the chloride is enough motivation to search for ways to suitably dope these compounds and achieve a state that exhibits superconductivity.

6 Summary

The materials in the scope of this dissertation belong to the domain where Peierls and Mott physics meet — in other words both electron-phonon coupling and electronic correlations play an essential role in these systems. With $1T$-$TaSe_2$ a layered transition metal compound was investigated that can be regarded as a paradigm quasi-two-dimensional CDW system. The appeal of this material certainly lies in the occurrence of a surface Mott metal-insulator transition, which is driven by CDW-induced changes of the electronic bandwidth and can thus be controlled simply by varying the temperature. In Chapter 4, a detailed examination of the electronic structure in the presence of the CDW was presented. The results of DFT calculations make it possible to identify a separated conduction band with a strongly reduced width compared to the undistorted state, which explains the rather unusual appearance of Mott physics in a $5d$ transition metal compound. This observation corroborates the Mott-Hubbard scenario with star-of-David clusters as relevant sites of the corresponding Hubbard picture. The Mott transition at the surface of $1T$-$TaSe_2$, for which clear evidence was presented in form of angle-resolved photoemission data, is one of the few examples where one is able to observe the evolution of the spectral function while going through the transition by tuning the crucial ration U/W within the same single crystal. In the metallic phase, the photoemission spectra directly exhibit the occupied part of the three-peak structure as it is expected from DMFT predictions for a correlated metal, i.e., a lower Hubbard band and a quasiparticle peak at the Fermi level. Upon cooling a drastic rearrangement of spectral weight towards higher binding energies takes place, which is interpreted as spectral signature of a Mott-Hubbard transition: The quasiparticle peak vanishes in favor of the Hubbard subbands.

Compared to the charge-Peierls transition, its counterpart involving the spin degree of freedom — i.e., the spin-Peierls transition — must be considered a much rarer phenomenon. The compounds TiOCl and TiOBr studied in the course of this dissertation are, together with $CuGeO_3$, the only known inorganic materials to exhibit this instability. Furthermore, the record-high transition temperatures and interaction strengths found the particular interest in these systems. After the Mott insulator TiOCl was interpreted as spin-Peierls system for the first time in 2003 by Seidel *et al.* on the basis of magnetization measurements [Seidel03], it was the success of XRD experiments presented in Chapter 5 to provide direct evidence for the spin-Peierls nature of the TiOCl low-temperature phase. Also the nature of the intermediate state of TiOCl as incommensurately modulated spin-Peierls state could be revealed by XRD measurements, thus completing a coherent spin-Peierls picture of the oxyhalides TiOCl and TiOBr with two

successive phase transitions. The existence of an extended fluctuation regime above the intermediate phase is confirmed by measurements of the heat capacity, which show a strongly delayed release of entropy and thus hint towards the major role played by fluctuations. The orbital sector as possible origin of these fluctuations can be ruled out on the basis of photoemission experiments utilizing selection rules for polarized radiation.

In a comprehensive study focussing on the normal state electronic structure, both the momentum-integrated and momentum resolved spectral function was determined experimentally by means of photoelectron spectroscopy. Complemented by various DFT and model calculations, these measurements show that the electronic structure of TiOCl and TiOBr cannot be understood in a one-particle picture. The best fit to the data was accomplished by DDMRG calculations for the single-band 1D Hubbard model. However, a comparison of the two compounds, which reveals the much greater importance of interchain coupling in the bromide, leads to the conclusion that multi-band effects and/or the magnetic interchain interaction on the triangular lattice have to be taken into account in order to arrive at a realistic theoretic modelling of these systems.

It is exactly this triangular lattice with its geometric frustration of magnetic interactions that fuels the expectations that another fascinating phenomenon — the RVB state — is not far from being realized in the titanium oxyhalides. In this regard the results of pressure-dependent optical transmittance and reflectance measurements appear particularly intriguing: The observed closure of the correlation gap at about 12 GPa is clear evidence for an insulator-metal transition. Assuming that changes of the crystal-structure symmetry are not involved, this would be the first observation of a bandwidth-controlled Mott transition induced by external pressure. The interesting point concerning this experimental discovery is that according to RVB theory the proximity to a metallic state gives reason to anticipate promising chances for finding a novel, RVB-type superconductivity realized in suitably doped oxyhalides.

Bibliography

[Aebi01]   P. Aebi, Th. Pillo, H. Berger, and F. Lévy. "On the search for Fermi surface nesting in quasi-2D materials". *Journal of Electron Spectroscopy and Related Phenomena* **117-118**, 433, 2001.

[Aiura03a]   Y. Aiura, H. Bando, R. Kitagawa, S. Maruyama, Y. Nishihara, K. Horiba, M. Oshima, O. Shiino, and M. Nakatake. "Electronic structure of layered $1T$-$TaSe_2$ in commensurate charge-density-wave phase studied by angle-resolved photoemission spectroscopy". *Physical Review B* **68**(7), 073408, 2003.

[Aiura03b]   Y. Aiura, I. Hase, H. Bando, K. Yagi-Watanabe, K. Ozawa, T. Iwase, Y. Nishihara, O. Shiino, M. Oshima, M. Kubota, and K. Ono. "Ta 5d Band Symmetry of $1T$-$TaS_{1.2}Se_{0.8}$ in the Commensurate Charge-Density-Wave Phase". *Physical Review Letters* **91**(25), 256404, 2003.

[Aiura04]   Y. Aiura, I. Hase, K. Yagi-Watanabe, H. Bando, K. Ozawa, K. Tanaka, R. Kitagawa, S. Maruyama, T. Iwase, Y. Nishihara, K. Horiba, O. Shiino, M. Oshima, M. Nakatake, M. Kubota, and K. Ono. "Increase in charge-density-wave potential of $1T$-TaS_xSe_{2-x}". *Physical Review B* **69**(24), 245123, 2004.

[Anderson73] P. W. Anderson. "Resonating Valence Bonds: A New Kind of Insulator?". *Materials Research Bulletin* **8**, 153, 1973.

[Anderson87a] P. W. Anderson. "The Resonating Valence Bond State in La_2CuO_4 and Superconductivity". *Science* **235**, 1196, 1987.

[Anderson87b] P. W. Anderson, G. Baskaran, Z. Zou, and T. Hsu. "Resonating-valence-bond theory of phase transitions and superconductivity in La_2CuO_4-based compounds". *Physical Review Letters* **58**, 2790, 1987.

[Anisimov93] V. I. Anisimov, I. V. Solovyev, M. A. Korotin, M. T. Czyzyk, and G. A. Sawatzky. "Density-functional theory and NiO photoemission spectra". *Physical Review B* **48**, 16929, 1993.

[Ashcroft76] N. W. Ashcroft and N. D. Mermin. *Solid State Physics*, chapter 33. Saunders College Publishing, 1976.

[Baskaran87]   G. Baskaran, Z. Zou, and P. W. Anderson. "The Resonating Valence Bond State and High-T$_c$ Superconductivity — A Mean Field Theory". *Solid State Communications* **63**, 973, 1987.

[Baskaran93]   G. Baskaran. "Fundamentals of RVB Theory and Some Applications to High Temperature Superconductors". In L. C. Gupta and M. S. Multani, editors, *Frontiers in Solid State Sciences — Vol. 1, Selected Topics in Superconductivity*. World Scientific, 1993.

[Baskaran01]   G. Baskaran. "Anderson's Theory of High-T$_c$ Superconductivity". In N. P. Ong and R. N. Bhatt, editors, *More is Different: Fifty Years of Condensed Matter Physics*, chapter 8. Princeton University Press, 2001.

[Bayliss84]   S. C. Bayliss, A. M. Ghorayeb, and D. R. P. Guy. "Thermal and transport evidence for a phase transition in $1T$-TaS$_2$ observed at $282\,\mathrm{K}$ upon warming". *Journal of Physics C: Solid State Physics* **17**(21), L533, 1984.

[Bednorz86]   J. G. Bednorz and K. A. Müller. "Possible high-T$_c$ superconductivity in the BaLaCuO system". *Zeitschrift für Physik B Condensed Matter* **64**, 189, 1986.

[Benthien04]   H. Benthien, F. Gebhard, and E. Jeckelmann. "Spectral Function of the One-Dimensional Hubbard Model away from Half Filling". *Physical Review Letters* **92**, 256401, 2004.

[Bethe31]   H. A. Bethe. "Zur Theorie der Metalle". *Zeitschrift für Physik* **71**, 205, 1931.

[Beynon93]   R. J. Beynon and J. A. Wilson. "TiOCl, TiOBr—are these RVB d^1, $S = \frac{1}{2}$ materials? The results of scandium substitution set in the context of other $S = \frac{1}{2}$ systems of current interest for high-temperature superconductivity and the metal-insulator transition". *Journal of Physics: Condensed Matter* **5**, 1983, 1993.

[Blaha01]   P. Blaha, K. Schwarz, and J. Luitz, 2001. Computer code WIEN2k, Techn. Univ. Wien, Vienna, URL http://www.wien2k.at.

[Bovet04]   M. Bovet, D. Popovic, F. Clerc, C. Koitzsch, U. Probst, E. Bucher, H. Berger, D. Naumovic, and P. Aebi. "Pseudogapped Fermi surfaces of $1T$-TaS$_2$ and $1T$-TaSe$_2$: A charge density wave effect". *Physical Review B* **69**(12), 125117, 2004.

[Bray83]   J. W. Bray, L. V. Interrante, I. S. Jacobs, and J. C. Bonner. *The Spin-Peierls Transition*, chapter 7. Plenum Press, New York, 1983.

[Brouwer80]   R. Brouwer and F. Jellinek. "The Low-Temperature Superstructures of $1T$-TaSe$_2$ and $2H$-TaSe$_2$". *Physica B* **99**, 51, 1980.

[Bulaevskii63]   L. N. Bulaevskii. "Theory of a linear anti-ferromagnetic chain". *Soviet Physics JETP* **16**, 685, 1963.

[Bulla99]   R. Bulla. "Zero Temperature Metal-Insulator Transition in the Infinite-Dimensional Hubbard Model". *Physical Review Letters* **83**(1), 136, 1999.

[Buslaps91]   T. Buslaps. *Elektronische Struktur und Phasentransformationen der Tantaldichalkogenide*. PhD thesis, Christian-Albrechts-Universität zu Kiel, 1991.

[Buzdin80]   A. I. Buzdin and L. N. Bulaevskii. "Spin-Peierls transition in quasi-one-dimensional crystals". *Soviet Physics / Uspekhi* **23**, 409, 1980.

[Caimi04]   G. Caimi, L. Degiorgi, N. N. Kovaleva, P. Lemmens, and F. C. Chou. "Infrared optical properties of the spin-$\frac{1}{2}$ quantum magnet TiOCl". *Physical Review B* **69**, 125108, 2004.

[Carlson04]   E. W. Carlson, V. J. Emery, S. A. Kivelson, and D. Orgad. "Concepts in High Temperature Superconductivity". In K.H. Bennemann and J.B. Ketterson, editors, *The Physics of Conventional and Unconventional Superconductors, Vol. II*. Springer Verlag, 2004.

[Claessen97]   R. Claessen. *Photoelektronenspektroskopie niederenergetischer Anregungen in niedrigdimensionalen Festkörpern*. Habilitationsschrift, Universität des Saarlandes, 1997.

[Claessen02]   R. Claessen, M. Sing, U. Schwingenschlögl, P. Blaha, M. Dressel, and C. S. Jacobsen. "Spectroscopic signatures of spin-charge separation in the quasi-one-dimensional organic conductor TTF-TCNQ". *Physical Review Letters* **88**, 096402, 2002.

[Clerc04]   F. Clerc, M. Bovet, H. Berger, L. Despont, C. Koitzsch, O. Gallus, L. Patthey, M. Shi, J. Krempasky, M. G. Garnier, and P. Aebi. "Spin-orbit splitting in the valence bands of $1T$-TaS$_2$ and $1T$-TaSe$_2$". *Journal of Physics: Condensed Matter* **16**(18), 3271, 2004.

[Colonna05]   S. Colonna, F. Ronci, A. Cricenti, L. Perfetti, H. Berger, and M. Grioni. "Mott Phase at the Surface of $1T$-TaSe$_2$ Observed by Scanning Tunneling Microscopy". *Physical Review Letters* **94**(3), 036405, 2005.

[Craco04]   L. Craco, M. S. Laad, and E. Müller-Hartmann. "Metallizing the Mott insulator TiOCl by electron doping: A view from LDA+DMFT". cond-mat/0410472, 2004.

[Cross79]   M. C. Cross. "Effects of magnetic fields on a spin-Peierls transition". *Physical Review B* **20**, 4606, 1979.

[Damascelli03] A. Damascelli, Z. Hussain, and Z.-X. Shen. "Angle-resolved photoemission studies of the cuprate superconductors". *Reviews of Modern Physics* **75**, 473, 2003.

[Damascelli04] A. Damascelli. "Probing the Electronic Structure of Complex Systems by ARPES". *Physica Scripta* **T109**, 61, 2004.

[Daul00]   S. Daul and R.M. Noack. "Phase diagram of the half-filled Hubbard chain with next-nearest-neighbor hopping". *Physical Review B* **61**, 1646, 2000.

[DiSalvo74]   F. J. DiSalvo, R. G. Maines, and J. V. Waszczac. "Preparation and Properties of $1T$-TaSe$_2$". *Solid State Communications* **14**, 497, 1974.

[Duffy68]   W. Duffy and K. P. Barr. "Theory of Alternating Antiferromagnetic Heisenberg Linear Chains". *Physical Review* **165**, 647, 1968.

[Ehrenfreund77] E. Ehrenfreund and L. S. Smith. "Nuclear-spin-lattice relaxation process in spin-Peierls systems". *Physical Review B* **16**(5), 1870, 1977.

[Eyert96]   V. Eyert. "A Comparative Study on Methods for Convergence Acceleration of Iterative Vector Sequences". *Journal of Computational Physics* **124**, 271, 1996.

[Eyert98]   V. Eyert and K.-H. Höck. "Electronic structure of V_2O_5: Role of octahedral deformations". *Physical Review B* **57**(20), 12727, 1998.

[Eyert00]   V. Eyert. "Basic notions and applications of the augmented spherical wave method". *International Journal of Quantum Chemistry* **77**(6), 1007, 2000.

[Fazekas79]   P. Fazekas and E. Tosatti. "Electrical, structural and magnetic properties of pure and doped $1T$-TaS$_2$". *Philosophical Magazine B* **39**(3), 229, 1979.

[Fazekas99a]   P. Fazekas. *Lecture Notes on Electron Correlation and Magnetism*, chapter 4. World Scientific, 1999.

[Fazekas99b]   P. Fazekas. *Lecture Notes on Electron Correlation and Magnetism*, chapter 6.3. World Scientific, 1999.

[Fröhlich54]   H. Fröhlich. "On the theory of superconductivity: the one-dimensional case". *Proceedings of the Royal Society of London Series A* **223**, 296, 1954.

[Fulde91]   P. Fulde. *Electron Correlations in Molecules and Solids*, chapter 12. Springer Verlag, 1991.

[Grüner88]   G. Grüner. "The dynamics of charge-density waves". *Reviews of Modern Physics* **60**, 1129, 1988.

[Grüner94]   G. Grüner. *Density waves in solids*. Adison-Wesley, 1994.

[Gutzwiller63]   M. C. Gutzwiller. "Effect of Correlation on the Ferromagnetism of Transition Metals". *Physical Review Letters* **10**(5), 159, 1963.

[Hase93]   M. Hase, I. Terasaki, and K. Uchinokura. "Observation of the spin-Peierls transition in linear Cu^{2+} (spin-1/2) chains in an inorganic compound $CuGeO_3$". *Physical Review Letters* **70**, 3651, 1993.

[Hemberger05]   J. Hemberger, M. Hoinkis, M. Klemm, M. Sing, R. Claessen, S. Horn, and A. Loidl. "Heat capacity of the quantum magnet TiOCl". *Physical Review B* **72**, 012420, 2005.

[Hoinkis05]   M. Hoinkis, M. Sing, J. Schäfer, M. Klemm, S. Horn, H. Benthien, E. Jeckelmann, T. Saha-Dasgupta, L. Pisani, R. Valentí, and R. Claessen. "Electronic structure of the spin-$\frac{1}{2}$ quantum magnet TiOCl". *Physical Review B* **72**, 125127, 2005.

[Hoinkis06]   M. Hoinkis, M. Sing, S. Glawion, L. Pisani, R. Valentí, S. van Smaalen, and R. Claessen. "One-dimensional versus two-dimensional correlation effects in the oxyhalides TiOCl and TiOBr: A comparative photoemission study". To be published, 2006.

[Horiba02]   K. Horiba, K. Ono, J. H. Oh, T. Kihara, S. Nakazono, M. Oshima, O. Shiino, H. W. Yeom, A. Kakizaki, and Y. Aiura. "Charge-density wave and three-dimensional Fermi surface in $1T$-$TaSe_2$ studied by photoemission spectroscopy". *Physical Review B* **66**, 073106, 2002.

[Hubbard63]   J. Hubbard. "Electron correlations in narrow energy bands". *Proceedings of the Royal Society of London Series A* **276**, 238, 1963.

[Hüfner95]   S. Hüfner. *Photoelectron Spectroscopy*. Springer-Verlag, 1995.

[Hüfner99]   S. Hüfner, R. Claessen, F. Reinert, Th. Straub, V. N. Strocov, and P. Steiner. "Photoemission spectroscopy in metals: band structure-Fermi surface-spectral function". *Journal of Electron Spectroscopy and Related Phenomena* **100**, 191, 1999.

[Huisman69]   R. Huisman and F. Jellinek. "On the Polymorphism of Tantalum Diselenide". *Journal of the Less-Common Metals* **17**, 111, 1969.

[Imai03]   T. Imai and F. C. Chou. "Novel Spin-Gap Behavior in Layered $S = \frac{1}{2}$ Quantum Spin System TiOCl". cond-mat/0301425, 2003.

[ISI06]   ISI Web of Knowledge, 2006. URL http://www.isiknowledge.com/.

[Jeckelmann02] E. Jeckelmann. "Dynamical density-matrix renormalization-group method". *Physical Review B* **66**, 045114, 2002.

[Kanamori63]   J. Kanamori. "Electron Correlation and Ferromagnetism of Transition Metals". *Progress of Theoretical Physics* **30**(3), 275, 1963.

[Kataev03]   V. Kataev, J. Baier, A. Möller, L. Jongen, G. Meyer, and A. Freimuth. "Orbital orderin the low-dimensional quantum spin system TiOCl probed by ESR". *Physical Review B* **68**, 140405(R), 2003.

[Kevan92]   S. Kevan, editor. *Angle-Resolved Photoemission — Theory and Current Applications.* Elsevier, 1992.

[Kézsmárki04] I. Kézsmárki, N. Hanasaki, D. Hashimoto, S. Iguchi, Y. Taguchi, S. Miyasaka, and Y. Tokura. "Charge Dynamics Near the Electron-Correlation Induced Metal-Insulator Transition in Pyrochlore-Type Molybdates". *Physical Review Letters* **93**(26), 266401, 2004.

[Kézsmárki06] I. Kézsmárki, N. Hanasaki, K. Watanabe, S. Iguchi, Y. Taguchi, S. Miyasaka, and Y. Tokura. "Variation of the charge dynamics in bandwidth- and filling-controlled metal-insulator transitions of pyrochlore-type molybdates". *Physical Review B* **73**(12), 125122, 2006.

[Kotliar04]   G. Kotliar and D. Vollhardt. "Strongly Correlated Materials: Insights from Dynamical Mean-Field Theory". *Physics Today* **57**(3), 53, 2004.

[Krimmel06]   A. Krimmel, J. Strempfer, B. Bohnenbuck, B. Keimer, M. Hoinkis, M. Klemm, S. Horn, A. Loidl, M. Sing, R. Claessen, and M. v. Zimmermann. "Incommensurate structure of the spin-Peierls compound TiOCl in zero and finite magnetic fields". *Physical Review B* **73**, 172413, 2006.

[Kuntscher06] C. A. Kuntscher, S. Frank, A. Pashkin, M. Hoinkis, M. Klemm, M. Sing, S. Horn, and R. Claessen. "Pressure-induced insulator-to-metal transition in low-dimensional TiOCl". cond-mat/0603376, 2006.

[Landau79]   L. D. Landau and E. M. Lifshitz. *Statistical Physics, Part 1.* Elsevier, 1979.

[Lashley03]   J. C. Lashley, M. F. Hundley, A. Migliori, J. L. Sarrao, P. G. Pagliuso, T. W. Darling, M. Jaime, J. C. Cooley, W. L. Hults, L. Morales, D.J. Thoma, J.L. Smith, J. Boerio-Goates, B.F. Woodfield, G.R. Stewart,

R.A. Fisher, and N.E. Phillips. "Critical examination of heat capacity measurements made on a Quantum Design physical property measurement system". *Cryogenics* **43**(6), 369, 2003.

[Lemmens04] P. Lemmens, K. Y. Choi, G. Caimi, L. Degiorgi, N. N. Kovaleva, A. Seidel, and F. C. Chou. "Giant phonon softening in the pseudogap phase of the quantum spin system TiOCl". *Physical Review B* **70**, 134429, 2004.

[Lemmens05] P. Lemmens, K. Y. Choi, R. Valentí, T. Saha-Dasgupta, E. Abel, Y. S Lee, and F. C. Chou. "Spin gap formation in the quantum spin systems TiOX, X = Cl and Br". *New Journal of Physics* **7**, 74, 2005.

[Lichtenstein98] A. I. Lichtenstein and M. I. Katsnelson. "Ab initio calculations of quasiparticle band structure in correlated systems: LDA++ approach". *Physical Review B* **57**, 6884, 1998.

[Lieb68] E. H. Lieb and F. Y. Wu. "Absence of Mott Transition in an Exact Solution of the Short-Range, One-Band Model in One Dimension". *Physical Review Letters* **20**(25), 1445, 1968.

[Lieth77] R. M. A. Lieth, editor. *Preparation and Crystal Growth of Materials with Layered Structures*. R. Reidel Publishing Company, 1977.

[Loa99] I. Loa, U. Schwarz, M. Hanfland, R.K. Kremer, and K. Syassen. "Crystal Structure and Optical Spectroscopy of NaV_2O_5 under Pressur". *physica status solidi (b)* **215**, 709, 1999.

[Madelung78] O. Madelung. *Introduction to Solid-State Theory*. Springer Verlag, 1978.

[Manske04] D. Manske. *Theory of Unconventional Superconductors — Cooper-Pairing Mediated by Spin Excitations*, chapter 2.5. Springer Verlag, 2004.

[Mao86] H. K. Mao, J. Xu, and P. M. Bell. "Calibration of the ruby pressure gauge to 800 kbar under quasi-hydrostatic conditions". *Journal of Geophysical Research* **91**, 4673, 1986.

[Maule88] C. H. Maule, J. N. Tothill, P. Strange, and J. A. Wilson. "An optical investigation into the $3d^1$ and $3d^2$ transition-metal halides and oxyhalides, compounds near to delocalisation". *Journal of Physics C: Solid State Physics* **21**, 2153, 1988.

[Metzner89] W. Metzner and D. Vollhardt. "Correlated Lattice Fermions in $d = \infty$ Dimensions". *Physical Review Letters* **62**(3), 324, 1989.

[Moncton77]   D. E. Moncton, R. J. Birgeneau, L. V. Interrante, and F. Wudl. "X-Ray Scattering Study of Spin-Lattice Dimerization in a Quasi One-Dimensional Heisenberg Antiferromagnet". *Physical Review Letters* **39**, 507, 1977.

[Mott49]   N. F. Mott. "The Basis of the Electron Theory of Metals, with Special Reference to the Transition Metals". *Proceedings of the Physical Society A* **62**, 416, 1949.

[Mott61]   N. F. Mott. "The Transition to the Metallic State". *The Philosophical Magazine* **6**, 287, 1961.

[Mott90]   N. F. Mott. *Metal–Insulator Transitions*. Taylor and Francis, London, 2nd edition, 1990.

[Mühlschlegel59]   B. Mühlschlegel. "Die thermodynamischen Funktionen des Supraleiters". *Zeitschrift für Physik A* **155**(3), 313, 1959.

[Müller-Hartmann88]   E. Müller-Hartmann. "Überlegungen zur Theorie der Hochtemperatursupraleiter". In *Supraleitung und verwandte Quantenphänomene - Vorlesungsmanuskripte des 19. IFF-Ferienkurses*. KFA Jülich, 1988.

[Myron75]   H. W. Myron and A. J. Freeman. "Electronic structure and Fermi-surface-related instabilities in $1T$-TaS$_2$ and $1T$-TaSe$_2$". *Physical Review B* **11**(8), 2735, 1975.

[Nagaosa92]   N. Nagaosa and P. A. Lee. "Ginzburg-Landau theory of the spin-charge-separated system". *Physical Review B* **45**, 966, 1992.

[Nitzsche67]   R. Nitzsche. "Kristallzucht aus der Gasphase durch chemische Transportreaktionen". *Fortschritte der Mineralogie* **44**, 231, 1967.

[Palatinus05]   L. Palatinus, A. Schönleber, and S. van Smaalen. "Two-fold superstructure of titanium(III)-oxybromide at T = 17.5 K". *Acta Crystallographica Section C* **61**, i48, 2005.

[Pauling33]   L. Pauling and G. W. Wheland. "The Nature of the Chemical Bond. V. The Quantum-Mechanical Calculation of the Resonance Energy of Benzene and Naphthalene and the Hydrocarbon Free Radicals". *The Journal of Chemical Physics* **1**, 362, 1933.

[Peierls34]   R. E. Peierls. "Remarks on Transition Temperatures". *Helvetica Physica Acta* **7**, Suppl. 2, 81, 1934.

[Peierls55]   R. E. Peierls. *Quantum theory of solids*. Oxford University Press, 1955.

[Peierls91]   R. E. Peierls. *More Surprises in Theoretical Physics*. Princeton University Press, 1991.

[Perdew96]   J. P. Perdew, K. Burke, and M. Ernzerhof. "Generalized Gradient Approximation Made Simple". *Physical Review Letters* **77**, 3865, 1996.

[Perfetti03]   L. Perfetti, A. Georges, S. Florens, S. Biermann, S. Mitrovic, H. Berger, Y. Tomm, H. Hochst, and M. Grioni. "Spectroscopic Signatures of a Bandwidth-Controlled Mott Transition at the Surface of $1T$-$TaSe_2$". *Physical Review Letters* **90**(16), 166401, 2003.

[Pfalzer05]   P. Pfalzer. Private communication, 2005.

[Pytte74]   E. Pytte. "Peierls Instability in Heisenberg chains". *Physical Review B* **10**, 4637, 1974.

[Rossnagel06]   K. Rossnagel and N. V. Smith. "Spin-orbit coupling in the band structure of reconstructed $1T$-TaS_2". *Physical Review B* **73**(7), 073106, 2006.

[Rückamp05a]   R. Rückamp, J. Baier, M. Kriener, M. W. Haverkort, T. Lorenz, G. S. Uhrig, L. Jongen, A. Möller, G. Meyer, and M. Grüninger. "Zero-Field Incommensurate Spin-Peierls Phase with Interchain Frustration in TiOCl". *Physical Review Letters* **95**, 097203, 2005.

[Rückamp05b]   R. Rückamp, E. Benckiser, M. W. Haverkort, H. Roth, T. Lorenz, A. Freimuth, L. Jongen, A. Möller, G. Meyer, P. Reutler, B. Büchner, A. Revcolevsci, S.-W. Cheong, C. Sekar, G. Krabbes, and M. Grüninger. "Optical study of orbital excitations in transition-metal oxides". *New Journal of Physics* **7**, 144, 2005.

[Saha-Dasgupta04]   T. Saha-Dasgupta, R. Valentí, H. Rosner, and C. Gros. "TiOCl, an orbital-ordered system?". *Europhysics Letters* **67**(1), 63, 2004.

[Saha-Dasgupta05]   T. Saha-Dasgupta, A. Lichtenstein, and R. Valentí. "Correlation effects on the electronic structure of TiOCl: A NMTO+DMFT study". *Physical Review B* **71**, 153108, 2005.

[Schäfer58]   H. Schäfer, F. Wartenpfuhl, and E. Weise. "Titan(III)-oxychlorid". *Zeitschrift für anorganische und allgemeine Chemie* **295**, 268, 1958.

[Schäfer62]   H. Schäfer. *Chemische Transportreaktionen*. Verlag Chemie, 1962.

[Schäfer01]   J. Schäfer, E. Rotenberg, S. D. Kevan, P. Blaha, R. Claessen, and R. E. Thorne. "High-Temperature Symmetry Breaking in the Electronic Band Structure of the Quasi-One-Dimensional Solid $NbSe_3$". *Physical Review Letters* **87**, 196403, 2001.

[Schattke03]   W. Schattke and M. A. van Hove, editors. *Solid-State Photoemission and Related Methods.* Wiley-VCH, 2003.

[Schnering72]   H. G. V. Schnering, M. Collin, and M. Hassheider. "TiOBr; Darstellung, Eigenschaften und Struktur". *Zeitschrift für anorganische und allgemeine Chemie* **387**, 137, 1972.

[Schönleber06] A. Schönleber, S. van Smaalen, and L. Palatinus. "Structure of the incommensurate phase of the quantum magnet TiOCl". *Physical Review B* **73**(21), 214410, 2006.

[Seidel03]   A. Seidel, C. A. Marianetti, F. C. Chou, G. Ceder, and P. A. Lee. "$S = \frac{1}{2}$ chains and spin-Peierls transition in TiOCl". *Physical Review B* **67**, 020405(R), 2003.

[Sharma02]   S. Sharma, L. Nordström, and B. Johansson. "Stabilization of charge-density waves in $1T$-TaX_2 ($X =$ S, Se, Te): First-principles total energy calculations". *Physical Review B* **66**(19), 195101, 2002.

[Shaz05]   M. Shaz, S. van Smaalen, L. Palatinus, M. Hoinkis, M. Klemm, S. Horn, and R. Claessen. "Spin Peierls transition in TiOCl". *Physical Review B* **71**, 100405(R), 2005.

[Sing03]   M. Sing, U. Schwingenschlögl, R. Claessen, P. Blaha, J. M. P. Carmelo, L. M. Martelo, P. D. Sacramento, M. Dressel, and C. S. Jacobsen. "Electronic structure of the quasi-one-dimensional organic conductor TTF-TCNQ". *Physical Review B* **68**, 125111, 2003.

[Slough86]   C. G. Slough, W. W. McNairy, R. V. Coleman, B. Drake, and P. K. Hansma. "Charge-density waves studied with the use of a scanning tunneling microscope". *Physical Review B* **34**, 994, 1986.

[Smith74]   N. V. Smith, M. M. Traum, and F. J. Di Salvo. "Mapping energy bands in layer compounds from the angular dependence of ultraviolet photoemission". *Solid State Communications* **15**(2), 211, 1974.

[Smith75]   N. V. Smith and M. M. Traum. "Angular-resolved ultraviolet photoemission spectroscopy and its application to the layer compounds TaSe$_2$ and TaS$_2$". *Physical Review B* **11**(6), 2087, 1975.

[Smith85]   N. V. Smith, S. D. Kevan, and F. J. DiSalvo. "Band structures of the layer compounds $1T$-TaS$_2$ and $2H$-TaSe$_2$ in the presence of commensurate charge-density waves". *Journal of Physics C: Solid State Physics* **18**(16), 3175, 1985.

[Soyer96]   A. Soyer. "*LAUEX*: a user-friendly program for the simulation and in-dexation of Laue diagrams on UNIX systems". *Journal of Applied Crystallography* **29**(4), 509, 1996.

[Strocov03]   V. N. Strocov. "Intrinsic accuracy in 3-dimensional photoemission band mapping,". *Journal of Electron Spectroscopy and Related Phenomena* **130**, 65, 2003.

[Taylor02]   P. L. Taylor and O. Heinonen. *A Quantum Approach to Condensed Matter Physics*. Camebridge University Press, 2002.

[Tinkham75]   M. Tinkham. *Introduction to Superconductivity*. MacGraw-Hill Book Co., 1975.

[van Smaalen05] S. van Smaalen, L. Palatinus, and A. Schönleber. "Incommensurate interactions and nonconventional spin-Peierls transition in TiOBr". *Physical Review B* **72**, 020105(R), 2005.

[van Smaalen06] S. van Smaalen. Private communication, 2006.

[Voit00]   J. Voit, L. Perfetti, F. Zwick, H. Berger, G. Margaritondo, G. Grüner, H. Höchst, and M. Grioni. "Electronic Structure of Solids with Competing Periodic Potentials". *Science* **290**, 501, 2000.

[Wiegers01]   G. A. Wiegers, J. L. de Boer, A. Meetsma, and S. van Smaalen. "Domain structure and refinement of the triclinic superstructure of $1T$-TaSe$_2$ by single crystal X-ray diffraction". *Zeitschrift für Kristallographie* **216**, 45, 2001.

[Wilson75]   J. A. Wilson, F. J. Di Salvo, and S. Mahajan. "Charge-density waves and superlattices in the metallic layered transition metal dichalcogenides". *Advances in Physics* **24**, 117, 1975.

[Wilson87]   J. A. Wilson, C. Maule, P. Strange, and J. N. Tothill. "Anomalous behaviour in the layer halides and oxyhalides of titanium and vanadium: a study of materials close to delocalisation". *Journal of Physics C: Solid State Physics* **20**, 4159, 1987.

[Woolley77]   A. M. Woolley and G. Wexler. "Band structures and Fermi surfaces for $1T$-TaS$_2$, $1T$-TaSe$_2$, and $1T$-VSe$_2$". *Journal of Physics C: Solid State Physics* **10**(14), 2601, 1977.

[Wu89]   X. L. Wu and C. M. Lieber. "Hexagonal domain-like charge density wave phase of TaS2 determined by scanning tunneling microscopy". *Science* **243**, 1703, 1989.

[Yeh85]   J. J. Yeh and I. Lindau. "Atomic Subshell Photoionization Cross Sections and Asymmetry Parameters: $1 \leq Z \leq 103$". *Atomic Data and Nuclear Data Tables* **32**, 1, 1985.

[Zakharov06] D. V. Zakharov, J. Deisenhofer, H.-A. Krug von Nidda, P. Lunkenheimer, J. Hemberger, M. Hoinkis, M. Klemm, M. Sing, R. Claessen, M. V. Eremin, S. Horn, and A. Loidl. "Spin dynamics in the low-dimensional magnet TiOCl". *Physical Review B* **73**, 094452, 2006.

Acknowledgment

Curriculum Vitae

Personal Data

Markus Hoinkis
born 17.08.1976 in Augsburg
german

Education

09/1987 – 06/1996	HOLBEIN GYMNASIUM AUGSBURG
06/1996	Abitur
10/1997 – 08/2001	UNIVERSITÄT AUGSBURG
10/1999	Vordiplom
08/2001 – 08/2002	MICHIGAN STATE UNIVERSITY, USA
08/2002	M. S. in physics, Advisor: Prof. N. O. Birge
10/2002 – 01/2007	UNIVERSITÄT AUGSBURG
01/2007	PhD in physics, Advisor: Prof. R. Claessen

Work Experience

08/1996 – 09/1997	Alternative service, TSV HAUNSTETTEN, Augsburg
10/2002 – 08/2006, 11/2006 – 03/2007	Research assistant at the Chair of Experimental Physics II, UNIVERSITÄT AUGSBURG
08/2006 – 10/2006	Research assistant at the Suga Laboratory, OSAKA UNIVERSITY, Japan